UNIVERSITY OF SOUTHAMPTON

Faculty of Social Sciences
School of Mathematical Sciences

Modelling Charge Transport in Lithium-Ion Batteries

by
Ethan Culverhouse
ORCiD: 0009-0005-3528-1812

A thesis for the degree of
Doctor of Philosophy

24th March 2024

University of Southampton

Abstract

Faculty of Social Sciences
School of Mathematical Sciences

Doctor of Philosophy

Modelling Charge Transport in Lithium-Ion Batteries

by Ethan Culverhouse

Lithium-ion batteries are highly considered for rechargeable storage devices due to their competitive theoretical capacities and energy densities; they have shown great potential for use in electric and hybrid vehicles. Having already found use in smaller portable devices, research now pushes to increase their efficiency through the use of models to better understand the processes occurring and by studying materials for new designs. In this thesis, we first focus on the charge transport occurring within the electrolyte before considering the intercalation of lithium within electrode particles. We begin by giving an overview of the structure and current development of a lithium-ion battery before discussing the equations to describe the movements of ions in the electrolyte phase. We discuss the application of these equations to a dilute electrolyte and then introduce moderately concentrated electrolyte theory, where we now consider the interactions between ions. We present an ion-hopping model using a Monte Carlo algorithm to simulate these ionic interactions and the effect on their movements. We use this model to find the activity coefficients of electrolytes composed of $LiPF_6$ using various solvents. We discuss single-particle models and how they can be used to simplify computationally intensive models such as the Doyle-Fuller-Newman model. A study of quantum tunnelling and solving the Schrödinger equation is presented, which we apply to $LiFePO_4$ and $LiCoO_2$ cathodes to investigate electron tunnelling as a potential cause of electrode degradation and electrolyte decomposition.

Contents

Research Thesis: Declaration of Authorship

Print name: ETHAN CULVERHOUSE

Title of thesis: MODELLING CHARGE TRANSPORT IN LITHIUM-ION BATTERIES

I declare that this thesis and the work presented in it are my own and has been generated by me as the result of my own original research.

I confirm that:

1. This work was done wholly or mainly while in candidature for a research degree at this University;
2. Where any part of this thesis has previously been submitted for a degree or any other qualification at this University or any other institution, this has been clearly stated;
3. Where I have consulted the published work of others, this is always clearly attributed;
4. Where I have quoted from the work of others, the source is always given. With the exception of such quotations, this thesis is entirely my own work;
5. I have acknowledged all main sources of help;
6. Where the thesis is based on work done by myself jointly with others, I have made clear exactly what was done by others and what I have contributed myself;
7. None of this work has been published before submission

Signature: ..... Date:.....

List of Variables and Parameters

Table showing the variable and parameters and their descriptions and units used throughout the thesis. The table displays starts with Latin letters and then Greek letters each in alphabetical order.

Symbol	Description	Units
a_n	Activity of the negative ionic species	dimensionless
a_p	Activity of the positive ionic species	dimensionless
a_s	Activity of the neutral solvent species	dimensionless
B	Permeability factor of the electrodes	dimensionless
b_{et}	Brunauer-Emmett-Teller (commonly shortened to BET) surface area	m^{-1}
C_{num}	Coordination number (or ligancy) change in text	dimensionless
c_0	Initial ion concentration of the electrolyte	$mol\ m^{-3}$
$c_{0,a}$	Initial concentration of lithium ions in the anode particles	$mol\ m^{-3}$
$c_{0,c}$	Initial concentration of lithium ions in the cathode particles	$mol\ m^{-3}$
c_a	Concentration of lithium ions in the anode particles	$mol\ m^{-3}$
c_c	Concentration of lithium ions in the cathode particles	$mol\ m^{-3}$
c_a^{max}	Maximum concentration of lithium ions in the anode particles	$mol\ m^{-3}$
c_c^{max}	Maximum concentration of lithium ions in the cathode particles	$mol\ m^{-3}$
c_e	Ion concentration of the electrolyte	$mol\ m^{-3}$
c_n	Concentration of the negative ionic species in the electrolyte	$mol\ m^{-3}$
c_p	Concentration of the positive ionic species in the electrolyte	$mol\ m^{-3}$
c_s	Concentration of the neutral solvent species in the electrolyte	$mol\ m^{-3}$
c_T	Total concentration of the electrolyte	$mol\ m^{-3}$
D_a	Diffusivity function of the lithium ions in the anode particles	$m^2\ s^{-1}$
D_c	Diffusivity function of the lithium ions in the cathode particles	$m^2\ s^{-1}$
D_e	Diffusivity function of the ions in the electrolyte	$m^2\ s^{-1}$
D_{eff}	Effective Diffusivity of the electrolyte	$m^2\ s^{-1}$
D_{ij}	Maxwell-Stefan diffusivity of species i due to species j	dimensionless
D_n	Diffusion coefficient of the negative ionic species in the electrolyte	$m^2\ s^{-1}$
D_p	Diffusion coefficient of the positive ionic species in the electrolyte	$m^2\ s^{-1}$
D_s	Diffusion coefficient of the neutral solvent species in the electrolyte	$m^2\ s^{-1}$
$\mathbf{d}_n$	Driving force on negative ions due to chemical potential gradient	N
$\mathbf{d}_p$	Driving force on positive ions due to chemical potential gradient	N
$\mathbf{d}_s$	Driving force on solvent due to chemical potential gradient	N
$\mathbf{E}$	Electric field	$V\ m^{-1}$
E_a	Activation energy for the given reaction to occur	J
E_{cell}	Potential difference across the cell	V
E_{cell}^0	Standard cell potential difference	V
E_{ox}^0	Oxidation standard potential difference	V
E_{red}^0	Reduction standard potential difference	V

E_{eq}	Equilibrium potential	V
E_{ij}	Energy required for a particle to hop from site i to site j	J
E_{i-j}	Average interaction energy between particles of substances i and j	J
E_q	Total energy of the quantum particle change	J
E_i^{Tot}	Total energy of the system due to particles of substance i	J
F_c	Electrostatic force between two point charges	N
$\mathbf{F}_{d_n}$	Drag force exerted on a negative ion due to the electrolyte	N
$\mathbf{F}_{d_p}$	Drag force exerted on a positive ion due to the electrolyte	N
$\mathbf{F}_{e_n}$	Force on a negative ion in electrolyte due to electric field	N
$\mathbf{F}_{e_p}$	Force on a positive ion in electrolyte due to electric field	N
f_{ij}	Drag coefficient inflicted in species i by species j	dimensionless
G	Gibbs free energy	J
G^0	Standard Gibbs free energy	J
G_{A_a}	Gibbs energy of activation for the anodic reaction	J
G_{A_c}	Gibbs energy of activation for the cathodic reaction	J
$G^0_{A,a}$	Gibbs energy of activation for anodic reaction standard conditions	J
$G^0_{A,c}$	Gibbs energy of activation for cathodic reaction standard conditions	J
G^{mix}	Gibbs free energy of mixing	J
H	Enthalpy	J
$G_{i,initial}$	Gibbs free energy of substance i before mixing	J
$G_{i,final}$	Gibbs free energy of substance i after mixing	J
$G_{T,initial}$	Total Gibbs free energy of the solution before mixing	J
$G_{T,final}$	Total Gibbs free energy of the solution after mixing	J
H_{mix}	Enthalpy of mixing	J
I	Current through the cell	A
j	Current density in the electrolyte	$A\ m^{-2}$
j_0	Exchange current density	$A\ m^{-2}$
j_a	Current density in the anode particles	$A\ m^{-2}$
j_c	Current density in the cathode particles	$A\ m^{-2}$
j_n	Current density on the surface of the electrode particles	$A\ m^{-2}$
K_{d_n}	Drag coefficient of the negative ion species	dimensionless
K_{d_p}	Drag coefficient of the positive ion species	dimensionless
k_a	Butler-Volmer rate constant for the anodic reaction	depends on order
k_c	Butler-Volmer rate constant for the cathodic reaction	depends on order
k_i	Wave number	m^{-1}
M_i^{mol}	Molar mass of substance i	kg
m_i	Mass of substance i	kg
N_-	Flux of a general negative ion in the electrolyte	$mol\ m^{-2}s^{-1}$
N_T	Number of steps between temperature changes	dimensionless
n_e	Number of electrons transported	dimensionless
n_i	Number of ions of species i in a solution	dimensionless

n_{total}	Total number of ions in a solution	dimensionless
$P_{i,j}$	Probability of a particle hopping from site i to site j	dimensionless
p	Pressure	Pa
Q	Charge	C
Q^r	Reaction quotient	dimensionless
$\mathbf{q}_{a_n}$	Advective flux of the negative ionic species	$mol\ m^{-2}s^{-1}$
$\mathbf{q}_{a_p}$	Advective flux of the positive ionic species	$mol\ m^{-2}s^{-1}$
$\mathbf{q}_{d_n}$	Diffusive flux of the negative ionic species	$mol\ m^{-2}s^{-1}$
$\mathbf{q}_{d_p}$	Diffusive flux of the positive ionic species	$mol\ m^{-2}s^{-1}$
$\mathbf{q}_n$	Flux of the negative ionic species in the electrolyte	$mol\ m^{-2}s^{-1}$
$\mathbf{q}_p$	Flux of the positive ionic species in the electrolyte	$mol\ m^{-2}s^{-1}$
$\mathbf{q}_s$	Flux of the neutral solvent species in the electrolyte	$mol\ m^{-2}s^{-1}$
R_a	Radius of the anode particles	m
R_c	Radius of the cathode particles	m
R_k	Rate constant for the given reaction	depends on order
r	Distance from the centre of an electrode particle	m
S	Entropy	$J\ K^{-1}$
S_{mix}	Entropy of mixing	$J\ K^{-1}$
T	Absolute temperature	K
T^{coeff}	Transmission coefficient	dimensionless
T_c	Temperature reducing constant	dimensionless
$T_{initial}$	Initial chosen temperature for the simulation	K
t	Time	s
t^+	Electrolyte transference number	dimensionless
U	Internal energy	J
$U_{eq,a}$	Open-circuit potential in the anode	V
$U_{eq,c}$	Open-circuit potential in the cathode	V
V	Cell voltage	V
V_a	Electric potential at the anode current collector	V
V_{bar}	Function of the potential barrier	V
V_c	Electric potential at the cathode current collector	V
V_i^c	Electric potential energy of point charge i due to the other point charges	V
V_{Total}^c	Total electric potential energy of a system of point charges	V
$V*$	Volume	m^3
V_n^*	Partial molar volume of the negative ionic species in the electrolyte	m^3
V_p^*	Partial molar volume of the positive ionic species in the electrolyte	m^3
V_s^*	Partial molar volume of the neutral solvent species in the electrolyte	m^3
$\mathbf{v}_n$	Velocity of the negative ionic species in the electrolyte	ms^{-1}
$\mathbf{v}_p$	Velocity of the positive ionic species in the electrolyte	ms^{-1}
$\mathbf{v}_s$	Velocity of the neutral solvent species in the electrolyte	ms^{-1}
x	Distance across the electrochemical cell	m

z_n	Valency of the negative ion species	dimensionless
z_p	Valency of the positive ion species	dimensionless

Symbol	Description	Units
α_a	Charge transfer coefficient for the anodic reaction	dimensionless
α_c	Charge transfer coefficient for the cathodic reaction	dimensionless
γ_n	Activity coefficient of the negative ionic species	dimensionless
γ_p	Activity coefficient of the positive ionic species	dimensionless
γ_s	Activity coefficient of the neutral solvent species	dimensionless
ϵ	Permittivity of the electrolyte	$F\ m^{-1}$
ϵ_{el}	Volume fraction of the electrolyte	dimensionless
ϵ_r	Relative permittivity of the medium compared to a vacuum	dimensionless
η_a	Overpotential between the electrolyte and anode particles	V
η_c	Overpotential between the electrolyte and cathode particles	V
κ	Conductivity of the electrolyte	$S\ m^{-1}$
μ_n	Chemical potential of the negative ionic species	$J\ mol^{-1}$
μ_p	Chemical potential of the positive ionic species	$J\ mol^{-1}$
μ_s	Chemical potential of the neutral species	$J\ mol^{-1}$
μ_n^0	Chemical potential of negative ions species under standard conditions	$J\ mol^{-1}$
μ_p^0	Chemical potential of positive ion species under standard conditions	$J\ mol^{-1}$
μ_s^0	Chemical potential of solvent species under standard conditions	$J\ mol^{-1}$
$\hat{\mu_n}$	Electrochemical potential of the negative ionic species	$J\ mol^{-1}$
$\hat{\mu_p}$	Electrochemical potential of the positive ionic species	$J\ mol^{-1}$
$\hat{\mu_s}$	Electrochemical potential of the neutral solvent species	$J\ mol^{-1}$
ρ	Charge density in the electrolyte	$C\ m^{-3}$
σ_a	Conductivity in the anode	$S\ m^{-1}$
σ_c	Conductivity in the cathode	$S\ m^{-1}$
Φ_a	Electric potential in the anode	V
Φ_c	Electric potential in the cathode	V
ϕ_e	Electric potential in the electrolyte	V
χ_n	Mole fraction of the negative ionic species	dimensionless
χ_p	Mole fraction of the positive ionic species	dimensionless
χ_s	Mole fraction of the neutral solvent species	dimensionless
Ψ	Wave function (1-dimensional)	$m^{-\frac{1}{2}}$
ω	Work done	J

Table showing the description and values of the physical constants used in the thesis.

Symbol	Description	Value
e	Elementary charge	1.602176634x10^{-19} C
ϵ_0	Permittivity of a vacuum	8.8541878128x10^{-12} $F\ m^{-1}$
F	Faraday constant	9.648533212x10^{4} $C\ mol^{-1}$
$\hat{h}$	Reduced Planck constant	1.054571817x10^{-34} $J\ s$
k_B	Boltzmann constant	1.380649x10^{-23} $J\ K^{-1}$
k_e	Coulomb constant	8.9875517923x10^{9} $N\ m^2\ C^{-2}$
N_A	Avogadro constant	6.02214076x10^{23} mol^{-1}
R_g	Universal gas constant	8.31446261815324 $J\ mol^{-1}\ K^{-1}$

Table showing the description of the chemical symbols used in the thesis.

Chemical Symbol	Description
C_6	Graphite
$CO(CH_2O)_2$	Ethylene carbonate (EC)
$CO(C_2H_5O)_2$	Diethyl carbonate (DC)
$CO(C_3H_8O_2)$	Ethyl methyl carbonate (EMC)
Co^{3+} / Co^{4+}	Cobalt ion
Li^+	Lithium ion
$LiAsF_6$	Lithium hexafluoroarsenate
$LiBF_4$	Lithium tetrafluoroborate
$LiCoO_2$	Lithium cobalt oxide
$LiCoPO_4$	Lithium cobalt phosphate
$LiFePO_4$	Lithium iron phosphate (LFP)
$LiMn_2O_4$	Lithium manganese oxide (LMO)
$LiMnPO_4$	Lithium manganese phosphate
$LiPF_6$	Lithium hexafluorophosphate
$LiWO_2$	Lithium tungsten oxide
Mn^{+3} / Mn^{+4}	Manganese ion
TiS_2	Titanium disulfide

1 Introduction

With the increasing need for sustainable energy storage devices that are both economical and reliable, the research and development of lithium-ion batteries as rechargeable storage devices has increased significantly in recent years. Since Sony released the first commercial secondary lithium-ion battery in 1991 (Blomgren, 2017), they have shown significant advantages in terms of high energy densities and low self-discharge compared to other types of rechargeable batteries. Small lithium-ion batteries have found use in many portable electronics, such as mobile phones and laptops (Al Hallaj et al., 1999) and show great potential for use in electric vehicles. (Goodenough and Park, 2013).

Researchers are still encountering problems relating to the safety of such devices; the build-up of heat due to the exothermic reactions can lead to thermal runaway (Al Hallaj et al., 1999). However, the precautions to prevent such problems, such as the use of non-flammable electrolytes, can take away from the potential electrochemical performance. The occurrence of unwanted side reactions can also cause irreversible capacity fade, an issue many types of lithium-ion batteries experience, which reduces its useful cycling life (Ramadass et al., 2003). Models to predict such behaviour have been developed to try to understand the potential causes. The effects of overcharging can result in the deposition of lithium on the negative electrode and electrolyte decomposition; this process reduces the available lithium and electrolyte on further cycling (Zhang et al., 2000). A $LiC_6|LiPF_6|LiMn_2O_4$ cell was investigated, with a model predicting that the use of thinner electrodes consisting of smaller particles would reduce this effect (Arora, White and Doyle, 1999). By modelling the charge and discharge of a lithium-ion battery, we can better understand the processes that occur, with the aim of current research to improve charging rate and cycling performance to make them more efficient for use in vehicles while still maintaining low cost and high safety.

In this chapter, we review the literature focused on the development and current research of lithium-ion batteries, with a discussion of relevant materials studied. In Section 1.1, we begin by giving an overview of the structure of an electrochemical cell and the general mechanism through which it works before moving on to describe the electrochemical reactions occurring at the electrodes during the charge and discharge processes in Section 1.2. We then explore their development and

discuss the important properties for an efficient lithium-ion battery in Section 1.3 by focusing on each part of a cell separately.

1.1 The Structure of a Lithium-Ion Battery

A lithium-ion battery is composed of many electrochemical cells, where each cell is made up of four main parts: two electrodes, one positive and one negative, the electrolyte, and a separator, which acts as a barrier to prevent the flow of electrons between the electrodes but still allows the lithium ions to pass through. Each electrode has a current collector, which is then attached to an external circuit. This structure is shown in Figure 1, where a) and b) show the cell during charge and discharge, respectively.

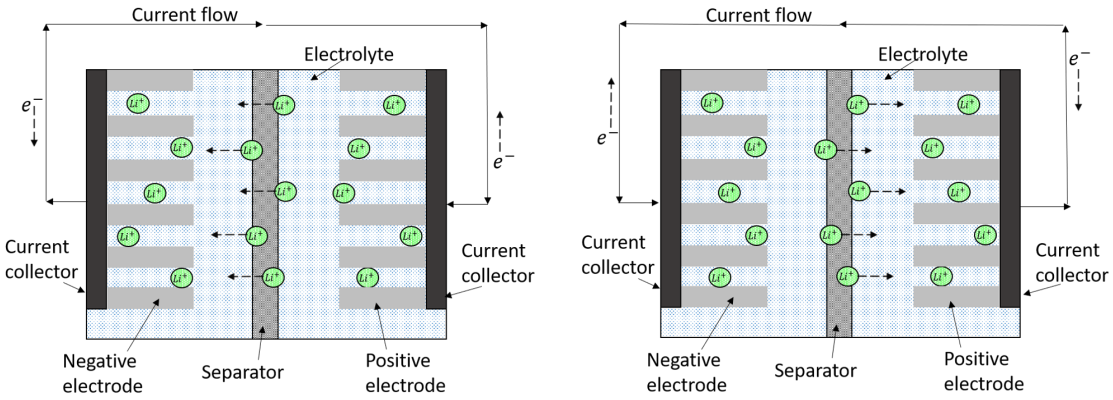

Figure 1: A representation of a lithium-ion battery during a) (left) charge and b) (right) discharge. The lithium ions move through the electrolyte and cross the separator while the electrons travel between the current collectors via the external circuit.

During the discharge of the cell, the lithium ions are transported from the negative electrode, known as the anode, to the positive electrode, known as the cathode, by the following mechanism: they diffuse from the particles in the negative electrode to the electrode-electrolyte interface. Here, an oxidation reaction occurs which results in the release of a lithium ion into the electrolyte. These ions now diffuse and move under the influence of the electric field, through the electrolyte towards the positive electrode where the ions intercalate with the electrode via a reduction reaction and diffuse into the positive electrode particles. Meanwhile, an electron is released into the negative electrode which travels through the external circuit, via the current collectors, to the positive electrode, where it is absorbed by a positive lithium ion.

This movement of electrons generates the current.

A similar process occurs while the cell is being charged, but instead the lithium ions are transported from the positive electrode to the negative electrode. However, for this mechanism to occur, a potential difference must be applied across the cell.

1.2 Electrochemical Reactions

Electrochemical reactions occur at both the anode and cathode during the charge and discharge processes. The discharge reactions will occur spontaneously, while the charge reactions only occur when a potential has been applied. The spontaneity is determined by the electrode materials' relative oxidising/reducing ability, which is a measure of its tendency to give away/take in electrons. This concept is closely related to that of Gibbs Free Energy.

1.2.1 Gibbs Free Energy

The idea of Gibbs free energy, denoted G, was first considered in the 1870s by Josiah Willard Gibbs, where he termed the concept as the 'available energy' of a system (Atkins et al., 1988). More specifically, it can be described as the amount of energy stored in a system that is 'free' to do work (Atkins and De Paula, 2014) and depends on the enthalpy and entropy of the system as follows:

$$G = H - TS, \tag{1.1}$$

where T is the temperature in Kelvin. Here, S is the entropy, a measure of the disorder in the energy of a system and therefore relates to the amount of energy that is not available to do work. In general, energy has a tendency to disperse from a localised area as well as convert to different forms, making a system more chaotic. Therefore, with every spontaneous change the entropy will increase (Atkins et al., 1988).

H is the enthalpy, which can be written as:

$$H = U + pV^*, \tag{1.2}$$

where p is the pressure, V^* is the volume, and U is the internal energy of the system. It is a measure of the energy required to create and then maintain the system.

We are interested in the change in Gibbs free energy when a reaction occurs. Consider an electrochemical cell where a reaction is occurring at constant temperature and pressure. As the reaction advances over time, we can write the change in Gibbs energy as:

$$\Delta G = \left.\frac{\partial G}{\partial t}\right|_{T,p=const.} \quad [1.3]$$

While the reaction advances we can denote the amount of work that can be done as ω so, by the definition of Gibbs free energy, we can write that:

$$\frac{d\omega}{dt} = \Delta G. \quad [1.4]$$

During this change, work will be done to transport electrons between the electrodes, this is given by the product of the amount of charge transported, Q, and the potential difference across the electrochemical cell, which we will denote as E_{cell}:

$$d\omega = QE_{cell}. \quad [1.5]$$

We can write the amount of charge transported as $-n_eFdt$ where n_e denotes the number of electrons that are transported throughout the whole reaction, and F is Faraday's constant, which is defined as the magnitude of charge per mole of electrons. The minus sign represents the negative charge of an electron. We can therefore write:

$$d\omega = -n_eFE_{cell}dt. \quad [1.6]$$

Combining equations [1.4] and [1.6], we therefore find the relation between the Gibbs free energy and the cell potential:

$$\Delta G = -n_eFE_{cell}. \quad [1.7]$$

Note that, in general, the Gibbs free energy is often considered relative to some standard Gibbs free energy for the particular reaction, ΔG^0. It can be given by (Atkins and De Paula, 2014):

$$\Delta G = \Delta G^0 + RTln(Q^r), \qquad [1.8]$$

where R is the universal gas constant and T is absolute temperature. Here, Q^r is known as the reaction quotient and is related to the activities of the products relative to the activities of the reactants. We will be considering ideal solutions so the activities can typically be replaced with concentration-like terms. In Chapter 3, we will go into more detail about activities and how they are important when looking at non-ideal solutions.

Substituting equation [1.7] into [1.8] and rearranging, leads to:

$$E_{cell} = -\frac{\Delta G^0}{n_e F} - \frac{RT}{n_e F}\ln(Q^r), \qquad [1.9]$$

and therefore we can introduce a standard cell potential, E^0_{cell}, such that:

$$E^0_{cell} = -\frac{\Delta G^0}{n_e F}, \qquad [1.10]$$

therefore giving:

$$E_{cell} = E^0_{cell} - \frac{RT}{n_e F}\ln(Q^r). \qquad [1.11]$$

This equation is known as the Nernst equation. To understand how this concept links to the charge and discharge processes, we will consider the reactions that take place within an electrochemical cell composed of a $LiCoO_2$ cathode and a C_6 anode.

We first need to look at the standard potentials of each electrode (relative to the standard hydrogen electrode). These values are typically given as the reduction potential, but the relative oxidation potential is found by simply taking the negative of the reduction potential.

The standard potentials for the reduction of each electrode are given by (relative to the standard hydrogen electrode):

$$Li^+ + C_6 + e^- \rightarrow LiC_6 \quad (E^0_{red}(C_6/LiC_6) \sim -2.84V \text{vs. SHE}), \qquad [1.12]$$

$$\mathrm{Li^+ + CoO_2 + e^- \rightarrow LiCoO_2} \quad (E^0_{red}(\mathrm{CoO_2/LiCoO_2}) \sim 1.00V \text{vs. SHE}), \quad [1.13]$$

where the standard potentials for the relative oxidation reactions are given by $-E^0$.

Overall, the standard potential difference of the cell, E^0_{cell}, is given by the sum of the oxidation standard potential of the oxidation reaction and the reduction standard potential of the reduction reaction. We can denote this as:

$$E^0_{cell} = E^0_{ox}(ox) + E^0_{red}(red), \quad [1.14]$$

where we are using the subscript to denote the type of standard potential we are using and the term in brackets to denote which reaction.

Rewriting this in terms of just the reduction standard potentials, we therefore find:

$$E^0_{cell} = -E^0_{red}(ox) + E^0_{red}(red). \quad [1.15]$$

Considering the example of a $\mathrm{LiCoO_2}$ cathode and a $\mathrm{C_6}$ anode, we have the overall reaction of the cell:

$$\mathrm{CoO_2 + LiC_6 \rightarrow LiCoO_2 + C_6}, \quad [1.16]$$

where we have the following reactions occurring at the anode [1.17] and cathode [1.18] respectively. These are known as half-equations:

Oxidation reaction at the anode:

$$\mathrm{LiC_6 \rightarrow C_6 + Li^+ + e^-}, \quad [1.17]$$

Reduction reaction at the cathode:

$$\mathrm{CoO_2 + Li^+ + e^- \rightarrow LiCoO_2}, \quad [1.18]$$

and the calculation of E^0_{cell} is as follows:

$$\begin{aligned} E^0_{cell} &= E^0_{ox}(anode) + E^0_{red}(cathode), & [1.19] \\ &= -(E^0_{red}(anode) + E^0_{red}(cathode), & [1.20] \\ &= (-(-2.84) + 1.00 = 3.84V \text{ vs. SHE}. & [1.21] \end{aligned}$$

As this value for E^0_{cell} is positive (so ΔG is negative) we can see the following overall reaction given in [1.16] is therefore the discharge reaction that occurs spontaneously.

Once the cell has discharged, it will need to be recharged again by the following reaction:

$$\mathrm{LiCoO_2 + C_6 \rightarrow CoO_2 + LiC_6}. \qquad [1.22]$$

The value of E^0_{cell} for this reaction is $\sim -3.84V$, and therefore the Gibbs free energy is positive, indicating a non-spontaneous reaction. In order to drive this reaction to occur, a potential difference of greater than $3.84V$ must be applied.

1.2.2 Capacity Fade

The equations discussed above are the theoretical reactions that will occur in the electrochemical cell. In reality, not all the lithium will be extracted and inserted between the electrodes. The reactions given in [1.17] and [1.18] can instead be written as:

At the anode:

$$\mathrm{LiC_6} \underset{\text{charge}}{\overset{\text{discharge}}{\rightleftharpoons}} \mathrm{Li_{1-x}C_6} + x\,\mathrm{Li^+} + x\mathrm{e^-}, \qquad [1.23]$$

At the cathode:

$$\mathrm{Li_{1-x}CoO_2} + x\,\mathrm{Li^+} + x\mathrm{e^-} \underset{\text{charge}}{\overset{\text{discharge}}{\rightleftharpoons}} \mathrm{LiCoO_2}, \qquad [1.24]$$

where x represents the number of moles of lithium that are successfully transferred between the two electrodes. This value varies for different materials for each electrode and will also decrease over repeated charge and discharge cycles, representing a fading capacity with each cycle. A decrease in capacity for a given material can be caused by various mechanisms (Zhang et al., 2000); this can include a permanent change in the structure of the electrode, which can prevent some lithium ions from being able to (de)-intercalate, or the loss of lithium to unwanted side reactions, which can reduce the amount of lithium available to be transferred (Imamura et al., 2011). This is an important concept to consider when selecting materials for use as an anode or cathode; a material that experiences less structural degradation and less loss of lithium can maintain capacity for a longer useful cycling life.

1.3 The Development of Lithium-Ion Batteries

The idea behind a lithium-ion battery was first developed in the early 1970s by Michel Armand, who first considered the idea of lithium ions moving reversibly between two intercalating electrodes (Blomgren, 2017). This idea was then taken further by Lazzari and Scrosati, who went on to develop a cell composed of $LiWO_2$ and TiS_2 electrodes. Due to the potentials of the chosen electrodes, the potential range of the cell was limited, but after completing 68 cycles, the cell showed relatively little deterioration (Lazzari and Scrosati, 1980).

Since then, a variety of transition metals have been tested for their performance for reversible lithium insertion and extraction, finding that both transition metal sulphides and halides were unsuitable due to having low open-circuit voltages and low conductivity, respectively (Padhi, Nanjundaswamy and Goodenough, 1997). The materials used for the electrodes and the electrolyte are an important consideration, as they can have a significant impact on the cell's safety, capacity, and energy density, which are key to the overall practicality for use in electric vehicles. We will consider each part of a cell and discuss the most commonly used materials.

1.3.1 The Cathode

Cathodes require the use of lithium-ion host materials that have high positive redox potentials (Ji et al., 2011). Most current research is focused on the use of transition metals that can readily undergo oxidation and reduction to allow for the extraction and insertion of lithium ions (Rao, 2014). The chosen material must remain structurally stable during the charge and discharge processes in order to minimise the irreversible capacity fade.

The lithium-ion battery released by Sony in 1991 made use of hexagonal-structured lithium cobalt oxide ($LiCoO_2$) as the cathode material. It displayed promising results while also being smaller, lighter, and possessing higher energy density than other designs for rechargeable batteries, such as lead-acid (Li et al., 2009). As such, it is among some of the most commonly used cathode materials. It is usually cycled between fully lithiated and half-lithiated states, which gives a specific capacity of $\sim 150\ \mathrm{mAhg^{-1}}$ and shows potential for a long cycling life (Li et al., 2009). However, a lithium cobalt oxide cathode has safety problems associated with the instability caused by overcharging. On removal of the lithium ions from the electrode (during

the charge process), a possible side reaction is the oxidation of a Co^{+3} ion to Co^{4+} ions, which are unstable and at high concentrations they can irreversibly affect the internal structure of the electrode (Li et al., 2009). Another proposed theory involved the Co^{+3} ions dissolving in the electrolyte, leading to the reduction of the potential capacity with each charge (Fergus, 2010b).

As cobalt is not as readily available as some other transition metals, such as iron and manganese, these electrodes can often only be used in small cells due to the higher costs involved. These cells, while still useful in smaller portable technologies such as mobile phones, are not practical for use in electric vehicles (Rao, 2014).

The development of lithium manganese oxide ($LiMn_2O_4$) as a cathode was first considered in 1981 when Hunter suggested that the spinel structure would be preserved when most of the lithium ions have de-intercalated (Hunter, 1981). In 1983, the first $LiMn_2O_4$ cathode was tested as lithium ions were chemically inserted into the lattice, which caused the reduction of Mn^{4+} to Mn^{3+} (Thackeray et al., 1983).

$LiMn_2O_4$ has improved thermal stability, compared to $LiCoO_2$, and so is much safer with the added benefit of lower manufacture cost while still maintaining a similar theoretical capacity of ~ 148 $mAhg^{-1}$, meaning it has also become one of the leading materials for cathode electrodes. (Rao, 2013). However, at present, the practical capacity has been found to be ~ 120 $mAhg^{-1}$, and the material tends to suffer from capacity fading with repeated charge and discharge cycles. Similarly to the case with $LiCoO_2$, a suggested explanation for this capacity fading is due to the dissolution of the manganese ions in the electrolyte (Arora, White, Doyle, 1998).

Lithium iron phosphate ($LiFePO_4$), another possible compound for use as a cathode, was first proposed in 1996 (Padhi, Nanjundaswamy and Goodenough, 1996). It quickly became a favourable option to explore due to the availability of iron, contributing to lower costs while still possessing a competitive specific capacity ~ 170 $mAhg^{-1}$ and thermal stability (Rao, 2014). Other phosphates have been considered for use as cathodes, such as $LiMnPO_4$ and $LiCoPO_4$, which have higher open-circuit voltages. However, $LiFePO_4$ has the highest theoretical capacity (Fergus, 2010b).

Upon charging, the lithium ions de-intercalate from the cathode, which causes the

oxidation of iron from Fe^{2+} to Fe^{3+}, leaving $FePO_4$ (Padhi, Nanjundaswamy and Goodenough, 1997). The olivine structure is retained in this process, which occurs via two phases and results in one-dimensional lithium-ion transport (Ellis et al., 2007) and a relatively flat discharge curve (Fergus, 2010b).

1.3.2 The Anode

Similar to the cathode, the anode must also remain structurally stable when in use as well as have high conductivity. The material should be strongly reducing to allow for higher open-circuit voltages when paired with a highly oxidising cathode (Xu, 2004). Pure lithium metal has excellent capacity ($\sim$ 3820 $mAhg^{-1}$) and is also strongly reducing (Eftekhari, 2017), but the safety risks involved with its use prevent it from being a practical choice for an anode (Li et al., 2009).

Carbon is a readily available resource, so research on various carbonaceous materials has been a major focus (Wu, Rahm and Holze, 2003). Carbon in the form of graphite (C_6) is the most frequently used material for the anode in commercial lithium-ion batteries. Graphite is made up of layers of structured carbon atoms, called graphene sheets, which allow lithium ions to intercalate reversibly between these layers. The carbon atoms are ordered into a lattice where each atom is only bonded to three others, leaving a free electron and making the material highly conductive along these planes (Ji et al., 2011). The graphene layers have a high surface-area-to-mass ratio, which can contribute to a lower overall weight for the cell while still maintaining a theoretical specific capacity of $\sim$ 372 $mAhg^{-1}$ (Ji et al., 2011).

Past research has also included the use of metal alloys. They often had problems with low cycling life, however the use of nanoparticles of these materials showed some improvements with this problem (Ritchie and Howard, 2006). In addition, nanoparticles allow for larger surface areas and an increased number of active sites for the intercalation of lithium ions. This leads to an increase in energy densities (Ji et al., 2011). The introduction of metal oxides to form composites with graphite or the carbon coating of the electrode can also reduce electrolyte decomposition and therefore improve the cycling behaviour on the first cycle (Wu, Rahm and Holze, 2003).

1.3.3 The Electrolyte

An electrolyte lies between the negative and positive electrodes and often consists of a lithium-based salt dissolved in an organic solvent, which allows the transfer of lithium ions between the electrodes. The safety of the battery is of high importance, therefore the electrolyte should have low flammability and be thermally stable. The electrode-electrolyte interface is vital in influencing the performance of the battery as the electrolyte must retain high stability with both electrodes. This is especially relevant as we push for batteries with higher energy densities by looking for cathodes and anode materials that are more oxidising and reducing (Xu, 2004). This stability is related to the potentials of the electrodes (as discussed in Section 1.2.1), which must both lie within the "electrochemical window" of the electrolyte; if the value for the anode is lower than this window it will reduce the electrolyte while a value for the cathode being too high will cause oxidation of the electrolyte. In both cases, it can cause an irreversible decrease in capacity (Goodenough and Park, 2013).

In an ideal situation, we would be able to find materials that have potentials as close to the limits of the electrolyte's electrochemical window as possible, resulting in a high open-circuit voltage and therefore a high energy density.

However, in some cases, these processes occurring can give the cell an advantage. During the initial charge process, some solvent-based electrolytes will be oxidised/reduced and cause a thin layer to form over the cathode/anode, known as the solid electrolyte interface (SEI) (Verma, Maire and Novák, 2010). This layer then acts as a protective barrier and prevents the process from occurring further while still allowing the lithium ions to intercalate/de-intercalate as before. This process will cause a slight loss in capacity but will avoid further capacity fade during later cycles (Goodenough and Kim, 2010).

Lithium-based electrolytes have been a focus due to their relatively wide electrochemical windows while also having the ability to form stable SEI layers (Goodenough and Kim, 2010). For example, lithium hexafluorophosphate ($LiPF_6$) was first proposed for use as an electrolyte in lithium-ion batteries in 1968 and is now used commercially due to its practicality across a range of properties (Xu, 2004). While $LiPF_6$ does not have the best performance in every requirement for an electrolyte,

it has been a popular choice due to its ability to simultaneously meet many of the requirements to a reasonable degree. For example, while lithium tetrafluoroborate ($LiBF_4$) has a slightly higher ionic mobility, $LiPF_6$ still has the advantage of higher conductivity and the ability to form a more stable SEI layer. Similarly, while lithium hexafluoroarsenate ($LiAsF_6$) has a higher conductivity than both, there were safety concerns due to its relatively high toxicity (Xu, 2004).

1.4 Research into Lithium-Ion Batteries

In addition to the development of suitable electrolyte and electrode materials, there is extensive research into a wide range of methods to improve the performance of lithium-ion batteries, including both experimental and computational work.

Porous electrode theory has been developed by John Newman since 1962; this theory has been applied to various battery systems and fits well with experimental results (Newman and Tiedemann, 1975). Since then, Newman and his colleagues have developed the Doyle-Fuller-Newman model, a popular charge transport model that brings together the equations for the electrodes, electrolyte and reaction kinetics (Doyle, Fuller and Newman, 1993)(Newman et al., 2003)(Fuller, Doyle and Newman, 1994a,b). The DFN model has been at the frontline of charge transport research, with many using the model for studying a specific aspect of an electrochemical cell and also looking to optimise their models for use in complex and extensive problems.

The safety of lithium-ion batteries is an important consideration, especially when looking at use in vehicles. The study of heat and energy generation in different parts of a cell could give insight into safer designs (Richardson and Korotkin, 2021), while the use of mechanical models (Yiding, et al., 2020) and Monte Carlo simulation methods (Zhang et al., 2022) to investigate electrode degradation could predict battery failure.

Experimental work in cell imaging and monitoring can help us understand the complex chemistry behind the redox reactions on an electrode's surface, leading to breakthroughs in new electrode materials and optimising cell performance (Sathiya et al., 2015)(Biton et al., 2016).

These models can give insight into the complex workings of an electrochemical cell, leading the way for batteries to be built with improved performance. In addition, research focused on modelling safety issues could be implemented to predict and prevent causes of battery failure.

1.4.1 Optimising Performance Parameters

Compared to other secondary battery options, Lithium-ion batteries bring higher energy densities and specific energies; these are important factors that contribute to their popularity for energy storage systems. Energy density is defined as the amount of energy a battery contains per unit volume; it is sometimes referred to as volumetric energy density with units WhL^{-1}. Similarly, specific energy can be defined as the amount of energy a battery contains per unit mass. It can also be referred to as gravimetric energy density and has units $Whkg^{-1}$. These energy densities give a measure of how much energy a battery can produce; higher values can store more energy while being smaller and lighter. This property can be important for use in small portable devices where size is a key factor, such as mobile phones, but can be equally useful for electric vehicles where weight might be a consideration.

The first commercial battery by Sony had a gravitational energy density of $80Whkg^{-1}$, however with the significant research since then, energy densities of $> 300Whkg^{-1}$ became attainable (Blomgren, 2017). The development of a lithium-ion battery with a gravitational energy density of $711Whkg^{-1}$ was recently announced, which used a manganese-based material for the cathode and a lithium-metal anode (Li et al., 2023).

One research avenue towards increasing energy densities includes increasing the cell voltage. This is determined by the difference between the 'operating voltages' of the anode and cathode, which is dictated by the voltage at which the oxidation and reduction reactions occur for the selected cathode and anode materials. For higher cell voltages, we need to maximise this difference, but this can prove challenging to do without the electrolyte causing problems; pushing the cell voltage beyond the stable electrochemical window of the electrolyte causes its irreversible decomposition and decreases the battery's cycle life (Chen et al., 2019). Such electrode materials have been researched (Hu et al., 2013)(Li et al., 2017), but new electrolyte options that may be able to support higher voltages are still being studied. Solid

electrolytes are an example (Manthiram, 2017)(Lau et al., 2018); they are typically safer in design but have lower conductivities than liquid electrolytes (Fergus, 2010a).

Increasing the specific capacity of a lithium-ion battery is another way to increase its energy density. Specific capacity is the amount of charge the battery can produce, per unit of mass, when discharged at a given voltage. It is measured in $Ahkg^{-1}$. Similarly, capacity density is the amount of charge the battery can produce per unit of volume (AhL^{-1}). Increasing the capacity means increasing the number of sites on the electrodes where lithium ions are able to reversibly (de)-intercalate and the number of electrons that are able to contribute towards the oxidation/reduction reactions. The challenge is being able to do this while still keeping the battery small and light (Choi and Aurbach, 2016).

To overcome this limitation, research into conversion-reaction electrodes has found possible material options that have shown theoretical specific capacities of up to 5 times greater than those used at present (Meng et al., 2023). These types of electrodes involve oxides of transition metals that were not originally considered possible candidates due to their structures not accepting the intercalation of lithium ions. Instead of intercalation, these materials react to form lithium oxides on the surface of the electrode, however the exact mechanism of these reactions is not yet understood fully (Yu et al., 2015)(Yu et al., 2018). These options still come with significant limitations; these conversion reactions can often cause large structural changes leading to serve capacity fade, even early in the battery's cycle life. Similarly, safety issues can arise due to the use of oxides increasing the risk of unwanted exothermic side reactions leading to thermal runaway (Cabana et al., 2010)(Manthiram, 2017)(Meng et al., 2023).

Currently under research to increase specific capacity include doping, a method where very small quantities of other elements are introduced into the structures of the electrodes with the intention of altering the electrochemical properties to improve performance (Lüder et al., 2017). For example, doping a $LiCoO_2$ electrode with aluminium (Al) and lanthanum (La) was found to help with structural stability when cycling at higher voltages (Liu et al., 2018), while doping cathode materials has been shown to slightly reduce electrolyte decomposition and decrease the release of oxygen (Yan et al., 2020).

1.5 Report Outline

In this thesis, we study the modelling of charge transport throughout different parts of an electrochemical cell. When starting the project, the original plan was to study each part of a cell and consider a charge transport model for each part. Then, to combine these into a model for a full cell that encapsulates the essential charge transport equations and also builds on these ideas to bring new insights or account for more complex behaviour. Completing the full-cell model within the time proved to be too ambitious, but here we present the individual models for the parts of an electrochemical cell with discussion on how they could be combined into a full-cell model in the future.

We begin by focusing on the modelling of charge transport through the electrolyte phase. In Chapter 2, we will briefly outline the Poisson-Nernst-Planck theory and discuss how this can be applied to a model for dilute electrolytes. In this model, we will consider the situation where we have charge neutrality and an ideal solution. While this can be a suitable assumption for the bulk electrolyte, we will investigate in Chapter 3 how to account for non-ideality.

We will introduce the electrochemical potentials of the ionic species in an electrolyte to formulate an alternative model to Chapter 2. We discuss more concentrated electrolytes, where the assumption of an ideal solution does not hold, and interactions between ions become important to consider. We derive a model to account for this by considering partial molar volumes and then give analytical and numerical solutions.

We study models used to account for non-ideal behaviour, such as the Maxwell-Stefan equations and Margules functions. We set up an ion-hopping model where we consider a Monte Carlo algorithm to simulate these ionic interactions and apply these models. We run the simulation for electrolytes using various solvents and compare the results to experimental results from the literature. We focus on calculations for the activity coefficient term, as this is the term that incorporates the deviation from ideality. We make additional amendments to the algorithm and run further simulations to model the formation of solvation shells in the electrolyte.

In Chapter 4, we introduce the Dolye-Fuller-Newman (DFN) model and follow the derivation of a single-particle model that maintains good agreement with the DFN model while reducing computational complexity.

We study the double layer in Chapter 5 and consider the effect it has on the movements of the ions adjacent to the electrode surface. We will investigate the Schrödinger equation and its applications to modelling electrons moving through a potential barrier. We link this to an electrochemical cell by considering the electrons tunnelling through the potential barriers near the electrode surface. We study the effect this could have on Butler-Volmer reaction kinetics and electrode capacity.

In Chapter 6, we will summarise these models and consider developments for future work.

The models studied in Chapters 2 and 3 explore the electrolyte, both dilute and moderately concentrated, while in Chapter 5 we look at the reactions occurring on the surface of the electrodes. Linking these models together would involve considering the fluxes at the electrode surfaces and quantifying how this drives the reaction rates of the redox reactions and explains the Butler-Volmer kinetics. This could also give more insight into our study of electron tunnelling. Additionally, a further model of the charge transport occurring within the electrode materials, such as diffusion into the particles, could complete the full cell model.

A full cell model could prove to be computationally expensive, so here we link to the work in Chapter 4 where we considered a single particle model from the literature as an alternative formulation that has proved to be significantly quicker to solve while maintaining good agreement. This gives insight into how we could follow a similar process to reduce the complexity of our models without reducing accuracy, which would allow the inclusion of more complex behaviour, such as applying a similar asymptotic analysis to better understand the double layer behaviour.

2 Models for Dilute Electrolytes

2.1 Poisson-Nernst-Planck Theory

To begin to model the movements of the ions in the electrolyte we will first consider the Poisson-Nernst-Planck theory which can be used for the modelling of dilute electrolytes. Following the derivation found in (Richardson and King, 2007), we first consider the movement of the ions due to diffusion and under the influence of the electric field, so we proceed by deriving the diffusive and advective fluxes of the positive and negative ion species.

2.1.1 The Electric Potential

By assuming the electric field is irrotational, it can therefore be written in terms of the electric potential, ϕ:

$$\nabla \times \mathbf{E} = 0 \quad \Longrightarrow \quad \mathbf{E} = -\nabla\phi. \tag{2.1}$$

Applying the differential form of Gauss's law, we get Poisson's equation:

$$\nabla.\mathbf{E} = \frac{\rho}{\epsilon} \quad \Longrightarrow \quad \nabla.(\epsilon\nabla\phi) = -\rho, \tag{2.2}$$

where ρ is charge density and ϵ is the permittivity of the electrolyte, which we will assume to be constant. This allows us to rewrite [2.2] in terms of the concentrations of the two ionic species (Bazant, Thornton and Ajdari, 2004):

$$\nabla^2\phi = \frac{-\rho}{\epsilon} = \frac{F}{\epsilon}(c_n - c_p), \tag{2.3}$$

where F is Faraday's constant, c_n and c_p are the concentrations of the negative and positive species.

2.1.2 The Flux of the Ionic Species

To consider the fluxes of the ions in the electrolyte, the positive lithium ions (Li^+) and a general negative ion denoted as N^-, we need to allow for their diffusive movement due to the concentration gradient and their advective movement due to the electric field. We will denote the concentration of each species as c_i and each flux as $\mathbf{q}_i$, where $i = n, p$ for the negative and positive species.

The Diffusive Flux: To find the diffusive flux of an ionic species, we use Fick's 1^{st} law of diffusion:

$$\mathbf{q}_{d_i} = -D_i \nabla c_i, \tag{2.4}$$

where $\mathbf{q}_{d_i}$, the diffusive flux of species i, is proportional to the concentration gradient of that species with D as the diffusion coefficient. The negative sign here denotes the fact that the ions will flow from areas of high concentration towards areas of low concentration, therefore flowing against the concentration gradient. Values for the diffusion coefficient often fall around the range $10^{-10} - 10^{-9}$ $\mathrm{m^2 s^{-1}}$ (Atkins and De Paula, 2014).

The Advective Flux: The advective flux for each species is given by:

$$\mathbf{q}_{a_i} = c_i \mathbf{v}_{a_i}, \tag{2.5}$$

where $\mathbf{v}_{a_i}$ is the velocity of species i due to the electric field.

We begin by considering the forces acting on a single ion. Each ion will experience a force from the electric field, $\mathbf{F}_{e_i}$ given by equation [2.6]. We can then use [2.1] to write in terms of the electric potential. The ez_i term allows for the charge of the ion where $e \sim 1.602 \times 10^{-19}$ C is the charge of a single proton, known as the elementary charge.

$$\mathbf{F}_{e_i} = ez_i \mathbf{E} = -ez_i \nabla \phi. \tag{2.6}$$

This force will cause the ion to move through the electrolyte towards the electrode of the opposite charge. This movement will then cause the electrolyte to exert a drag force, $\mathbf{F}_{d_i}$ given by equation [2.7], on the ion until it reaches a terminal drift velocity, $\mathbf{v}_{a_i}$, with the drag coefficient K_{d_i}:

$$\mathbf{F}_{d_i} = K_{d_i} \mathbf{v}_{a_i}. \tag{2.7}$$

This drift velocity is reached when these two forces are balanced, so we find the following relation:

$$-ez_i \nabla \phi = K_{d_i} \mathbf{v}_{a_i} \quad \Longrightarrow \quad \mathbf{v}_{a_i} = -\frac{ez_i}{K_{d_i}} \nabla \phi, \tag{2.8}$$

where the drift velocity of the ion is proportional to the strength of the electric field.

We can now introduce the concept of mobility, which gives a measure of how easily an ion moves through the electrolyte while under the influence of the electric field. We can relate the mobility of an ion to the drag coefficient, leading to:

$$M_i = \frac{1}{K_{d_i}} \quad \Longrightarrow \quad \mathbf{v}_{a_i} = -ez_i M_i \nabla\phi. \tag{2.9}$$

Therefore, by substituting [2.9] into [2.5] for each species of ion, we find the following advective fluxes:

$$\mathbf{q}_{a_i} = -c_i e z_i M_i \nabla\phi, \tag{2.10}$$

The Einstein Relation: We can also link the mobility of the ion to the diffusion coefficient by the following relation:

$$M_i = \frac{D_i}{k_B T}, \tag{2.11}$$

where $k_B \sim 1.381 \times 10^{-23}$ $\mathrm{kg\,s^{-2}\,K^{-1}}$ is the Boltzmann's constant, and T is the absolute temperature.

We can now take the fact that the elementary charge can be written in terms of Faraday's constant and Avogadro's constant, $N_A \sim 6.022 \times 10^{23}$ $\mathrm{mol^{-1}}$:

$$e = \frac{F}{N_A}, \tag{2.12}$$

where Avogadro's constant can also give the relation between the universal gas constant, $R_g \sim 8.314$ $\mathrm{J\,mol^{-1}K^{-1}}$, and the Boltzmann's constant as:

$$R_g = k_B N_A. \tag{2.13}$$

Combining equations [2.12] and [2.13] we find the relation:

$$\frac{e}{k_B} = \frac{F}{R_g}, \tag{2.14}$$

which can be substituted into the advective flux [2.10] to give:

$$\mathbf{q}_{a_i} = -z_i c_i \frac{F D_i}{R_g T} \nabla\phi \tag{2.15}$$

The total flux for each ion species is now given by the sum of its respective diffusive [2.4] and advective parts [2.15], giving:

$$\mathbf{q}_i = -D_i\big(\nabla c_i + z_i c_i \frac{F}{R_g T}\nabla\phi\big), \qquad [2.16]$$

Using the assumption that the species of ion will not interact with each other, the electrolyte will behave as an ideal solution, we can also introduce equations for the conservation of each ion species:

$$\frac{\partial c_i}{\partial t} + \nabla.\mathbf{q}_i = 0. \qquad [2.17]$$

Bringing together equations [2.3], [2.16] and [2.17] we have the general equations for the model. We will now look at how this model can be applied to a dilute electrolyte in 1-dimension.

2.2 A 1D Model for Dilute Electrolytes

Consider a single electrode with its surface located at $x = 0$, immersed in a $1:1$ binary electrolyte which spans the region $0 < x < L$. A binary electrolyte is one composed of a single compound that dissociates into one positive ion and one negative ion, which have charges z_p and z_n such that $z_n = -z_p$ (Newman and Thomas-Alyea, 2004). In the case that $z_p = +1$ and $z_n = -1$ we have a $1:1$ electrolyte (e.g. $LiPF_6$ dissociates into Li^+ ions and $PF_6{}^-$ ions). We will be considering a 1-dimensional model, where the x-direction represents the distance from the electrode surface.

The use of this 1-dimensional set-up simplifies the equation for the electric field [2.1] to:

$$\mathbf{E} = -\frac{\partial\phi}{\partial x}\mathbf{e}_x, \qquad [2.18]$$

and equations [2.3], [2.16] and [2.17] now become:

$$\frac{\partial^2\phi}{\partial x^2} = \frac{F}{\epsilon}(c_n - c_p), \qquad [2.19]$$

$$q_n = -D_n\left(\frac{\partial c_n}{\partial x} - c_n\frac{F}{R_gT}\frac{\partial \phi}{\partial x}\right), \quad [2.20] \qquad \frac{\partial c_n}{\partial t} + \frac{\partial q_n}{\partial x} = 0, \quad [2.21]$$

$$q_p = -D_p\left(\frac{\partial c_p}{\partial x} + c_p\frac{F}{R_gT}\frac{\partial \phi}{\partial x}\right), \quad [2.22] \qquad \frac{\partial c_p}{\partial t} + \frac{\partial q_p}{\partial x} = 0. \quad [2.23]$$

where we have expanded equations [2.16] and [2.17] for each ion species, $i = n, p$.

Equations [2.20] - [2.23] are often referred to as the Nernst-Planck equations for flux, and together with Poisson's equation they are known as the Poisson-Nernst-Planck theory.

2.2.1 Charge Neutrality

As we are considering a electrolyte that acts as an ideal solution, it is usual to assume charge neutrality in the bulk electrolyte. This leads to the assumption that the concentrations of the positive and negative species are equal. To justify this, we begin by non-dimensionalising equations [2.19] - [2.23] using the following scalings (Richardson and King, 2007):

$$x = L\hat{x}, \quad t = \frac{L^2}{D}\hat{t}, \quad c_n = c_0\hat{c}_n, \quad c_p = c_0\hat{c}_p, \quad [2.24]$$

$$q_n = \frac{D}{L}c_0\hat{q}_n, \quad q_p = \frac{D}{L}c_0\hat{q}_p, \quad \phi = \frac{R_gT}{F}\hat{\phi}. \quad [2.25]$$

Here, we are scaling x by an approximate length for an electrochemical cell, L, where c_0 represents typical electrolyte concentration and D gives the typical scale of the diffusion coefficients D_n and D_p. We also need to consider a suitable value for ϵ, the permittivity of the electrolyte, which is typical given in terms of the permittivity of free space such that $\epsilon = \epsilon_r\epsilon_0$, where ϵ_r is the relative permittivity. For a dilute electrolyte, the salt is not considered to have too much of an impact on permittivity so often can be taken as similar to the permittivity of water, which is given by $80\epsilon_0 = 7.0834\text{x}10^{-10}\ Fm^{-1}$ (Richardson and King, 2007). Values for

these parameters are given in Table 1.

Applying these scalings leads to:

$$\frac{R_gT}{FL^2}\frac{\partial^2\hat{\phi}}{\partial\hat{x}^2} = \frac{F}{\epsilon}(c_0\hat{c}_n - c_0\hat{c}_p), \qquad [2.26]$$

$$\frac{D}{L}c_0\hat{q}_n = -D_n\left(\frac{c_0}{L}\frac{\partial\hat{c}_n}{\partial\hat{x}} - c_0\hat{c}_n\frac{F}{R_gT}\frac{R_gT}{FL}\frac{\partial\hat{\phi}}{\partial\hat{x}}\right), \qquad [2.27]$$

$$\frac{D}{L}c_0\hat{q}_p = -D_p\left(\frac{c_0}{L}\frac{\partial\hat{c}_p}{\partial\hat{x}} + c_0\hat{c}_p\frac{F}{R_gT}\frac{R_gT}{FL}\frac{\partial\hat{\phi}}{\partial\hat{x}}\right), \qquad [2.28]$$

$$\frac{Dc_0}{L^2}\frac{\partial\hat{c}_n}{\partial\hat{t}} + \frac{D}{L^2}c_0\frac{\partial\hat{q}_n}{\partial\hat{x}} = 0, \qquad [2.29]$$

$$\frac{Dc_0}{L^2}\frac{\partial\hat{c}_p}{\partial\hat{t}} + \frac{D}{L^2}c_0\frac{\partial\hat{q}_p}{\partial\hat{x}} = 0, \qquad [2.30]$$

which simplifies to:

$$\frac{\epsilon R_gT}{F^2L^2c_0}\frac{\partial^2\hat{\phi}}{\partial\hat{x}^2} = (\hat{c}_n - \hat{c}_p), \qquad [2.31]$$

$$\hat{q}_n = -\frac{D_n}{D}\left(\frac{\partial\hat{c}_n}{\partial\hat{x}} - \hat{c}_n\frac{\partial\hat{\phi}}{\partial\hat{x}}\right), \qquad [2.32]$$

$$\frac{\partial\hat{c}_n}{\partial\hat{t}} + \frac{\partial\hat{q}_n}{\partial\hat{x}} = 0, \qquad [2.33]$$

$$\hat{q}_p = -\frac{D_p}{D}\left(\frac{\partial\hat{c}_p}{\partial\hat{x}} + \hat{c}_p\frac{\partial\hat{\phi}}{\partial\hat{x}}\right), \qquad [2.34]$$

$$\frac{\partial\hat{c}_p}{\partial\hat{t}} + \frac{\partial\hat{q}_p}{\partial\hat{x}} = 0. \qquad [2.35]$$

We can rewrite these equations by introducing new variables:

$$\lambda^2\frac{\partial^2\hat{\phi}}{\partial\hat{x}^2} = (\hat{c}_n - \hat{c}_p), \qquad [2.36]$$

$$\hat{q}_n = -\alpha\left(\frac{\partial\hat{c}_n}{\partial\hat{x}} - \hat{c}_n\frac{\partial\hat{\phi}}{\partial\hat{x}}\right), \qquad [2.37]$$

$$\frac{\partial\hat{c}_n}{\partial\hat{t}} + \frac{\partial\hat{q}_n}{\partial\hat{x}} = 0, \qquad [2.38]$$

$$\hat{q}_p = -\beta\left(\frac{\partial \hat{c}_p}{\partial \hat{x}} + \hat{c}_p \frac{\partial \hat{\phi}}{\partial \hat{x}}\right), \qquad [2.39] \qquad \frac{\partial \hat{c}_p}{\partial \hat{t}} + \frac{\partial \hat{q}_p}{\partial \hat{x}} = 0, \qquad [2.40]$$

where we have used:

$$\alpha = \frac{D_n}{D}, \qquad \beta = \frac{D_p}{D}, \qquad \lambda = \frac{1}{L}\sqrt{\frac{\epsilon R_g T}{F^2 c_0}}. \qquad [2.41]$$

We can relate λ to the Debye length, which gives the thickness of a region termed the double layer; a region adjacent to an electrode where charge neutrality is not satisfied. The Debye length of an electrolyte is given by (Newman and Thomas-Alyea, 2004):

$$L_d = \sqrt{\frac{\epsilon R_g T}{F^2 c_0}}, \qquad [2.42]$$

therefore comparing to [2.41], we find the relation:

$$\lambda = \frac{L_d}{L}. \qquad [2.43]$$

Table 1: Values and descriptions of parameters introduced in equations [2.24] - [2.25] and the derived dimensionless parameter for λ from equation [2.41].

Parameter	Description	Value	Reference
c_0	Salt concentration of the electrolyte	1000 $mol\ m^{-3}$	(Richardson and King, 2007)
ϵ	Permittivity of the electrolyte	$80\epsilon_0 = 7.0834\text{x}10^{-10}\ Fm^{-1}$	(Richardson and King, 2007)
D	Diffusivity of the electrolyte	$5.34\text{x}10^{-}10\ m^2\ s^{-1}$	(Srinivasan, and Newman, 2004)
L	Length of the electrochemical cell	$1.6\text{x}10^{-4}\ m$	(Ecker et al., 2015)
L_d	Debye length	$4.342\text{x}10^{-10}\ m$	Calculated from [2.42]
λ	Relation between Debye length and cell length	$2.714\text{x}10^{-6}$	Calculated from [2.41]c)
T	Temperature	298 K	(Srinivasan, and Newman, 2004)

Typically, the scale of the Debye layer is much smaller than the scale of the whole cell (Ranom, 2014). This can be seen by the values of λ, L and L_d in Table 1 where $\lambda << 1$ and $L_d << L$. This allows us to set the left side of equation [2.36] to 0, therefore we can impose:

$$\hat{c}_n - \hat{c}_p \approx 0 \qquad \Longrightarrow \qquad \hat{c}_n \approx \hat{c}_p, \tag{2.44}$$

so we can then denote:

$$\hat{c}_n = \hat{c}_p = \hat{c}, \tag{2.45}$$

which gives rise to the following equations:

$$\hat{q}_n = -\alpha\left(\frac{\partial \hat{c}}{\partial \hat{x}} - \hat{c}\frac{\partial \hat{\phi}}{\partial \hat{x}}\right), \tag{2.46}$$

$$\frac{\partial \hat{c}}{\partial \hat{t}} + \frac{\partial \hat{q}_n}{\partial \hat{x}} = 0, \tag{2.47}$$

$$\hat{q}_p = -\beta\left(\frac{\partial \hat{c}}{\partial \hat{x}} + \hat{c}\frac{\partial \hat{\phi}}{\partial \hat{x}}\right), \tag{2.48}$$

$$\frac{\partial \hat{c}}{\partial \hat{t}} + \frac{\partial \hat{q}_p}{\partial \hat{x}} = 0. \tag{2.49}$$

To make a further simplification, we can consider setting the diffusion coefficient of the positive ion species equal to the typical value, $D_p = D$. This leads to altering the scalings for t, q_n and q_p to:

$$t = \frac{L^2}{D_p}\hat{t}, \quad q_n = \frac{D_p}{L}c_0\hat{q}_n, \quad q_p = \frac{D_p}{L}c_0\hat{q}_p, \tag{2.50}$$

and changes α and β to:

$$\alpha = \frac{D_n}{D_p}, \qquad \beta = \frac{D_p}{D_p} = 1, \tag{2.51}$$

where α now represents the ratio of the positive and negative diffusivities.

Substituting [2.51] into [2.46] - [2.49], we find:

$$\hat{q}_n = -\frac{D_n}{D_p}\left(\frac{\partial \hat{c}}{\partial \hat{x}} - \hat{c}\frac{\partial \hat{\phi}}{\partial \hat{x}}\right), \tag{2.52}$$

$$\frac{\partial \hat{c}}{\partial \hat{t}} + \frac{\partial \hat{q}_n}{\partial \hat{x}} = 0, \tag{2.53}$$

$$\hat{q}_p = -\left(\frac{\partial \hat{c}}{\partial \hat{x}} + \hat{c}\frac{\partial \hat{\phi}}{\partial \hat{x}}\right), \qquad [2.54] \qquad \frac{\partial \hat{c}}{\partial \hat{t}} + \frac{\partial \hat{q}_p}{\partial \hat{x}} = 0. \qquad [2.55]$$

Here, we are still treating the negative and positive ions as diffusing independently of each other. Another possible approach is to consider the diffusivity of the electrolyte as a whole, with the positive and negative ions contributing to this diffusivity due to their movements. This is known as ambipolar diffusion, which gives a measure of the effective diffusivity of the electrolyte.

2.2.2 Ambipolar Diffusion

Now that we are only considering one variable for the concentration, we can combine [2.46] - [2.49] to reduce the number of equations. To start we consider the conservation equations [2.47] and [2.49]; it follows that:

$$\beta\left(\frac{\partial \hat{c}}{\partial \hat{t}} + \frac{\partial \hat{q}_n}{\partial \hat{x}}\right) + \alpha\left(\frac{\partial \hat{c}}{\partial \hat{t}} + \frac{\partial \hat{q}_p}{\partial \hat{x}}\right) = 0. \qquad [2.56]$$

On substituting the fluxes [2.46] and [2.48] into the conservation equations [2.56] we find:

$$\beta\left(\frac{\partial \hat{c}}{\partial \hat{t}} - \alpha\left(\frac{\partial^2 \hat{c}}{\partial \hat{x}^2} - \frac{\partial \hat{c}}{\partial \hat{x}}\frac{\partial \hat{\phi}}{\partial \hat{x}} - \hat{c}\frac{\partial^2 \hat{\phi}}{\partial \hat{x}^2}\right)\right) + \alpha\left(\frac{\partial \hat{c}}{\partial \hat{t}} - \beta\left(\frac{\partial^2 \hat{c}}{\partial \hat{x}^2} + \frac{\partial \hat{c}}{\partial \hat{x}}\frac{\partial \hat{\phi}}{\partial \hat{x}} + \hat{c}\frac{\partial^2 \hat{\phi}}{\partial \hat{x}^2}\right)\right) = 0, \qquad [2.57]$$

which therefore simplifies down to:

$$\frac{\partial \hat{c}}{\partial \hat{t}} - \delta\frac{\partial^2 \hat{c}}{\partial \hat{x}^2} = 0, \qquad [2.58]$$

where we have defined a dimensionless form of the effective diffusivity:

$$\delta = \frac{2\alpha\beta}{\alpha + \beta} = \frac{2D_nD_p}{D(D_n + D_p)} = \frac{D_{eff}}{D}. \qquad [2.59]$$

Equation [2.59], which can be termed the ambipolar diffusion equation, shows how the two ion species diffuse together as though they are a single neutral species, this results directly from the assumption of charge neutrality so therefore is only applicable to bulk electrolytes (Schmuck and Bazant, 2015). This effect can be seen

more clearly if we consider an electrolyte containing ions with unequal charges.

In general, the effective diffusivity in the dilute limit can be written as:

$$D_{eff} = \frac{(z_p - z_n)D_n D_p}{(z_p D_p - z_n D_n)}, \qquad [2.60]$$

where z_n and z_p are the charges of the negative and positive species respectively. Rewriting equation [2.60] as:

$$\frac{1}{D_{eff}} = \frac{z_p}{D_n(z_p - z_n)} - \frac{z_n}{D_p(z_p - z_n)}, \qquad [2.61]$$

we can see that D_{eff} is measure of the average diffusivity, weighted by the ratio of the charges. The ion with the larger magnitude of charge will have a larger advective flux and so will have a tendency to diffuse at a faster rate, however the effective diffusivity will be influenced more by the ion with the smaller magnitude of charge (and smaller diffusivity) in order prevent the ion species from separating too far, to maintain charge neutrality in the solution (Ghosal and Chen, 2010).

2.2.3 Discussion

In this section, we have presented a 1D model for a dilute electrolyte using Poisson-Nernst-Planck theory to describe the effect of the electric field and concentration gradient on the fluxes of the positive and negative ionic species. In Section 2.1, we set up a general form of the model as:

$$\nabla^2 \phi = \frac{F}{\epsilon}(c_n - c_p), \qquad [2.62]$$

$$\mathbf{q}_i = -D_i\big(\nabla c_i + z_i c_i \frac{F}{R_g T}\nabla\phi\big), \qquad [2.63]$$

$$\frac{\partial c_i}{\partial t} + \nabla.\mathbf{q}_i = 0. \qquad [2.64]$$

In Section 2.2, we opted to study a 1:1 binary electrolyte, where the charges of the ions are $z_n = -1, z_p = 1$, leading to a simplification of equation [2.63]. We also chose to reduce the model to 1-dimension, with the x-direction measuring the distance from the electrode (which is located at $x = 0$), this represents a horizontal cross-section taken from Figure 1.

The original Doyle-Fuller-Newman model considers 1-dimensional lithium transport between the anode and the cathode (Doyle et al., 1993), this comes from the assumption that the chemistries and structures of the electrodes and electrolyte are consistent throughout the 3D material and therefore taking a 1D cross-section or a 2D cross-section either horizontally or vertically is representative of any other cross-section (Nonner and Eisenberg, 1998)(Liu, 2009). The only exception to this is at the boundaries of the structure (other than where the electrodes are). In reality, these boundaries could lead to slight turbulent and unpredictable movements in the electrolyte, we will discuss the effects of this and methods to model this in Chapter 3.

Similarly, interactions between the charged ions could cause movements in all three dimensions, however in the dilute limit it is typical to neglect these ionic interactions, therefore we expect the concentration gradient to only vary significantly across the x-direction (Lagnoni et al., 2022). In Chapter 3, we will study more concentrated electrolytes where we will consider the interactions between ions, this will lead to looking at the electrolyte in 2D.

Here, we only included one electrode, located at $x = 0$, as we were interested in studying the difference in behaviour close to and far from this electrode. The inclusion of a second electrode located at $x = L$ and then applying a current across the cell would result in the following boundary conditions on the fluxes (Subramaniam, 2019):

$$q_n|_{x=0} = 0, \qquad q_n|_{x=L} = 0, \tag{2.65}$$

$$q_p|_{x=0} = R_0, \qquad q_p|_{x=L} = R_L, \tag{2.66}$$

where the fluxes of the negative ions are still 0 as these ions are not (de)-intercalated into the electrodes, while the positive lithium ions will (de)-intercalate at a rate determined by the reaction occurring at that electrode. Here we have denoted the reaction rates as R_0 and R_L for the electrodes located at $x = 0$ and $x = L$, respectively. We will look at a full-cell model in Chapter 4.

An important factor for an electrolyte is the lithium salt's ability to dissociate into ions (for example Lithium hexafluorophosphate ($LiPF_6$) dissociates into Li^+ and PF_6^- ions). If the lithium salt dissociates fully into ions, the solution is known as a strong solution, whereas one that only partially dissociates is known as a weak

solution. A solution with more dissociated ions leads to the ability for more charge to be carried and therefore high conductivities. It is for this reason commercial lithium-ion batteries opt to use strong solutions for the electrolyte.

Poisson-Nernst-Planck theory shows good agreement in the bulk electrolyte, but only shows agreement in the double layer when considering weak electrolytes. For strong electrolytes it tends to predict much higher concentrations than are typically possible; it has been argued this is due to neglecting the solvent molecules. Accounting for these solvent molecules along with an incompressibility condition enforces a conservation of volume and therefore ensures the model doesn't predict higher concentrations than can realistically fit into the space. This can be seen in (Richardson and King, 2007), and we will study this concept in Chapter 3.

3 Moderately Concentrated Electrolytes

In the previous chapter, we considered dilute electrolytes and assumed they behaved as an ideal solution. This allowed us to state the resulting equations in terms of the concentration of the ionic species. In this chapter, we will discuss this assumption in relation to concentrated electrolytes and how this affects the equations we previously derived.

We start by defining chemical and electrochemical potentials and how these relate to ideal solutions and then discuss the differences to non-ideal solutions. This motivates a look into the Stefan-Maxwell equations and Margules functions to model for moderately concentrated electrolytes (Newman et al., 2003), where we must also consider the activity terms. We will use these equations to consider how we can build a model based on ions hopping on a lattice to develop a Monte Carlo simulation to describe the ionic movements where we take into account these interactions between different ionic species.

3.1 Gibbs Free Energy and Chemical Potentials

Recall equations [1.1] and [1.2], where we can define Gibbs free energy, G of a mixture, as:

$$G = H - TS = U + pV^* - TS, \tag{3.1}$$

where H is the enthalpy, U is the internal energy, S is entropy, p is pressure, V^* is volume, and T is the absolute temperature.

Next, we can define the chemical potential, which is often referred to as the partial molar Gibbs energy and can be written as (Atkins and De Paula, 2014):

$$\mu_i = \left.\frac{\partial G}{\partial n_i}\right|_{p,T,n_{j,j\neq i}}, \tag{3.2}$$

where n_i is a measure of the amount of species i and we are holding the pressure, temperature and the amounts of all other species constant. The chemical potential

describes how the Gibbs free energy will change when the composition of the mixture changes.

The total Gibbs free energy of a solution is the sum of the partial Gibbs free energies of each species multiplied by the amount of that species that is present, therefore we can define G as:

$$G = \sum_i \frac{\partial G}{\partial n_i}\bigg|_{p,T,n_j,j\neq i} n_i = \sum_i \mu_i n_i. \qquad [3.3]$$

If we change the composition of the solution, the change in Gibbs free energy is therefore given by:

$$dG = \sum_i d\mu_i n_i + \sum_i \mu_i dn_i. \qquad [3.4]$$

Similarly, if we take equation [3.1] and consider the change in Gibbs free energy

$$dG = dU + d(pV^*) - d(TS) = dU + pdV^* + V^*dp - TdS - SdT, \qquad [3.5]$$

while holding pressure and temperature constant, we find:

$$dG = dU + pdV^* - TdS. \qquad [3.6]$$

We can rewrite equation [3.6] in terms of the change in internal energy, dU, and introduce the chemical potential from equation [3.2], where we have written the Gibbs free energy in terms of the solution's components, n_i (Moran and Shapiro, 2006):

$$dU = TdS - pdV^* + \sum_i \mu_i dn_i. \qquad [3.7]$$

We can now substitute in for dU using [3.7] into equation [3.6], we are left with:

$$dG = \sum_i \mu_i dn_i - SdT + V^*dp. \qquad [3.8]$$

Combining equations [3.8] and [3.4] and cancelling terms, we find:

$$V^* dp - S dT = \sum_i d\mu_i n_i, \qquad [3.9]$$

and therefore under constant temperature and pressure we find the Gibbs-Duhem equation [3.10], which shows how the chemical potentials of different species in a solution are not independent of each other: an increase in one will lead to a decrease in another.

$$\sum_i d\mu_i n_i = 0. \qquad [3.10]$$

We can use a similar approach to find a relation between the mole fraction and partial molar volumes of a solution. For a solution of volume V, the partial molar volume for species i can be defined as (Atkins and De Paula, 2014):

$$V_i^* = \frac{\partial V^*}{\partial n_i}. \qquad [3.11]$$

This implies the relation:

$$dV^* = \sum_i V_i^* dn_i, \qquad [3.12]$$

where we can then integrate to give:

$$V^* = \sum_i V_i^* n_i. \qquad [3.13]$$

Similarly to [3.10], [3.13] gives a relation between the amounts of each species that can occupy a given volume: an increase in the amount of one species therefore leads to a decrease in the amount for the other.

3.2 Electrochemical Potentials

In Chapter 2, we set up a model for electrolytes using the Poisson-Nernst-Planck theory. Here, we will briefly consider how to define similar equations using electrochemical potentials. The electrochemical potential is closely related to the chemical potential; the chemical potential describes the difference in free energy with changing composition while the electrochemical potential accounts for this term as well as the energy change from external effects such as an electric field.

As before, we will denote the positive and negative species' concentrations as c_p and c_n and their charges as z_p and z_n, with the addition of the concentration of the neutral ($z_s = 0$) solvent species as c_s.

We can write the electrochemical potential, $\bar{\mu}_i$, of a species as:

$$\bar{\mu}_i = \mu_i + z_i F \phi, \tag{3.14}$$

where F is Faraday's constant and μ_i is the chemical potential of the species. The chemical potential of a species can also be written in terms of its activity:

$$\mu_i = \mu_i^0 + R_g T \ln(a_i), \tag{3.15}$$

where μ_i^0 is the chemical potential of the species under standard conditions and a_i is the activity (Bard and Faulkner, 2001), which itself can be written in terms of the activity coefficient γ_i and the mole fraction χ_i:

$$a_i = \gamma_i \chi_i. \tag{3.16}$$

The mole fraction gives the ratio of the concentration of the species to the total concentration of the solution:

$$\chi_i = \frac{c_i}{c_T}, \tag{3.17}$$

where, for the species $i = n, p, s$:

$$c_T = \sum_i c_i = c_n + c_p + c_s, \tag{3.18}$$

and therefore we can conclude that:

$$\sum_i \chi_i = 1. \tag{3.19}$$

When considering dilute electrolytes it is usual to assume the solution behaves ideally. In this limit, the activity coefficient $\gamma_i \to 1$, and so the activity can simply be replaced with the mole fraction terms (Mortimer, 2008).

Combining [3.14], [3.15] and [3.16], we can write the electrochemical potentials as:

$$\bar{\mu}_n = \mu_n^0 + R_g T \ln(\chi_n) + z_n F \phi, \quad [3.20]$$

$$\bar{\mu}_p = \mu_p^0 + R_g T \ln(\chi_p) + z_p F \phi, \quad [3.21]$$

$$\bar{\mu}_s = \mu_s^0 + R_g T \ln(\chi_s), \quad [3.22]$$

which can be combined with equations [2.17] and a similar conservation equation for the solvent, to give an alternative form of equations [2.16] and [2.17]

$$\mathbf{q}_n = -c_n \frac{D_n}{R_g T} \nabla \bar{\mu}_n, \quad [3.23] \qquad \frac{\partial c_n}{\partial t} + \nabla . \mathbf{q}_n = 0, \quad [3.24]$$

$$\mathbf{q}_p = -c_p \frac{D_p}{R_g T} \nabla \bar{\mu}_p, \quad [3.25] \qquad \frac{\partial c_p}{\partial t} + \nabla . \mathbf{q}_p = 0, \quad [3.26]$$

$$\mathbf{q}_s = -c_s \frac{D_s}{R_g T} \nabla \bar{\mu}_s, \quad [3.27] \qquad \frac{\partial c_s}{\partial t} + \nabla . \mathbf{q}_s = 0. \quad [3.28]$$

We would expect these equations will hold when considering an ideal solution; in general a model for a dilute electrolyte will be assumed to be an ideal solution and so the above equations can be used.

3.3 A Model Using Electrochemical Potentials

Following on from Chapter 2, we can also derive a model for the concentration profile through the electrolyte using the electrochemical potentials for the charged ion species and neutral solvent species.

We will again consider a one-dimensional model for a positive electrode immersed in a $1:1$ binary electrolyte that contains positive lithium ions (Li^+), general negative ions (N^-) with charges ± 1 and a general neutral solvent species. With this setup, equations [3.20] - [3.28] simplify to:

$$q_n = -\frac{D_n}{R_g T} c_n \frac{\partial \mu_n}{\partial x}, \quad [3.29]$$

$$q_p = -\frac{D_p}{R_g T} c_p \frac{\partial \mu_p}{\partial x}, \quad [3.30]$$

$$q_s = -\frac{D_s}{R_g T} c_s \frac{\partial \mu_s}{\partial x}, \quad [3.31]$$

$$\mu_n = \mu_n^0 + R_g T \ln(\chi_n) - F\phi, \quad [3.32]$$

$$\mu_p = \mu_p^0 + R_g T \ln(\chi_p) + F\phi, . \quad [3.33]$$

$$\mu_s = \mu_s^0 + R_g T \ln(\chi_s). \quad [3.34]$$

3.3.1 Analytical Solutions

Considering the case where the flux of each species is 0, we will therefore set $q_i = 0$ for $i = n, p, s$. To avoid the trivial solution of all concentrations being 0, we find that the derivative of each electrochemical potential must be 0. This allows us to write:

$$R_g T \ln\left(\frac{c_n}{c_T}\right) - F\phi = A, \quad [3.35]$$

$$R_g T \ln\left(\frac{c_p}{c_T}\right) + F\phi = B, \quad [3.36]$$

$$R_g T \ln\left(\frac{c_s}{c_T}\right) = C, \quad [3.37]$$

where we have used [3.17] to substitute in for the mole fraction of each species. Solving for each concentration and combining the constant terms, we find:

$$c_n = \tilde{A} c_T e^{\frac{F}{R_g T}\phi}, \quad [3.38]$$

$$c_p = \tilde{B} c_T e^{-\frac{F}{R_g T}\phi}, \quad [3.39]$$

$$c_s = \tilde{C} c_T. \quad [3.40]$$

We can see from equation [3.17], that equation [3.40] is equivalent to a constant mole fraction for the solvent species, therefore we know that at any point x from the electrode, the concentration of the solvent relative to the total concentration,

c_T will always be the same.

Combining these equations with the one-dimensional form of [2.3], [3.13], and [3.18]:

$$\frac{\partial^2 \phi}{\partial x^2} = \frac{F}{\varepsilon}(c_n - c_p), \tag{3.41}$$

$$c_T = c_n + c_p + c_s, \tag{3.42}$$

$$V_n^* c_n + V_p^* c_p + V_s^* c_s = 1. \tag{3.43}$$

We again will non-dimensionalise these equations, using similar scalings to Section 2.2.1, these are shown in Table 2 where this time we will also scale the solvent concentration c_s and total concentration c_T by the typical electrolyte concetration c_0.

$$x = L\hat{x}, \quad c_n = c_0\hat{c}_n, \quad c_p = c_0\hat{c}_p, \quad c_s = c_0\hat{c}_s, \quad \phi = \frac{R_g T}{F}\hat{\phi}. \tag{3.44}$$

Table 2: Values and descriptions of parameters introduced in equation [3.44] and the derived dimensionless parameter for λ from equation [2.41].

Parameter	Description	Value	Reference
c_0	Salt concentration of the electrolyte	1000 $mol\ m^{-3}$	(Richardson and King, 2007)
ϵ	Permittivity of the electrolyte	$80\epsilon_0 = 7.0834\text{x}10^{-10}\ Fm^{-1}$	(Richardson and King, 2007)
D	Diffusivity of the electrolyte	5.34x10$^-$10 $m^2\ s^{-1}$	(Srinivasan, and Newman, 2004)
L	Length of the electrochemical cell	$1.6\text{x}10^{-4}\ m$	(Ecker et al., 2015)
L_d	Debye length	$4.342\text{x}10^{-10}\ m$	Calculated from [2.42]
λ	Relation between Debye length and cell length	$2.714\text{x}10^{-6}$	Calculated from [2.41]c)
T	Temperature	298 K	(Srinivasan, and Newman, 2004)

From equation [3.18], we can see the dimensionless form of the total concentration, c_T can be written as: $\hat{c}_T = \frac{c_T}{c_0}$.
This results in:

$$\hat{c}_n = \tilde{A}\hat{c}_T e^{\hat{\phi}}, \tag{3.45}$$

$$\hat{c}_p = \tilde{B}\hat{c}_T e^{-\hat{\phi}}, \tag{3.46}$$

$$\hat{c}_s = \tilde{C}\hat{c}_T, \tag{3.47}$$

$$\frac{R_g T\epsilon}{F^2 L^2 c_0}\frac{\partial^2 \hat{\phi}}{\partial \hat{x}^2} = (\hat{c}_n - \hat{c}_p), \tag{3.48}$$

$$\hat{c}_T = \hat{c}_n + \hat{c}_p + \hat{c}_s, \tag{3.49}$$

$$V_n^* \hat{c}_n + V_p^* \hat{c}_p + V_s^* \hat{c}_s = \frac{1}{c_0}. \tag{3.50}$$

At first glance, it might be possible to greatly simplify these equations by assuming that $\hat{c}_T$ is constant throughout the electrolyte. Applying this assumption to the equations [3.45] - [3.47], we find that $\hat{c}_s$ must then also be constant, and we can absorb the c_T terms into the constant terms:

$$\hat{c}_n = \tilde{A}e^{\hat{\phi}}, \tag{3.51}$$
$$\hat{c}_p = \tilde{B}e^{-\hat{\phi}}, \tag{3.52}$$
$$\hat{c}_s = \tilde{C}. \tag{3.53}$$

We again consider the usual boundary conditions for the potential, $\hat{\phi}$ and concentrations, $\hat{c}_n$ and $\hat{c}_p$ in the bulk electrolyte:

$$\hat{\phi}|_{\hat{x}=1} = 0, \tag{3.54}$$
$$\hat{c}_n|_{\hat{x}=1} = 1, \tag{3.55}$$
$$\hat{c}_p|_{\hat{x}=1} = 1. \tag{3.56}$$

We then find $\tilde{A} = \tilde{B} = 1$ and so:

$$\hat{c}_n = e^{\hat{\phi}}, \tag{3.57}$$
$$\hat{c}_p = e^{-\hat{\phi}}. \tag{3.58}$$

Substituting equations [3.57] and [3.58] into Poisson's equation [3.41], where, as in Section 2.2.1, we have set $\lambda = \frac{1}{L}\sqrt{\frac{\epsilon R_g T}{F^2 c_0}}$, we therefore find an equation to solve for just the electric potential, $\hat{\phi}$:

$$\frac{\partial^2 \hat{\phi}}{\partial \hat{x}^2} = \frac{4}{\lambda^2}(e^{\hat{\phi}} - e^{-\hat{\phi}}) = \frac{2}{\lambda^2}\sinh(\hat{\phi}). \tag{3.59}$$

To solve this equation, we first notice that:

$$\frac{\partial}{\partial \hat{x}}\left(\frac{1}{2}\left(\frac{\partial \hat{\phi}}{\partial \hat{x}}\right)^2\right) = \frac{\partial \hat{\phi}}{\partial \hat{x}}\frac{\partial^2 \hat{\phi}}{\partial \hat{x}^2}, \tag{3.60}$$

therefore we can rewrite equation [3.59] as:

$$\frac{\partial}{\partial \hat{x}}\left(\frac{1}{2}\left(\frac{\partial \hat{\phi}}{\partial \hat{x}}\right)^2\right) = \frac{\partial \hat{\phi}}{\partial \hat{x}}\frac{2}{\lambda^2}\sinh(\hat{\phi}). \tag{3.61}$$

Using the fact that:

$$\frac{\partial}{\partial \hat{x}}(\cosh(\hat{\phi})) = \frac{\partial \hat{\phi}}{\partial \hat{x}}\sinh(\hat{\phi}), \tag{3.62}$$

we can then integrate to find:

$$\left(\frac{\partial \hat{\phi}}{\partial \hat{x}}\right)^2 = \frac{4}{\lambda^2}\cosh(\hat{\phi}) + c_1. \tag{3.63}$$

Considering the setup of the model, for the electric potential we have the following boundary conditions:

$$\hat{\phi}|_{\hat{x}\to 1} \to 0, \tag{3.64}$$

$$\left.\frac{\partial \hat{\phi}}{\partial \hat{x}}\right|_{\hat{x}\to 1} \to 0. \tag{3.65}$$

Substituting into equation [3.63], this implies that $c_1 = \frac{-4}{\lambda^2}$ and using the fact that $-1 + \cosh(\hat{\phi}) = 2\sinh^2\left(\frac{\hat{\phi}}{2}\right)$, we can rewrite equation [3.63] as:

$$\frac{\partial \hat{\phi}}{\partial \hat{x}} = \pm\frac{2\sqrt{2}}{\lambda}\sinh\left(\frac{\hat{\phi}}{2}\right), \tag{3.66}$$

which can be solved to give:

$$\tanh(\frac{\hat{\phi}}{4}) = c_2 e^{-\frac{\sqrt{2}}{\lambda}\hat{x}}, \tag{3.67}$$

where we have chosen the negative root to ensure that $\hat{\phi}(\hat{x})$ is purely real as $\hat{x} \to 1$, therefore giving the electric potential as:

$$\hat{\phi}(\hat{x}) = 4\tanh^{-1}(c_2 e^{-\frac{\sqrt{2}}{\lambda}\hat{x}}). \tag{3.68}$$

Note, that taking the positive root for $\hat{\phi}$ would lead to an imaginary electric potential which would cause problems with conservation equations, as the imaginary term describes unstable particles that tend to decay over time (Griffiths, 2006). Quantum mechanics uses imaginary potentials and potential energies to describe wave functions, which we will look at in Chapter 5 when studying the possibility of electron tunnelling occurring on the electrode-electrolyte interface.

Implementing a boundary condition at the electrode surface, we want the potential to be equal to the applied potential, V, and therefore we can find c_2 in terms of $\hat{V}$:

$$\phi|_{x=0} = V \qquad \Longrightarrow \qquad \hat{\phi}|_{\hat{x}=0} = \frac{F}{RT}V = \hat{V}, \tag{3.69}$$

$$\Longrightarrow \quad c_2 = \tanh\left(\frac{\hat{V}}{4}\right) \tag{3.70}$$

Therefore we find the equation for the potential $\hat{\phi}$ as:

$$\hat{\phi}(\hat{x}) = 4\tanh^{-1}\left(\tanh\left(\frac{\hat{V}}{4}\right)e^{-\frac{\sqrt{2}}{\lambda}\hat{x}}\right). \tag{3.71}$$

This solution for $\hat{\phi}$ is plotted against dimensionless distance in Figure 2, showing agreement with the expected profile for the electric potential discussed in Section 5.1.

This form can now be substituted into [3.57] and [3.58] to give concentration profiles for each ion species. These can be seen in Figure 4, where we have compared them to the numerical solution in Section 3.3.2.

3.3.2 Numerical Solution

We will now consider a solution where we assume c_T is not constant; we will assume it has the form $c_T = c_T(x)$. From equation [3.18], we have that the mole fraction of the solvent species is constant, and therefore we have that c_T is proportional to c_s.

Recall the system of dimensionless equations [3.45] - [3.50]:

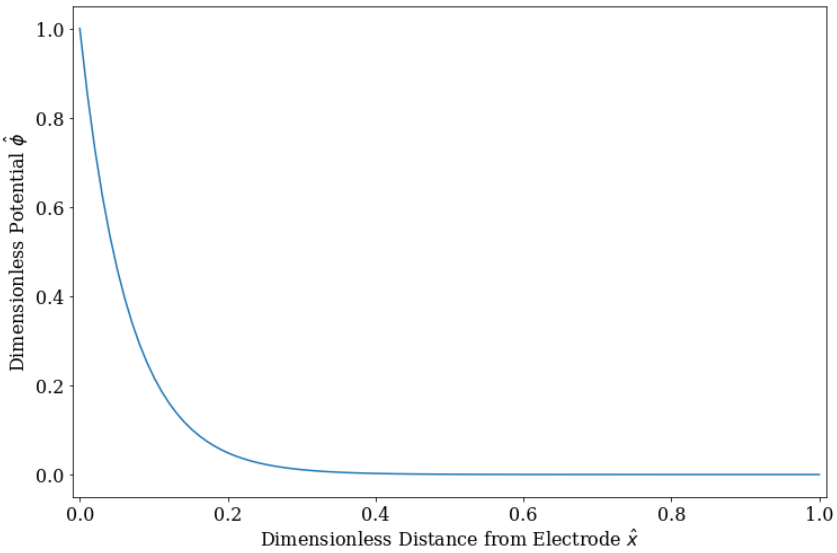

Figure 2: A plot of the analytic solution, equation [3.71], for the dimensionless potential against dimensionless distance from the electrode surface.

$$\hat{c}_n(\hat{x}) = \tilde{A}\hat{c}_T(\hat{x})e^{\hat{\phi}(\hat{x})}, \quad [3.72]$$

$$\hat{c}_p(\hat{x}) = \tilde{B}\hat{c}_T(\hat{x})e^{-\hat{\phi}(\hat{x})}, \quad [3.73]$$

$$\hat{c}_s(\hat{x}) = \tilde{C}\hat{c}_T(\hat{x}), \quad [3.74]$$

$$\frac{\partial^2\hat{\phi}(\hat{x})}{\partial\hat{x}^2} = \frac{1}{\lambda^2}(\hat{c}_n(\hat{x}) - \hat{c}_p(\hat{x})), \quad [3.75]$$

$$\hat{c}_T(\hat{x}) = \hat{c}_n(\hat{x}) + \hat{c}_p(\hat{x}) + \hat{c}_s(\hat{x}), \quad [3.76]$$

$$V_n^*\hat{c}_n(\hat{x}) + V_p^*\hat{c}_p(\hat{x}) + V_s^*\hat{c}_s(\hat{x}) = \frac{1}{c_0}. \quad [3.77]$$

From [3.77], we can see that:

$$\hat{c}_s(\hat{x}) = \frac{1}{V_s^*}\left(\frac{1}{c_0} - V_n^*\hat{c}_n(\hat{x}) - V_p^*\hat{c}_p(\hat{x})\right). \quad [3.78]$$

Combining [3.74] and [3.76] we can also see that:

$$\hat{c}_s(\hat{x}) = \tilde{C}(\hat{c}_n(\hat{x}) + \hat{c}_p(\hat{x}) + \hat{c}_s(\hat{x})), \quad [3.79]$$

which rearranges to give:

$$\hat{c}_s(\hat{x}) = \frac{\tilde{C}(\hat{c}_n(\hat{x}) + \hat{c}_p(\hat{x}))}{(1-\tilde{C})}, \quad [3.80]$$

which can be substituted into [3.72] and [3.73]:

$$\hat{c}_n(\hat{x}) = \tilde{A}\left(\hat{c}_n(\hat{x}) + \hat{c}_p(\hat{x}) + \frac{\tilde{C}[\hat{c}_n(\hat{x}) + \hat{c}_p(\hat{x})]}{(1-\tilde{C})}\right)e^{\hat{\phi}(\hat{x})}, \quad [3.81]$$

$$\hat{c}_p(\hat{x}) = \tilde{B}\left(\hat{c}_n(\hat{x}) + \hat{c}_p(\hat{x}) + \frac{\tilde{C}[\hat{c}_n(\hat{x}) + \hat{c}_p(\hat{x})]}{(1-\tilde{C})}\right)e^{-\hat{\phi}(\hat{x})}. \quad [3.82]$$

As with the analytical solution, we can consider the solution at the far boundary, as $\hat{x}$ reaches the bulk electrolyte, where we have that both concentrations $\hat{c}_n$ and $\hat{c}_n$ tend to the same value of c_0 and the electric potential tends to 0.

$$\hat{c}_n(\hat{x})|_{\hat{x}=1} = 2\tilde{A}c_0\left(\frac{1}{(1-\tilde{C})}\right) = c_0, \quad [3.83]$$

$$\hat{c}_p(\hat{x})|_{\hat{x}=1} = 2\tilde{B}c_0\left(\frac{1}{(1-\tilde{C})}\right) = c_0. \quad [3.84]$$

This implies that:

$$\tilde{A} = \tilde{B} = \frac{1-\tilde{C}}{2}, \quad [3.85]$$

resulting in:

$$\hat{c}_n(\hat{x}) = \frac{1}{2}(\hat{c}_n + \hat{c}_p)e^{\hat{\phi}}, \quad [3.86]$$

$$\hat{c}_p(\hat{x}) = \frac{1}{2}(\hat{c}_n + \hat{c}_p)e^{-\hat{\phi}}. \quad [3.87]$$

Similarly, we can apply the conditions for the concentrations to the $\hat{x} = 0$ boundary, where we assume $\frac{\partial \hat{c}_n}{\partial \hat{x}} = \frac{\partial \hat{c}_p}{\partial \hat{x}} = 0$. Differentiating [3.86] and [3.87] and substituting in for $\hat{c}_T$ and $\hat{c}_s$ using:

$$\left.\frac{\partial \hat{c}_n}{\partial \hat{x}}\right|_{\hat{x}=0} = \frac{1}{2}e^{\hat{\phi}}\left[\frac{\partial \hat{c}_n}{\partial \hat{x}} + \frac{\partial \hat{c}_p}{\partial \hat{x}} + (\hat{c}_n + \hat{c}_p)\frac{\partial \hat{\phi}}{\partial \hat{x}}\right]\Bigg|_{\hat{x}=0} = 0, \quad [3.88]$$

$$\left.\frac{\partial \hat{c}_p}{\partial \hat{x}}\right|_{\hat{x}=0} = \frac{1}{2}e^{-\hat{\phi}}\left[\frac{\partial \hat{c}_n}{\partial \hat{x}} + \frac{\partial \hat{c}_p}{\partial \hat{x}} - (\hat{c}_n + \hat{c}_p)\frac{\partial \hat{\phi}}{\partial \hat{x}}\right]\Bigg|_{\hat{x}=0} = 0, \quad [3.89]$$

and applying the conditions we find:

$$\frac{1}{2}e^{\hat{V}}\left[(\hat{c}_n+\hat{c}_p)\frac{\partial\hat{\phi}}{\partial\hat{x}}\right]\Bigg|_{\hat{x}=0}=0, \tag{3.90}$$

$$-\frac{1}{2}e^{-\hat{V}}\left[(\hat{c}_n+\hat{c}_p)\frac{\partial\hat{\phi}}{\partial\hat{x}}\right]\Bigg|_{\hat{x}=0}=0. \tag{3.91}$$

This leaves us with the condition that

$$\frac{\partial\hat{\phi}}{\partial\hat{x}}\Bigg|_{\hat{x}=0}=0. \tag{3.92}$$

Bringing equations [3.75], [3.86] and [3.87] together along with the boundary conditions, we can summarise the model as:

$$\frac{\partial\hat{\phi}}{\partial\hat{x}} = \hat{\theta}, \tag{3.93}$$

$$\frac{\partial\hat{\theta}}{\partial\hat{x}} = \frac{1}{\lambda^2}(\hat{c}_n-\hat{c}_p), \tag{3.94}$$

$$\hat{c}_n(\hat{x}) = \frac{1}{2}(\hat{c}_n+\hat{c}_p)e^{\hat{\phi}}, \tag{3.95}$$

$$\hat{c}_p(\hat{x}) = \frac{1}{2}(\hat{c}_n+\hat{c}_p)e^{-\hat{\phi}}, \tag{3.96}$$

$$\hat{\phi}|_{\hat{x}=0} = \hat{V}, \quad \hat{\phi}|_{\hat{x}=1}=0, \tag{3.97}$$

$$\frac{\partial\hat{c}_n}{\partial\hat{x}}\Bigg|_{\hat{x}=0} = 0, \quad \hat{c}_n|_{\hat{x}=1}=c_0, \tag{3.98}$$

$$\frac{\partial\hat{c}_p}{\partial\hat{x}}\Bigg|_{\hat{x}=0} = 0, \quad \hat{c}_n|_{\hat{x}=1}=c_0, \tag{3.99}$$

where we have rewritten equation [3.75] as a system of first-order differential equations.

Bringing the equations together, we now note this system of equations is overdetermined and so solving numerically we may be unable to find a solution other than the trivial solution of $c_n = c_p = 0$. We will reduce the number of equations by using equation [3.95] to rewrite c_n in terms of c_p:

$$\hat{c}_n\left[1-\frac{1}{2}e^{\phi}\right]=\frac{1}{2}\hat{c}_p e^{\hat{\phi}}, \tag{3.100}$$

leading to:

$$\hat{c}_n = \frac{1}{2e^{-\hat{\phi}} - 1}\hat{c}_p. \tag{3.101}$$

Substituting this into equation [3.94], we find:

$$\frac{\partial \hat{\theta}}{\partial \hat{x}} = \frac{1}{\lambda^2}\hat{c}_p\left[\frac{1}{2e^{-\hat{\phi}} - 1} - 1\right], \tag{3.102}$$

where we are now only considering the concentration of the positive lithium ions.

Numerical Procedure To solve this numerically, we first considered using the *py-pde* package in Python by following the solving of Poisson's equation in $1D$ (Zwicker, 2020). This package implements a finite difference method and requires a function of the form:

$$\frac{\partial^2 y}{\partial x^2} = F(x). \tag{3.103}$$

Writing equation [3.75] into this form we have:

$$\frac{\partial^2 \phi}{\partial x^2} = F(x) \tag{3.104}$$

$$F(x) = \frac{1}{\lambda^2}(c_n(x) - c_p(x)) \tag{3.105}$$

The spatial domain of $[x_{mix}, x_{max}]$, is uniformly discretised into a grid of intervals, where $N+1$ nodes are placed that determine the boundaries of each interval. This is shown in Figure 3, where the green dots represent the nodes located within the domain, the blue dots represent the nodes placed on either boundary of the domain and the red dots represent the 'ghost' nodes that are generated and approximated in order to implement the Neumann boundary conditions.
To start, we define the grid nodes as:

$$x_i = x_{min} + i\Delta x, \quad \text{for} \quad i = 0, 1, ..., N \tag{3.106}$$

$$\Delta x = \frac{x_{max} - x_{min}}{N} \tag{3.107}$$

and the solution on each node as:

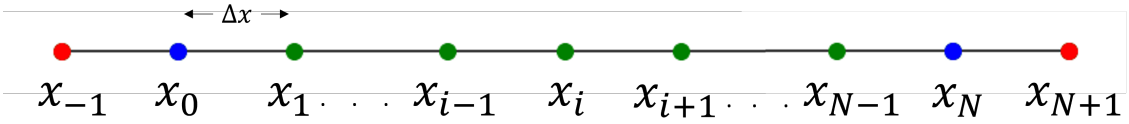

Figure 3: Representing the spatial discretization of the domain for the finite difference method discussed in Section 3.3.2. The green dots represent nodes within the domain, the blue dots represent the nodes on the boundaries of the domain, and the red dots represent the 'ghost' nodes that are used to apply a central difference to the Neumann boundary conditions.

$$\phi_i = \phi(x_i). \tag{3.108}$$

The basis of the finite difference method is approximating the derivatives as finite differences, in this case we use the second order central difference:

$$\phi''(x_i) \approx \frac{\phi_{i-1} + \phi_{i+1} - 2\phi_i}{(\Delta x)^2}. \tag{3.109}$$

In our case $x_{min} = 0, x_{max} = 1$ and therefore the grid becomes:

$$x_i = i\Delta x, \quad \text{for} \quad i = 0, 1, ..., N \tag{3.110}$$

$$\Delta x = \frac{1}{N} \tag{3.111}$$

we also define:

$$F_i(x) = F(x_i) = \frac{1}{\lambda^2}(c_n(x_i) - c_p(x_i)) = \frac{1}{\lambda^2}(c_{n,i} - c_{p,i}) \tag{3.112}$$

Applying the finite difference equation [3.109] to [3.104] and [3.105], we find:

$$\frac{\phi_{i-1} + \phi_{i+1} - 2\phi_i}{(\Delta x)^2} = \frac{1}{\lambda^2}(c_{n,i} - c_{p,i}) \tag{3.113}$$

which can be rearranged to give:

$$\phi_{i-1} + \phi_{i+1} - 2\phi_i = \frac{(\Delta x)^2}{\lambda^2}(c_{n,i} - c_{p,i}). \tag{3.114}$$

We also need to define the boundary conditions on ϕ, c_n and c_p, equations [3.97] and [3.98]-[3.99]b) become:

$$\phi_0 = \hat{V}, \quad \phi_N = 0, \tag{3.115}$$

$$c_{n,N} = c_0, \quad c_{p,N} = c_0. \tag{3.116}$$

We also need the Neumann boundary conditions, which involve applying a first-order finite difference equation. We opted to use a central difference to approximate these boundary conditions as it is typically for accurate than forward or backwards difference. This finite difference is given by:

$$\frac{\partial c_n}{\partial x} \approx \frac{c_{n,i+1} - c_{n,i-1}}{2\Delta x}, \tag{3.117}$$

$$\frac{\partial c_p}{\partial x} \approx \frac{c_{p,i+1} - c_{p,i-1}}{2\Delta x} \tag{3.118}$$

and so the boundary conditions [3.98]-[3.99]a) become:

$$\frac{c_{n,i} - c_{n,-1}}{2\Delta x} = 0, \tag{3.119}$$

$$\frac{c_{p,1} - c_{p,-1}}{2\Delta x} = 0, \tag{3.120}$$

leading to:

$$c_{n,1} = c_{n,-1}, \tag{3.121}$$

$$c_{p,1} = c_{p,-1}. \tag{3.122}$$

where we have introduced the 'ghost' nodes represented by the red dots in Figure 3 but then approximated them to the solution of nodes within the grid.

Using *py-pde* we implemented this scheme with $N = 60$ and a convergence tolerance of 1x10^{-4}. The numerical solution to this system for the concentrations $\hat{c}_n$ and $\hat{c}_p$ is shown in Figure 4, along with the analytical solution from Section 3.3.1.

We note that both solutions very quickly approach 1 as $\hat{x}$ increases towards the bulk electrolyte, implying that the assumption used in Section 3.3.1 of $\hat{c}_T$ (and therefore $\hat{c}_s$) remaining constant is a reasonable assumption in the bulk electrolyte but breaks down as we approach the electrode boundary. It is at this boundary where we approach the double layer (which will be discussed in Chapter 5) and it

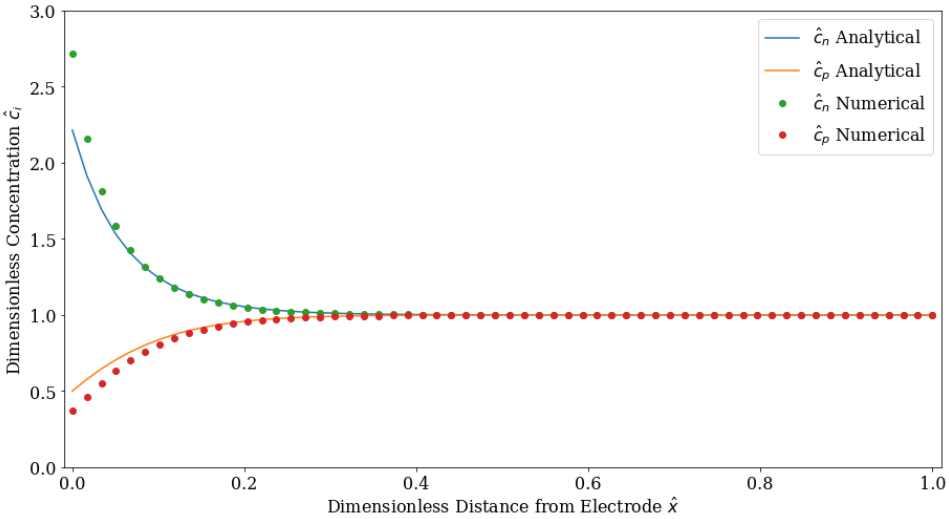

Figure 4: A plot showing the analytical and numerical solutions for the model, as described in Sections 3.3.1 and 3.3.2 respectively. The blue and orange lines show the analytical solutions, while the green and red circles are the numerical solutions for $\hat{c}_n$ and $\hat{c}_p$, respectively.

becomes necessary to consider non-ideal behaviour.

An important consideration is the Python package *py-pde* enforces the restriction that the discretisation must be uniform, meaning Δx must be constant. For the majority of our domain this is not an issue, but close to the electrode surface where the concentrations and electric potential vary more, a non-uniform grid could help to more closely approximate the solution. By increasing the number of nodes in these regions, the scheme can more closely follow a solution.

A way to improve this numerical solution could be to generate our own Python package to allow smaller Δx in regions where the derivatives of the function vary the most. A scheme where Δx is adjusted as the solution proceeds could increase the accuracy and convergence of the solution.

We will now study in more detail what an ideal solution is, why this assumption is made and why it is not a suitable assumption for more concentrated electrolytes.

3.4 Ideal Solutions

When a solution contains more than one type of substance, it is important to consider the energy changes that occur when the substances are first combined. A

solution consisting of a mixture of different substances is considered an ideal solution if there is no change in internal energy on mixing. This can be seen by comparing the Gibbs free energy before and after mixing.

Recall that we can define Gibbs free energy as a sum of enthalpy and the entropy (multiplied by the absolute temperature). We can therefore define the change in Gibbs free energy on mixing as:

$$\Delta G_{mix} = \Delta H_{mix} - T\Delta S_{mix}. \quad [3.123]$$

We will now consider the Gibbs free energy of two substances before and after mixing. Before mixing, we can state their Gibbs free energies using equations [3.3] and [3.15], to give:

$$G_{1,initial} = [\mu_1^0 + RT\ln(\chi_1)]n_1 = \mu_1^0 n_1, \quad [3.124]$$

$$G_{2,initial} = [\mu_2^0 + RT\ln(\chi_2)]n_2 = \mu_2^0 n_2. \quad [3.125]$$

Both substances are in their pure form, so the mole fractions are $\chi_i = 1$, and so the second term in the chemical potential is neglected.

The total Gibbs free energy before mixing is therefore simply the sum of these energies:

$$G_{T,initial} = \mu_1^0 n_1 + \mu_2^0 n_2. \quad [3.126]$$

The two substances are now mixed, again using equations [3.3] and [3.15], we find:

$$G_{1,final} = \mu_1 n_1 = [\mu_1^0 + RT\ln(\chi_1)]n_1, \quad [3.127]$$

$$G_{2,final} = \mu_2 n_2 = [\mu_2^0 + RT\ln(\chi_2)]n_2. \quad [3.128]$$

When [3.127] and [3.128] are added together, we find:

$$G_{T,final} = [\mu_1^0 + RT\ln(\chi_1)]n_1 + [\mu_2^0 + RT\ln(\chi_2)]n_2. \quad [3.129]$$

We would like the change in Gibbs free energy $G_{final} - G_{initial}$, so we can find:

$$\Delta G_{mix} = RT[\ln(\chi_1)n_1 + \ln(\chi_2)n_2]. \quad [3.130]$$

Similarly to equation [3.17], we can use an equation to relate n_i to a total amount of both substances $n_{total} = n_1 + n_2$:

$$\chi_i = \frac{n_i}{n_{total}}, \quad [3.131]$$

which we can substitute in for n_1 and n_2 into equation [3.130] to give:

$$\Delta G_{mix} = n_{total}RT[\chi_1 \ln(\chi_1) + \chi_2 \ln(\chi_2)]. \quad [3.132]$$

Equation [3.132] is known as the Gibbs energy of mixing. For an ideal solution, we can note that the mole fractions of each species will be $0 < \chi_i < 1$, therefore ΔG_{mix} will always be negative, meaning the mixing will occur spontaneously.

Refer back to equation [3.123], we can find (Atkins and De Paula, 2014):

$$\left.\frac{\partial \Delta G_{mix}}{\partial T}\right|_{p,n_i} = -\Delta S_{mix}, \quad [3.133]$$

which we can then combine with equation [3.132] to give:

$$\Delta S_{mix} = -n_{total}R[\chi_1 \ln(\chi_1) + \chi_2 \ln(\chi_2)]. \quad [3.134]$$

Equation [3.134] is known as the entropy of mixing, which we can see will increase as the substances are mixed. As the entropy of a solution is a measure of the disorder of the system, it makes sense that a mixture of two substances would have greater entropy than them separately in their pure forms.

Combining equations [3.123], [3.132], and [3.134] we can conclude that the enthalpy of mixing for a closed system held at a constant temperature, ΔH_{mix}, must be 0. This implies that the net energy to maintain the mixed system is the same as to maintain the separate pure systems. This relates to the energy involved with the interactions between the particles of both substances.

Consider a solution containing particles of two substances, A and B; the possible interactions that can occur are between $A-A$, $B-B$ and $A-B$. In an ideal solution, the average energy of the interactions between different particles must be equal to the average energy of the interactions between similar particles (Atkins and De Paula, 2014). This can be written as:

$$E_{A-A} + E_{B-B} = 2E_{A-B}. \qquad [3.135]$$

In general, for equation [3.135] to hold, A and B must be structurally very similar. Common examples of this include where both substances are hydrocarbons which have similar molecular structures.

Electrolyte solutions are composed of a solute dissolved into a solvent; in general, the substances used for these are unlikely to be structurally similar, leading to non-ideal solutions when mixed. In addition, in an electrolyte solution the solute is dissociated into ions. These ions are charged and so there will be electrostatic interactions between them. These interactions will be much stronger than those with the solvent particles and so equation [3.135] will not hold, suggesting significant deviations from ideality (Wright, 2007).

In Chapter 2, when we considered a dilute electrolyte, we used the assumption of the electrolyte behaving as an ideal solution. In these electrolytes, the concentrations of the ions are low compared to the concentration of the solvent. As it is primarily the interactions between the charged ions that cause the non-ideal behaviour, the effect is lessened as these interactions occur much less frequently, and so it is generally a reasonable assumption to make for the dilute case.

For use in lithium-ion batteries, moderately concentrated electrolytes are of interest, where the ideal solution assumption is not typically valid. In the remainder of this chapter, we will study non-ideal solutions and how we can account for these differences in our models.

3.5 Non-Ideal Solutions and Activity Coefficients

In Chapter 2, we looked at dilute electrolytes, where we assumed the electrolyte behaves as an ideal solution which neglects interactions between the differently

charged ionic species. In a dilute electrolyte this assumption is reasonable. However, at higher concentrations, ions passing close to one another will occur much more frequently making these interactions important to consider.

In Section 3.2, we defined equations for the electrochemical potential in terms of the activity $a_i = \gamma_i \chi_i$ and then took the limit where the activity coefficient $\gamma_i \to 1$ and therefore replaced the activity term with the mole fraction. As discussed in Section 3.3, this is a valid simplification for dilute electrolytes but does not hold for moderately concentrated electrolytes, such as those found in commercial batteries.

Recalling these equations, this time we retain the activity term:

$$\bar{\mu}_i = \mu_i^0 + RT \ln(a_i) + z_i F \phi, \qquad [3.136]$$

where the electrochemical potential for the positive, negative and neutral solvent species is denoted by $\bar{\mu}_i$ where $i = p, n, s$ respectively, μ_i^0 is the chemical potential of the species under standard conditions, z_i is the charge and a_i is the activity.

The activity, a_i, is a measure of the 'effective concentration' of a species when under non-ideal conditions. It is the activity coefficient term γ_i that encompasses the deviation from the ideal behaviour (Atkins and De Paula, 2014).

A common cause for electrolytes to deviate from ideal behaviour is the interactions between the different ion species. As opposite charged ions will tend to be attracted to each other, an individual ion will often be surrounded by ions of the opposite charge which removes the more random nature that ideal solutions tend to follow and reduces the mean distances between ions. This also affects the movements of ions as they will no longer move independently. This is known as the relaxation effect, which becomes more prominent with increased concentrations (Samson et al., 1999).

These interactions cause energy changes on mixing, meaning the enthalpy of mixing ΔH_{mix} is no longer 0. A model to account for these energy changes defines the activity coefficients as functions of the mole fraction of the other ion species. These functions are known as Margules functions.

3.5.1 Margules Functions

In order to account for interactions between ions in an electrolyte, we will now consider a 'regular' solution. This is a solution where we make the assumption that the entropy of mixing ΔS_{mix} is the same as if the solution was an ideal solution, but the enthalpy of mixing ΔH_{mix} is longer assumed to be 0 (Atkins and De Paula, 2014). This enthalpy difference aims to account for the energy changes caused by the ionic interactions, however the restriction placed on the entropy assumes the ions are still distributed randomly as in an ideal solution.

Consider a mixture containing two substances, A and B. We want to derive an expression for the energy changes that occurred during the mixing due to the change in interactions between molecules.

We begin by defining the term coordination number, also known as ligancy, which gives the maximum number of other molecules a given molecule can interact with at any given time. Here, we will denote the average coordination number of the system as C_{num}.

Assuming there are n_A molecules of substance A, we can define the average number of other molecules they will interact with as $n_A C_{num}$. The number of molecules of B that will be interacting with these molecules of A is proportional to the mole fraction of B and is therefore given by $\chi_B n_A C_{num}$.

Before mixing, all of these molecules of A would have been interacting with only other similar molecules, therefore we define the total energy change due to the molecules of A, as:

$$\Delta E_A^{Tot} = \chi_B n_A C_{num}[E_{B-A} - E_{A-A}], \tag{3.137}$$

where, as before, we denote the energy of interactions between two molecules i and j as E_{i-j} where $i, j = A, B$.

Similarly, the total energy change due to the molecules of B is given by:

$$\Delta E_B^{Tot} = \chi_A n_B C_{num}[E_{B-A} - E_{B-B}], \tag{3.138}$$

leading to a total energy change due to interactions as the sum of these contributions, divided by 2 to avoid counting all interactions twice. This can be rearranged to give:

$$\Delta E^{Tot} = \frac{C_{num}}{2}\frac{n_A n_B}{n_A + n_B}\left[2E_{B-A} - \left(E_{A-A} + E_{B-B}\right)\right], \qquad [3.139]$$

where we have replaced each mole fraction term χ_i with $\frac{n_i}{n_A+n_B}$, given by equation [3.131].

Due to the approximation that the entropy of mixing is equal to that of a similar composition ideal solution, and the only change to the Gibbs free energy is coming from the enthalpy of mixing no longer being 0, we can use equation [3.2] to define our change in chemical potential as:

$$\Delta\mu_i = \left.\frac{\partial \Delta E^{Tot}}{\partial n_i}\right|_{T,p,n_j,j\neq i}. \qquad [3.140]$$

Therefore we can find for substance A:

$$\Delta\mu_A = \alpha\left[\frac{n_B}{n_A + n_B} - \frac{n_A n_B}{(n_A + n_B)^2}\right] = \alpha\frac{{n_B}^2}{(n_A + n_B)^2}, \qquad [3.141]$$

where

$$\alpha = \frac{C_{num}}{2}\left[2E_{B-A} - \left(E_{A-A} + E_{B-B}\right)\right]. \qquad [3.142]$$

We can now reintroduce the mole fraction term using equation [3.131] to give:

$$\Delta\mu_A = \alpha{\chi_B}^2, \qquad [3.143]$$

and a similar expression for the change in chemical potential of substance B can be given by:

$$\Delta\mu_B = \alpha{\chi_A}^2. \qquad [3.144]$$

Recall equation [3.15] for the chemical potential, we can substitute the activity for the mole fraction and activity coefficient using equation [3.16] and rewrite to separate the activity coefficient and mole fraction as:

$$\mu_i = \mu_i^0 + RT[\ln(\gamma_i) + \ln(\chi_i)]. \quad [3.145]$$

It is the $RT\ln(\gamma_i)$ term that accounts for the deviation from ideality, so setting this equal to the change in chemical potentials from equations [3.143] and [3.144], we can define the activity coefficients of one substance in terms of the mole fraction of the other substance, such as:

$$\ln(\gamma_A) = \frac{\alpha}{RT}{\chi_B}^2, \quad [3.146]$$

$$\ln(\gamma_B) = \frac{\alpha}{RT}{\chi_A}^2, \quad [3.147]$$

which are known as Margules functions.

Therefore, we can give the altered chemical potentials as:

$$\mu_A = \mu_A^0 + RT\ln(\chi_A) + \alpha{\chi_B}^2, \quad [3.148]$$

$$\mu_B = \mu_B^0 + RT\ln(\chi_B) + \alpha{\chi_A}^2. \quad [3.149]$$

These chemical potentials go some way to describing a non-ideal solution. They include a term to account for the energy due to the ionic interactions between different species; this term depends on the mole fraction of the other species, which in turn depends on its concentration. However, there are still assumptions made for the entropy of mixing which will not always be valid. The entropy is assumed to be the same as if the solution was ideal and therefore indicates a more random distribution of the ions than is likely to be the case.

3.5.2 Maxwell-Stefan Equations

Another proposed way to study the ionic interactions in a solution is to consider the drag forces the different species exert on each other. Here, we introduce the Maxwell-Stefan equations which were applied to multi-component systems by Newman and Thomas-Alyea and are now used as a basis for moderately concentrated diffusion (Newman and Thomas-Alyea, 2004). The equations were originally developed by James Clerk Maxwell, who aimed to model diffusion in binary dilute gases. They were then taken further by Josef Stefan, who studied the application

to multi-component fluids.

These equations aim to account for the interactions between different species by considering the drag forces present when the ions move relative to each other. It is assumed there is a balance between the drag forces acting on the ions due to their relative velocities and the driving force due to the chemical potential gradient. This driving force is therefore given by (Bothe, 2011):

$$\mathbf{d}_i = \chi_i \nabla \mu_i, \tag{3.150}$$

where we are considering positive, negative and neutral solvent species denoted by $i = p, n, s$ respectively.

This driving force must also be equal to the frictional drag force, which depends on the relative velocities of the ions and their mole fractions in the solution. This therefore gives:

$$\mathbf{d}_i = -RT \sum_{j \neq i} f_{ij} \chi_i \chi_j (\mathbf{v}_i - \mathbf{v}_j), \tag{3.151}$$

where f_{ij} is a drag coefficient, together with the mole fractions of each species $RT f_{ij} \chi_i \chi_j$ gives the drag inflicted on species i by species j and $\mathbf{v}_i$ is the velocity of species i.

Setting these forces equal to each other and rearranging leads to:

$$c_i \nabla \mu_i = \sum_{j \neq i} RT f_{ij} c_T \chi_i \chi_j (\mathbf{v}_j - \mathbf{v}_i). \tag{3.152}$$

We now introduce the Maxwell-Stefan diffusivity term D_{ij}, a matrix of diffusivities giving the drag forces between pairs of species:

$$D_{ij} = \frac{1}{f_{ij}}. \tag{3.153}$$

Note that $f_{ij} = f_{ji}$, the drag of species i on another j is equal to the drag j exerts on i; this means that D_{ij} is a symmetric matrix (Verros and Giovannopoulos, 2009).

Substituting equation [3.153] into [3.152] and rewriting the mole fractions in terms of concentrations using equation [3.17], we find:

$$c_i \nabla \mu_i = \sum_{j \neq i} \frac{RT c_i c_j}{c_T D_{ij}} (\mathbf{v}_j - \mathbf{v}_i). \qquad [3.154]$$

Equation [3.154] gives a system of equations known as the Maxwell-Stefan equations for multi-component diffusion (Bothe, 2011). In later sections, we will be using these equations in a model where we aim to study the movements of ions in an electrolyte where we will not assume it behaves as an ideal solution.

3.6 An Ion-Hopping Model

To study the ionic movements in a moderately concentrated electrolyte, we will build a model based on ions hopping on a lattice. We will be treating the electrolyte as a non-ideal solution, so we will be applying the theory behind the Maxwell-Stefan equations and Margules functions.

Consider a single particle on a 1D lattice consisting of N sites. We can start by denoting the site that the particle is currently occupying as site i, and we now want to consider the probabilities of the particle hopping to a different adjacent site.

3.6.1 The Arrhenius Equation

The Arrhenius equation gives the rate of a reaction occurring by considering the energy required for the reaction to occur and the mean kinetic energy of the individual particles involved, which depends on the absolute temperature T of the system as:

$$E^K_{mean} = \frac{3}{2} k_B T, \qquad [3.155]$$

where k_B is the Boltzmann constant.

The ratio of this kinetic energy with the required energy therefore gives a measure of the rate of the reaction, according to the Arrhenius equation, given by:

$$R_k = A \exp\left(\frac{E_a}{k_B T}\right). \qquad [3.156]$$

where R_k is the reaction rate constant, A is a phenomenological constant that depends on the chemical reaction being studied, and E_a is the activation energy, which can be defined as the amount of energy required for the reaction to occur.

In this case, we are considering the amount of energy required for the particle to hop to an adjacent site, namely site j, so we can instead denote this as $E_{i,j}$ the amount of energy required for this particle to hop from site i to site j, where $j = i+1$ or $i-1$.

We are interested in the probabilities of the particle hopping to these adjacent sites, denoted $P_{i,i-1}, P_{i,i+1}$, so we can use the Arrhenius equation to form the following equations:

$$P_{i,i-1} = A \exp\left(\frac{E_{i,i-1}}{k_B T}\right), \quad [3.157]$$

$$P_{i,i+1} = A \exp\left(\frac{E_{i,i+1}}{k_B T}\right). \quad [3.158]$$

3.6.2 Monte Carlo Algorithms

In order to simulate the behaviour of the ions in an electrolyte we will use these probability equations to devise a model that makes use of a Monte Carlo algorithm. These algorithms are a subset of computational methods that use probability distribution theory and random sampling to predict and describe the outcome of an event. In this case, the events we will be studying are the hopping movements of multiple ions, which we will be treating as point charges.

We will be using as a basis a Monte Carlo method known as the Metropolis algorithm (Metropolis et al., 1953). The steps of the algorithm are as follows:

1. The point charges are randomly placed on a lattice, and the energy of the system due to the point charges is calculated, $E_{current}$.

2. A random charge is selected, followed by a direction to move. In 2D, this equates to choosing the x or y direction and positive or negative directions.

3. The charge is assumed to move in this direction and the energy of the new configuration is calculated, E_{new}.

- If this new configuration has a lower energy the change is accepted, $E_{current} = E_{new}$ and the process returns to step 1.
- If the new configuration has a higher energy, the change is accepted with a probability of $P = \exp\left(\frac{E_{current} - E_{new}}{k_B T}\right)$, where this equation is related to the Arrhenius equation by equation [3.158]. If the change is rejected, the configuration reverts to the previous one and $E_{current}$ remains the same. The process then returns to step 1.

These steps are then repeated until the system is in a low-energy state. Note, the change in step 3 is decided by generating a random number between $0 - 1$ and then comparing the calculated probability P to this random number. If P is greater than the generated random number, the configuration change occurs.

3.7 Our Monte Carlo Algorithm

Here, we will lay out how we have implemented the algorithm to study a moderately concentrated electrolyte. We begin by mentioning the assumptions we have made and then describe the simulation procedure.

3.7.1 Assumptions

We will be assuming the electrolyte is a strong electrolyte, meaning the solute will dissociate into ions fully in the solvent. This is instead of a weak electrolyte, which does not fully dissociate therefore both ions and molecules will be present in these solutions. The higher number of ions present will lead to an increase in conductivity, which is a desirable property for lithium-ion batteries (Xu, 2004).

To start with, we will be assuming a $1:1$ binary electrolyte, one that each molecule dissociates into a single positive ion and a single negative ion with valances $z_p = +1, z_n = -1$. Lithium hexafluorophosphate ($LiPF_6$) is a popular choice for use in commercial batteries. It dissociates into Li^+ and PF_6^- ions, and therefore is a binary electrolyte, so this assumption could be valid (Schaefer, 2011). However, the intention is to enable the model to be adaptable to account for other electrolytes.

3.7.2 Initial Iteration of the Algorithm

To start, the ions are placed randomly on the lattice, an example is shown in Figure 5. Next, we need a way to keep track of the electrostatic potential energy of

the system. This energy is caused by the electrostatic (or Coulomb) forces of the ions acting on other nearby ions. For a pair of point charges, Q_1 and Q_2, where $Q_i = ez_i$, z_i is the valance of charge i and e is the elementary charge $\approx 1.602x10^{-19}C$, separated by a distance r, the electrostatic force between them is given by:

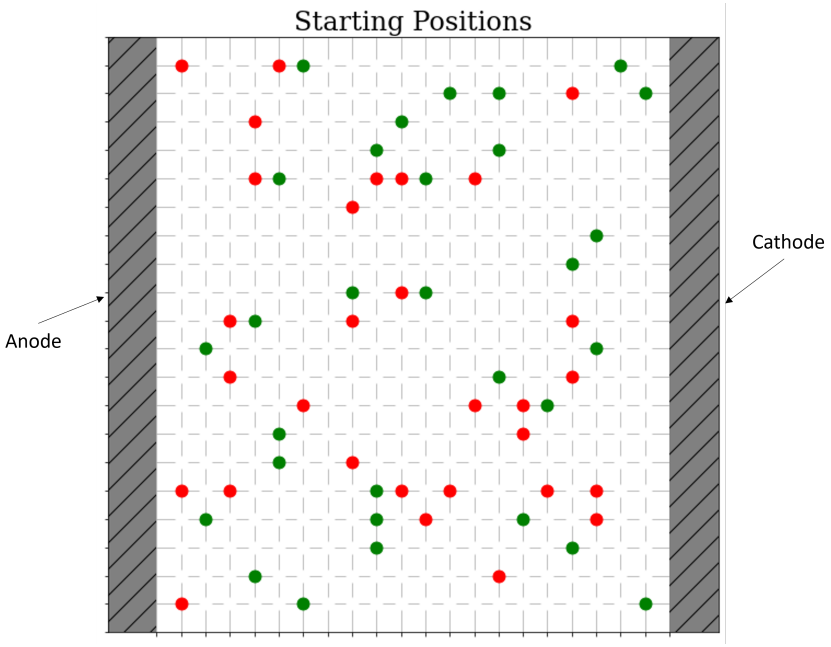

Figure 5: A representation of the initial set-up used for the algorithm, showing a lattice with an electrode either side. The negative ions are shown in red, while the positive ions are in green. A white particle, or a 'hole', represents a solvent molecule. The starting positions are given by all particles being placed randomly on the lattice at the start of the algorithm. This is a 20 x 20 representation of the lattice, for the simulations we used a 100 x 100 lattice.

$$F_c = k_e \frac{Q_1 Q_2}{r^2}, \qquad [3.159]$$

where k_e is known as Coulomb's constant, given by:

$$k_e = \frac{1}{4\pi\epsilon}, \qquad [3.160]$$

where $\epsilon = \epsilon_0 \epsilon_r$ is termed the permittivity of the medium which is given as a multiple of the vacuum permittivity $\epsilon_0 = 8.854\text{x}10^{-12}\ F\ m^{-1}$ and ϵ_r is the relative permittivity.

If the calculated force from equation [3.159] is negative, then the two charges must be of opposite signs and therefore the force between them is attractive, whereas a

positive force implies the charges are of the same sign and the force is repulsive.

The electric potential energy of charge Q_1 while in the presence of Q_2 is therefore given by:

$$V^c = k_e \frac{Q_1 Q_2}{r}. \qquad [3.161]$$

Equation [3.161] can generalised for N charges $Q_i, i = 1, .., N$. Equation [3.162] gives the potential energy of charge i due to all the other charges.

$$V_i^c = k_e Q_i \sum_{j,j \neq i}^{N} \frac{Q_j}{r_{ij}}, \qquad [3.162]$$

where r_{ij} is the distance between charges i and j.

Finally, this can expanded to give the electrostatic potential energy of the whole system of charges:

$$V_{Total}^c = \frac{1}{2} k_e \sum_{i}^{N} Q_i \sum_{j,j \neq i}^{N} \frac{Q_j}{r_{ij}}, \qquad [3.163]$$

where we include the factor of $\frac{1}{2}$ to avoid counting the contribution from each charge twice.

We will be using equation [3.163] to calculate the electrostatic potential energy of the system of ions on the lattice.

Note that in general, Coulomb's law only applies to stationary point charges. This is due to the movement of charge causing a magnetic field to be induced and therefore leading to a difference in the force that the charge experiences. To take this into account, the Biot-Savart law and Lorentz forces can be studied. However, in this case we are calculating the Coulomb forces in between each hopping movement, so at this time we are assuming the charges are instantaneous at rest.

The simulation begins with a calculation of the energy of the initial configuration, where we set an initial temperature. We then follow the steps set out in Section

4.5.2 to bring the system to a low-energy state. This is done by introducing a temperature-reducing constant T_c and a set number of steps N_T, where $0 < T_c < 1$, and slowly reducing the temperature by a factor of T_c every N_T steps (Kirkpatrick et al., 1983). This step aims to simulate the initial mixing of the solute into the solvent, with the electrostatic potential energy relating to the enthalpy of mixing discussed in Section 4.4.

We took the initial temperature to be $T_{initial} = 298K$ and the temperature-reducing constant $T_c = 0.95$. The simulation was run for $10,000$ steps, and the number of steps between temperature changes was $N_T = 500$.

Now the system is in a low-energy state, we can now proceed with the simulation of the electrolyte while there is a electric potential applied between the two electrodes.

3.7.3 Introducing Margles Functions

We are interested in using this simulation to study the behaviour of the ions in more concentrated electrolytes; specifically we can consider the activity coefficient of the electrolyte and study how this varies with changing electrolyte concentration. Here, we consider a specific electrolyte example and introduce Margules functions to quantify the activity coefficients. We then compare our simulation results to experimental results found in (Stewart and Newman, 2008).

Consider a binary $1:1$ electrolyte with solute Lithium hexafluorophosphate ($LiPF_6$), which dissociates into Li^+ and PF_6^- ions in a carbonate solvent. Here, we initially looked at ethylene carbonate (EC, chemical formula: $CO(CH_2O)_2$), diethyl carbonate (DC, chemical formula: $CO(C_2H_5O)_2$) and ethyl methyl carbonate (EMC, chemical formula: $CO(C_3H_8O_2)$). The first set of results for these solvents motivated us to also look at a solvent made up of a combination of EC and EMC.

We can rewrite equations [3.146] and [3.147] as:

$$\ln(\gamma_{Li^+}) = \frac{\alpha}{RT}{\chi_{PF_6^-}}^2, \qquad [3.164]$$

$$\ln(\gamma_{PF_6^-}) = \frac{\alpha}{RT}{\chi_{Li^+}}^2, \qquad [3.165]$$

where we have also rewritten equation [3.142]:

$$\alpha = \frac{C_{num}}{2}\left[2E_{PF_6^- - Li^+} - \left(E_{Li^+ - Li^+} + E_{PF_6^- - PF_6^-}\right)\right]. \quad [3.166]$$

Recall the altered forms of the chemical potentials using Margules functions, equations [3.148], [3.149] and writing them using the Li^+ and PF_6^- ions:

$$\mu_{Li^+} = \mu^0_{Li^+} + RT\ln(\chi_{Li^+}) + \alpha{\chi_{PF_6^-}}^2, \quad [3.167]$$
$$\mu_{PF_6^-} = \mu^0_{PF_6^-} + RT\ln(\chi_{PF_6^-}) + \alpha{\chi_{Li^+}}^2, \quad [3.168]$$

and the equation for electrochemical potential [3.14]:

$$\bar{\mu}_i = \mu_i + z_i F\phi. \quad [3.169]$$

These can be combined for the electrochemical potentials for each species:

$$\bar{\mu}_{Li^+} = \mu^0_{Li^+} + RT\ln(\chi_{Li^+}) + \alpha{\chi_{PF_6^-}}^2 + F\phi \quad [3.170]$$
$$\bar{\mu}_{PF_6^-} = \mu^0_{PF_6^-} + RT\ln(\chi_{PF_6^-}) + \alpha{\chi_{Li^+}}^2 - F\phi, \quad [3.171]$$

where we have set $z_n = -1$ and $z_p = +1$.

3.7.4 Simulation Procedure

During the simulation, we kept track of both the total electrostatic energy of the system of point charges, using equation [3.163] and the electrochemical potential of each charged species using equations [3.170] and [3.171], where the value for α was calculated using equation [3.166].

We now used the electrochemical potentials to guide the simulation, with the calculated electrostatic energies having an impact if the change in electrostatic energy is large enough in comparison to the change in electrochemical potentials. At each step, the following algorithm occurred:

1. The electrochemical potential of the positive and negative species is calculated and the electrostatic energy of the system due to the point charges is calculated, $E_{current}$.

2. A random charge is selected, followed by a direction to move. In 2D, this equates to choosing the x or y direction and positive or negative directions.

3. The charge is assumed to move in this direction and the new electrochemical potentials are calculated along with the electrostatic energy of the new configuration, E_{new}.

    - If the charge follows the direction of the electrochemical potential (if $\Delta\hat{\mu}_i < 0$), the electrostatic energy is now compared:
        - If the new configuration has a lower electrostatic energy ($E_{new} < E_{current}$) then new configuration is accepted $E_{current} = E_{new}$ and the process returns to step 1.
        - If the new configuration has a higher electrostatic energy ($E_{new} > E_{current}$), the change is accepted with a probability of $P = \exp\left(\frac{E_{current} - E_{new} + |\Delta\bar{\mu}_i|}{k_B T}\right)$, where this equation is related to the Arrhenius equation by equation [3.158]. If the change is rejected, the configuration reverts to the previous one and $E_{current}$ remains the same. The process then returns to step 1.
    - If the charge is seen as 'going against' the electrochemical potential (if $\Delta\bar{\mu}_i > 0$) the electrostatic energy is again compared. The change is accepted with a probability of $P = \exp\left(\frac{E_{current} - E_{new} - |\Delta\bar{\mu}_i|}{k_B T}\right)$. If the change is rejected, the configuration reverts to the previous one and $E_{current}$ remains the same. The process then returns to step 1.

To summarise, by including the change in electrochemical potential in the probabilities, the following occurs:
- If the configuration change follows the direction expected from the electrochemical potential, the probability of the change happening is increased. If the electrostatic energy also decreases this change is guaranteed.
- While the configuration not following the electrochemical potential doesn't immediately mean the change doesn't occur, the probability of it occurring is decreased. A decrease in electrostatic energy no longer guarantees the change.

This keeps the random nature of the Monte Carlo simulation while incorporating the effects of the electric potential and the interactions between the charged ions.

We repeated the simulation for different values of the mole fraction (X_{Li^+}) between $0.01 - 0.1$. Using a lattice size of 100 x 100, Table 3 shows the values for mole fractions used and how this translates into the number of positive and negative ions included in each simulation.

The typical coordination number of the lithium ions in ($LiPF_6$) ranges from $3 - 6$ (Malliakas et al., 2016), with numbers closer to 4 appearing more frequently in the literature (Yuan et al., 2014)(Kameda et al., 2016). We have completed the simulation calculations for $C_{num} = 3, 4, 5, 6$ for each solvent.

Table 3: The mole fraction values used in the simulation and the number of positive and negative ions and solvent molecules used to represent these mole fractions.

χ_{LiFP_6}	No. of Li^+ ions	No. of FP_6^- ions	No. of solvent molecules
0.01	50	50	9900
0.02	100	100	9800
0.03	150	150	9700
0.04	200	200	9600
0.05	250	250	9500
0.06	300	300	9400
0.07	350	350	9300
0.08	400	400	9200
0.09	450	450	9100
0.1	500	500	9000

In order to compare our results to the experimental results in the literature, we will be converting these mole fractions into molalities.

We have previously defined mole fraction in terms of concentrations, as:

$$\chi_{LiPF_6} = \frac{c_{LiPF_6}}{c_T}, \qquad \chi_S = \frac{c_s}{c_T}, \tag{3.172}$$

where s = solvent.

This can be rewritten in terms of the number of moles of solute and solvent:

$$\chi_{LiPF_6} = \frac{n_{LiPF_6}}{n_{LiPF_6} + n_s}, \qquad \chi_S = \frac{n_s}{n_{LiPF_6} + n_s}. \tag{3.173}$$

Dividing [3.173] a) by [3.173] b) leads to:

$$\frac{\chi_{LiPF_6}}{\chi_s} = \frac{n_{LiPF_6}}{n_s}. \tag{3.174}$$

The number of moles in a substance is given by the mass of the substance (m_i) divided by the substance's molecular mass (M_i^{mol}):

$$n_i = \frac{m_i}{M_i^{mol}}, \tag{3.175}$$

therefore substituting this for each substance into equation [3.174] we find:

$$\frac{\chi_{LiPF_6}}{\chi_s} = \frac{m_{LiPF_6}/M_{LiPF_6}^{mol}}{m_s/M_s^{mol}} = \frac{m_{LiPF_6} M_s^{mol}}{m_s M_{LiPF_6}^{mol}}. \tag{3.176}$$

which can be rearranged to give:

$$\frac{\chi_{LiPF_6}}{\chi_s M_s^{mol}} = \frac{m_{LiPF_6}}{m_s M_{LiPF_6}^{mol}}. \tag{3.177}$$

Molalities describe the amount of a solute (in moles) per $1kg$ of solvent, so can be written as:

$$\text{Molality} = \frac{n_{LiPF_6}}{m_s/1000}. \tag{3.178}$$

We can rearrange and substitute in the number of moles of solute using equation [3.175] to give:

$$\text{Molality} = \frac{1000 m_{LiPF_6}}{m_s M_{LiPF_6}^{mol}}. \tag{3.179}$$

This is similar to the RHS of equation [3.177], therefore we can substitute it in to give the molality in terms of mole fractions:

$$\text{Molality} = \frac{1000 \chi_{LiPF_6}}{\chi_s M_s^{mol}}. \tag{3.180}$$

Finally, we know the sum of all mole fractions must total 1, therefore we have $\chi_s = 1 - \chi_{LiPF_6}$ and we can then define the molality in terms of just the mole fraction of the solute χ_{LiPF_6} and the molecular mass of the solvent M_s^{mol}:

$$\text{Molality} = \frac{1000\chi_{LiPF_6}}{(1-\chi_{LiPF_6})M_s^{mol}}. \quad [3.181]$$

We now require the molecular mass of each solvent; these are shown in Table 4. In (Stewart and Newman, 2008), they used a solvent made up of a 1 : 1 (by mas) mix of EC and EMC. Using their respective molecular masses, we can conclude the mix was 54.174% EC and 45.826% EMC, therefore giving a molecular mass of $95.413 gmol^{-1}$.

Table 4: The solvents used in the simulation and their molecular masses, listed in $g\ mol^{-1}$.

Solvent	Molecular mass, M_i^{mol} $(g\ mol^{-1})$
Ethylene carbonate	88.062
Diethyl carbonate	118.13
Ethyl methyl carbonate	104.10
EC:EMC mix	95.413

We can now use equation [3.181] to convert the mole fractions in table 3 into molalities for each type of solvent. These molalities are found in Table 5.

Table 5: The mole fractions used in the simulation and their conversions into molality for each solvent used.

χ_{LiFP_6}	Molality EC	Molality DC	Molality EMC	Molality EC:EMC mix
0.01	0.1147	0.08551	0.09703	0.1059
0.02	0.2317	0.1723	0.1960	0.2139
0.03	0.3512	0.2618	0.2971	0.3241
0.04	0.4732	0.3527	0.4002	0.4367
0.05	0.5977	0.4455	0.5056	0.5516
0.06	0.7248	0.5403	0.6131	0.6690
0.07	0.8547	0.6372	0.7230	0.7889
0.08	0.9874	0.7361	0.8353	0.9114
0.09	1.123	0.8372	0.9500	1.037
0.1	1.261	0.9406	1.067	1.165

3.8 Results and Discussion

The algorithm described above was run for $10,000$ steps for each mole fraction using the numbers of charged ions and solvent molecules as shown in Table 3. The simulation produced values for α, then using equation [3.164] we calculated the values for the activity coefficient $ln(\gamma_{Li^+})$.

Note that equation [3.164] includes a term multiplying by the mole fraction of the PF_6^- ions. As the electrolyte is a binary 1:1 electrolyte, we have an equal number of positive and negative ions, meaning we also have an equal number of moles of each. This dictates that the mole fractions of the individual ions species are simply half of the mole fraction of the combined species.

Specifically, [3.164] can be written as:

$$\ln(\gamma_{Li^+}) = \frac{\alpha}{RT}\frac{1}{2}{\chi_{LiPF_6}}^2. \qquad [3.182]$$

Using the conversions in Table 5, we were then able to plot the activity coefficient against molality for each solvent, as shown in Figure 6. The dotted line in the plots represents the experimental results from the literature (Stewart and Newman, 2008). Table 6 shows the parameters used in the simulation.

Table 6: Values and descriptions of parameters introduced in the simulation, including those first used in the second and third iterations of the algorithm.

Parameter	Description	Value	Reference
C_{num}	Coordination number of Li^+ ions	$3, 4, 5, 6$	(Malliakas et al., 2016)
δ_{part}	Partial charge assigned to solvent molecules	± 0.2	(Vigil et al., 2023)
δ_r	Reducing factor for charged ions	0.8	(Vigil et al., 2023)
ϵ	Permittivity of electrolyte	$80\epsilon_0 = 7.0834\text{x}10^{-10}\ F\ m^{-1}$	(Richardson and King, 2007)
N_T	Number of steps between temperature changes	500	(Kirkpatrick et al., 1983)
$\phi(x)$	Electric potential	Equation from ref	(Richardson et al., 2021)
T_c	Temperature reducing constant	0.95	(Kirkpatrick et al., 1983)
$T_{initial}$	Initial temperature	$298\ K$	(Richardson et al., 2021)
z_n	Valency of Lithium ion	1	(Richardson et al., 2021)
z_p	Valency of negative counter-ion	-1	(Richardson et al., 2021)

3.8.1 Results for First Iteration of Algorithm

The results for ethylene carbonate in Figure 6a) show some agreement for molalities $< 1\ mol\ kg^{-1}$, with the results following the same general shape as the curve from the experimental results. They tend to predict slightly lower values for the activity coefficient but then diverge off to much higher values for molalities $> 1\ mol\ kg^{-1}$. The diethyl carbonate solvent showed a similar trend but overall tended to have higher activity coefficients.

The solvents ethylene carbonate and ethyl methyl carbonate showed results closest to the experimental results, so we opted to also run the simulation for a solvent composed of a mixture of these two substances. It is common for electrolytes in commercial lithium-ion batteries to use a mixture of substances as the solvent as this can allow the electrochemical properties of the electrolyte to be optimised, so we felt this a reasonable addition solvent to try. We considered the mixed solvent of EC and EMC that was used in (Stewart and Newman, 2008).

We found the results for this mixed solvent, shown in Figure 6d), were slightly closer to the experimental results curve but were again still diverging significantly to much higher values at higher molalities.

For all solvents, the higher values of coordination number showed much more significant divergence to higher activity coefficients. This is to be expected as a higher coordination number allows a given charged ion to have more closest neighbour ions and therefore there are more close-range ionic interactions occurring. These interactions lead to a deviation from ideality by decreasing the mobility of the ions, so one would expect higher coordination numbers to show more deviation and therefore higher activity coefficients.

Up to this point, we have primarily focused on the interactions between the positive and negative ions. It is important to consider that solvent molecules, despite having no charge, can still have an effect on the charged ions. This is caused by the polarity of the solvent molecules; a solvent with a higher polarity has partial charges on different sides of the molecule, causing a slight charge imbalance and therefore causing a response in the presence of charged ions.

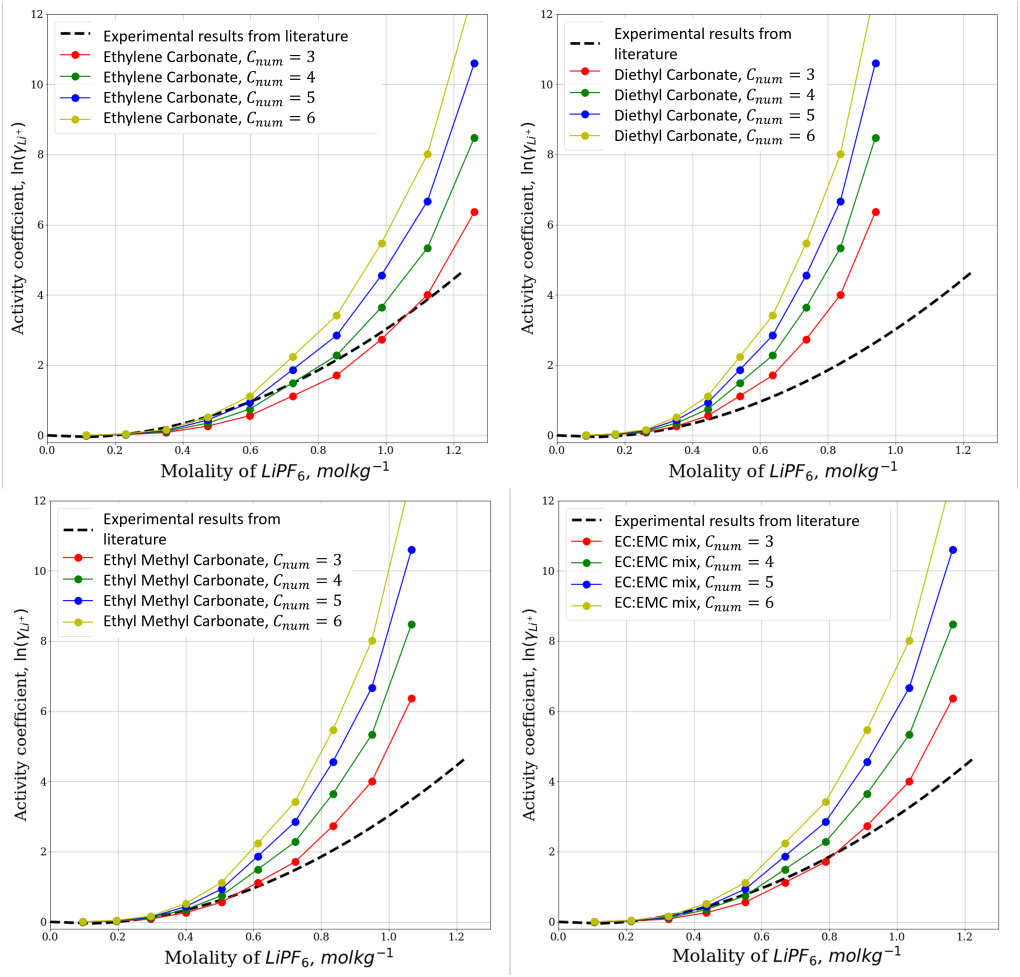

Figure 6: Plots of activity coefficient $ln(\gamma_{Li^+})$ as a function of molality for different coordination numbers and solvents. For each plot, the dotted line shows the curve fit to experimental data from (Stewart and Newman, 2008) for comparison. a) Shows the results for an ethylene carbonate solvent, b) shows the results for a diethyl carbonate solvent, c) shows the results for an ethyl methyl carbonate solvent, d) shows the results for a solvent made up of a mixed EC:EMC solvent. These results come from the initial iteration of the algorithm discussed in Sections 3.6 and 3.7.

When the solute dissociates into the solvent, the ions become fully surrounded by the solvent molecules, which orientate themselves so the direction of the dipole moment is opposite to the charge of the ion. This is, solvent molecules surrounding a positive ion will align themselves so the part of the molecule with a slight negative partial charge is facing inwards towards the positive ion. This occurrence is known as the formation of a solvation shell and can have an effect on the mobility of the ions in the solution.

In order to study this effect, we opted to make changes to the algorithm to account for these solvation shells. Of the solvents we have opted to study, ethylene carbonate has a very high polarity, while diethyl carbonate and ethyl methyl carbonate have much lower polarities.

3.8.2 Results for Second Iteration of Algorithm

The first method to account for the solvation shells involved modifying the ion-hopping probabilities. The aim was to do this by introducing an additional step in the algorithm when calculating the energy changes. If, as represented in Figure 7a), the algorithm has selected a charged ion (in this case a negative ion) to swap places with a solvent molecule (highlighted in grey) which is immediately adjacent to another charged ion (the above positive ion) we wish to consider the energy changes.

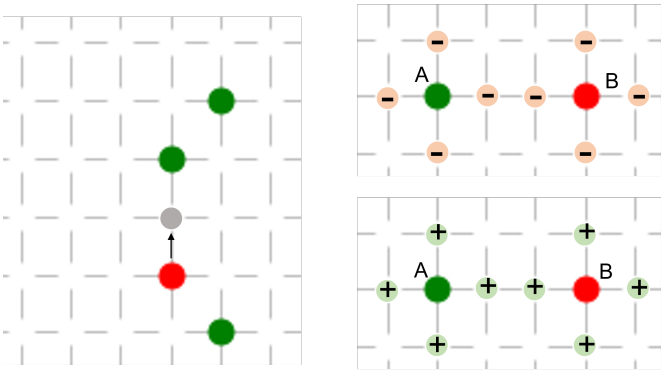

Figure 7: A representation of the methods used to account for solvation shells. a) Shows a negative ion (in red) swapping places with a solvent molecule that is already adjacent to a charged ion. This solvent molecule is part of a solvation shell surrounding the positive ion. b) Shows how we implemented the dipole moment in the solvent molecules. When calculating the energy of an ion due to the presence of a polar solvent molecule, b) shows how we assign the charges when considering ion A, c) shows how we assign the charges when considering ion B.

Initially, only the charged ions would contribute to the energy, but solvent molecules involved in a solvation shell could be seen as 'shielding' the central charged ion and lessening its contribution to the energy. This is known as the formation of partial charges (Jämbeck et al., 2012). The effect of this is a reduction in the calculated 'current energy'. For moves where the energy change is negative by a large margin, this will not have an impact. However, for moves where the energy change is negative but very small in magnitude, this could potentially cause the change to not occur. Finally, if the energy change is positive, the energy change will appear slightly larger in magnitude and therefore will be slightly less likely to occur.

The additional step in the algorithm occurs once the charge is selected but before the move takes place (between steps 2 and 3), and is as follows:

The position the charge is being moved into is checked, if this position currently has a solvent molecule then the positions adjacent to that solvent molecule are also checked. If this solvent molecule is not currently adjacent to another charged ion (other than the one being moved) then the simulation proceeds as normal. However, if the solvent molecule is currently adjacent to another charged ion the following occurs:

- The magnitude of charge of the adjacent charged ion is multiplied by a reducing factor of δ_r so that $Q_{i,new} = \delta_r Q_i$
- The energy change with this reduced magnitude of charge is calculated and input into the probabilities which dictates whether the change goes ahead as previously.
- The reducing factor δ_r is removed and the charge of the ion goes back to ± 1.

In the literature, a Monte Carlo simulation was used to calculate electrolyte transference numbers, which gives a measure of the proportion of the current that is carried by a charged ion. They opted to account for the solvation of lithium ions in a polar solvent by scaling the charges of the lithium ions (and the negative counterions) to values between $0.78 - 1$. The results showed good agreement with previous calculations of transference numbers, with the suggestion of a number ~ 0.8 being the optimal value (Leontyeva and Stuchebrukhov, 2011)(Vigil et al., 2023). We therefore chose to use $\delta_r = 0.8$ in this iteration of the algorithm.

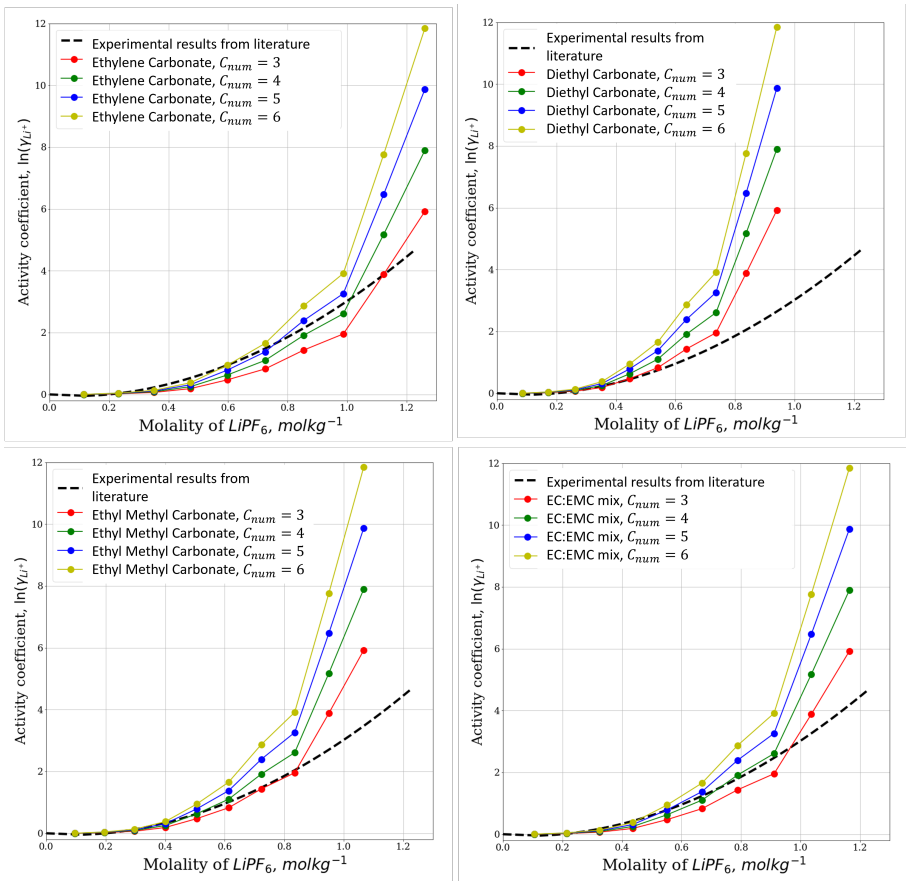

Figure 8: Plots of activity coefficient $ln(\gamma_{Li^+})$ as a function of molality for different coordination numbers and solvents. For each plot the dotted line shows the curve fit to experimental data from (Stewart and Newman, 2008) for comparison. a) Shows the results for an ethylene carbonate solvent, b) shows the results for a diethyl carbonate solvent, c) shows the results for an ethyl methyl carbonate solvent, d) shows the results for a solvent made up of a mixed EC:EMC solvent. These results come from the second iteration of the algorithm originally discussed Sections in 3.6, 3.7., with the changes in Section 3.8.2 included.

The results of the algorithm with this change are shown in Figure 8. The plots overall show a similar shape to the first iteration's results but do predict slightly lower activity coefficients, with lower coordination numbers dropping quite far below the experimental results curve. The high molalities have again diverged to much higher activity coefficient values; this time the activity coefficients are not quite as high but the divergence away from the other results is steeper.

3.8.3 Results for Final Iteration of Algorithm

The results did not quite follow the trend we were hoping to see, so we opted to make additional changes to account for the solvation shells. To represent the dipole

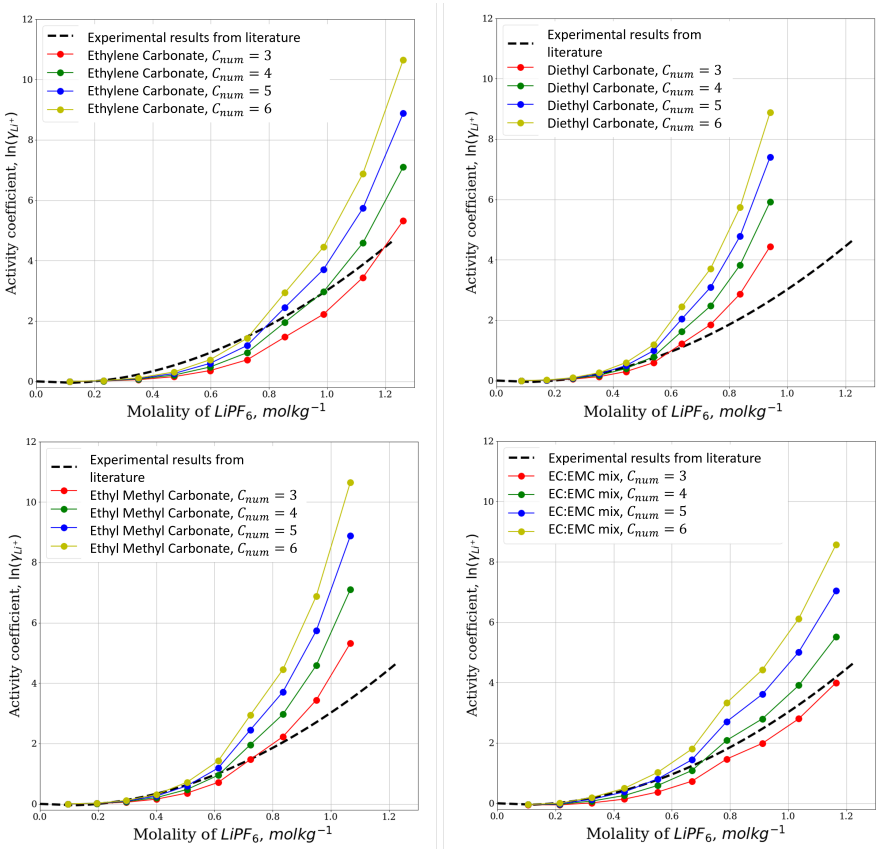

Figure 9: Plots of activity coefficient $ln(\gamma_{Li^+})$ as a function of molality for different coordination numbers and solvents. For each plot, the dotted line shows the curve fit to experimental data from (Stewart and Newman, 2008) for comparison. a) Shows the results for an ethylene carbonate solvent, b) shows the results for a diethyl carbonate solvent, c) shows the results for an ethyl methyl carbonate solvent, d) shows the results for a solvent made up of a mixed EC:EMC solvent. These results come from the third iteration of the algorithm originally discussed in Sections 3.6 and 3.7., with the changes in Section 3.8.3 included.

moment of the solvent molecules, we will alter the energy calculations to consider the solvent molecule particles, that are adjacent to a charged ion, to have a slight 'charge' depending on which the charge of the ion they are adjacent to.

When calculating the energy in a system of charges we can consider the energy of a given particle A due to another particle B (E_{A-B}), or the energy of particle B due to particle A (E_{B-A}). So far, we have assumed these values are equal.

Instead, when considering the energy from particle A's (a positive ion) point of view, we will let the solvent molecules nearby have a slight opposite charge, while the solvent molecules adjacent to other ions (say particle B) will have a slight charge of the same sign as the particle they are surrounding. This is to represent the polar solvent molecules aligning themselves so the opposite charge is close to the surrounding ion and the like charge is facing outwards towards the rest of the lattice. This is shown in Figure 7b) when considering particle A and in Figure 7c) when considering particle B.

This was implemented into the energy calculation parts of the algorithm (in addition to the steps implemented in Section 3.8.2). The energy of the current configuration is calculated using Coulomb's Law, equation [3.163] as previously. However, while calculating the pairwise interactions the solvent molecules will be assigned a partial charge ($\pm\delta_{part}$) depending on the charge of the ion they are adjacent to. Calculating the energy of the pairwise interaction for some ions C_i is as follows:

- The solvent molecules adjacent to C_i are assigned partial charges, δ_{part}, of the opposite charge to C_i.
- The solvent molecules adjacent to all other ions are assigned partial charges, δ_{part}, of the same charge as the ion they are adjacent to. This is done additively, so if a solvent molecule is adjacent to two ions of opposite charge, it remains as having no partial charge ($+\delta_{part} - \delta_{part} = 0$). Conversely, if adjacent to two ions of the same charge it will be assigned a partial charge of $\pm 2\delta_{part}$.
- Use Coulombs Law to calculate the electrostatic energy between ion C_i and all charged ions and partially charged molecules.

This is repeated for all charged ions, and each time the solvent molecules are assigned new partial charges depending on the charges of the ions being considered. The overall implication of this change to the algorithm is a further reduction in the energies being considered, especially at higher concentrations.

We opted to continue to use the fact that the partial charges of the lithium ions become ~ 0.8 when solvated and therefore to balance this we chose the solvent partial charges $\delta_{part} = 0.2$. This represents a slight dipole moment forming without the solvent molecules becoming too charged.

The results of the algorithm with these changes are shown in Figure 9.

We can see that low molalities still follow the experimental curve quite well, with these results following the curve slightly better, especially the lower coordination numbers for the mixed EC:EMC solvent. This suggests that the alterations we made to the algorithm go some way towards accounting for these solvation shells and the interactions they cause with the charged ions. The results also imply, in agreement with the literature, that lithium ions in this form will typically have coordination numbers closer to $3 - 4$.

3.9 Summary

In this chapter, we have studied moderately concentrated electrolytes. These electrolytes are closer to those used in commercial batteries, but their study requires refining previous assumptions to account for the high concentrations. We began by introducing electrochemical potentials and the concept of activity. We summarised a model using these electrochemical potentials and found analytical and numerical solutions.

We then discussed the differences between ideal and non-ideal solutions. In dilute electrolytes, the activity term can be replaced with the mole fraction as they tend to act like an ideal solution. However, concentrated electrolytes deviate from this ideality, so this assumption can no longer hold. This deviation is measured by the activity coefficient. We introduced Margles functions and the Maxwell-Stefan equations, which are popular ways to account for non-ideal behaviour.

We set up a Monte Carlo simulation based on ions hopping on a lattice, which would study the ionic interactions in an electrolyte to approximate their activity coefficients. We studied an electrolyte composed of lithium hexafluorophosphate and different solvent choices and compared the results to experimental results from the literature. We found the simulation gave reasonable agreement for low molalities but tended to deviate to much higher values for molalities $> 1\ mol\ kg^{-1}$.

These results motivated altering the algorithm to account for ion-solvent interactions due to the polarity of the solvents we studied. We ran the results for two further iterations of the algorithm, and each time the results improved slightly. The results for the final algorithm for the mixed solvent (composed of ethylene carbonate and ethyl methyl carbonate) showed reasonable agreement across the molality range tested when using lower coordination numbers.

3.9.1 Further work

The simulation could be extended to account for non-binary electrolytes, where the solute may dissociate into various ions of different charges, as well as testing more mixed solvent combinations. The Maxwell-Stefan equations could be incorporated into the simulation. This will introduce the drag force between different ions. However, this drag force depends on the relative velocities of the ions involved; therefore, as discussed above, Coulomb's law may no longer be valid, and an alternative method to calculate the energy may be needed.

The Debye-Hückel theory describes the deviation from ideality using a continuous model to study electrostatic potential energy from such interactions. The model shows agreement with experiments for lower concentrations, so it could provide insight on how to proceed with refining the algorithm for higher concentrations.

For the simulation in this section, we restricted our focus to a 2D model. Comparing this to 3D, it is typical to assume symmetry along the height of an electrochemical cell and so a 2D cross-section can suitably model the situation while significantly reducing computing complexity. We chose to simulate the ionic movements on a cross-section of a 3D cell; we expect the ionic movements due to the electric field to be well represented as the electric potential between the two electrodes will be consistent in the (y, z) directions (assuming the chemistry of electrode materials

are consistent) and therefore the ions will only be effected based on their distance from the electrodes (in the x direction). The ionic movements due to ion-ion and ion-solvent interactions are where a 3D model could change significantly as such interactions could have an effect in all directions. Extending the geometry of our simulation to 3D would increase the number of hopping directions to choose from to 6, which wouldn't increase complexity by much. However, a 3D geometry would significantly increase the number of hopping sites and therefore also the number of ions present if we were to study the same concentrations.

Similarly, due to limitations with computational power, we had to restrict the size of our lattice to a 100x100 grid, comparing this to reality it is significantly less ion sites. The average nearest-neighbour distance of a Li^+ ion is $\sim$ 2.1x10^{-10} m (Marcus, 1988) and a typical distance between electrodes is 2x10^{-5} m (Ecker et al., 2015) leading to approximately $\sim$ 1x10^5 ions fitting between the electrodes. In addition, the ionic radius of the negative counter ions and solvent molecules would differ. A PF_6^- ion has an ionic radius of 2.42x10^{-10} m (Simoes, 2017) and so $\sim$ 4x10^4 would fit between the electrodes, with the solvent molecules being bigger still. This great variance in sizes makes it difficult to quantify how close different ions can get to each other and therefore how many ion sites would be most accurate. We opted for a 100x100 grid with fixed site sizes to keep the computational times reasonable but still have a representative sample.

Despite restricting the geometry to 2D and considering a smaller number of ions, our simulation showed results that followed the same general shape as those found in the literature. The results for low concentrations showed very good agreement while higher concentrations tended to deviate, although each time we refined the algorithm our results improved. This is to be expected, as higher concentrations require more ions present in the simulation which in turn leads to more ionic interactions. The 2D geometry restricts these ions from being close to as many other ions therefore the model may predict less significant ionic interactions for the high concentrations. Extending the simulation to three dimensions could bring new insights into the ionic and solvent-ion interactions that occur.

4 Single-Particle Models

The development of accurate electrochemical cell models is often held back by the complexity of the resulting equations, making them extremely intensive to solve. For example, including non-linear diffusion, working in three dimensions, investigating the specific chemistries of electrode and electrolyte materials and working with multiple scales, from the microscopic equations within electrode particles to the macroscopic scale of transport in the electrolyte.

In an effort to simplify these models while still retaining their accuracy and validity, the single-particle model has been developed. This method reduces the complexity of the equations involved by considering just a single representative particle for each electrode. This comes with the assumption that the particles in the electrode are all equal in shape and size, and the rates of the redox reactions occurring are not dependent on the location within the electrode. This method can also be extended to graded electrodes (Richardson et al., 2020).

It has been demonstrated that making use of a single-particle model still maintains high accuracy while being significantly less computationally intensive. Research includes studying the cycling life (Ning and Popov, 2004),(Santhanagopalan et al., 2006), side reactions and their effect on electrode degradation (Li et al., 2018)(Planella and Widanage, 2023) and charge/discharge behaviour under various temperatures (Guo, Sikha and White, 2010).

In this chapter, we study a single-particle model derived from the Doyle-Fuller-Newman (DFN) model. To start, we will introduce the DFN model and set out the equations for a full electrochemical cell, with a discussion on important parameters. We will non-dimensionalise the model and follow the asymptotic method applied in (Richardson et al., 2020) for the resulting single-particle model. We will then discuss possible ways this model could be developed or the sorts of situations in which it could be applied.

4.1 The Full-Cell Doyle-Fuller-Newman Model

The Doyle-Fuller-Newman model is a popular electrochemical model presented in (Doyle, Fuller and Newman, 1993). It incorporates all aspects of an electrochemical

cell to model the charge transport in the electrodes and the electrolyte phases, as well as the intercalation of lithium ions into the electrode materials and the reaction rates occurring on the electrode surfaces. Here, we summarise the model for a full electrochemical cell:

As shown in Figure 10, we use the following setup:
The anode occupies the region between $L_1 < x < L_2$.
The separator occupies the region between $L_2 < x < L_3$.
The cathode occupies the region between $L_3 < x < L_4$.
The electrolyte occupies the region between $L_1 < x < L_4$.
The current collectors are located at $x = L_1$ and $x = L_4$.

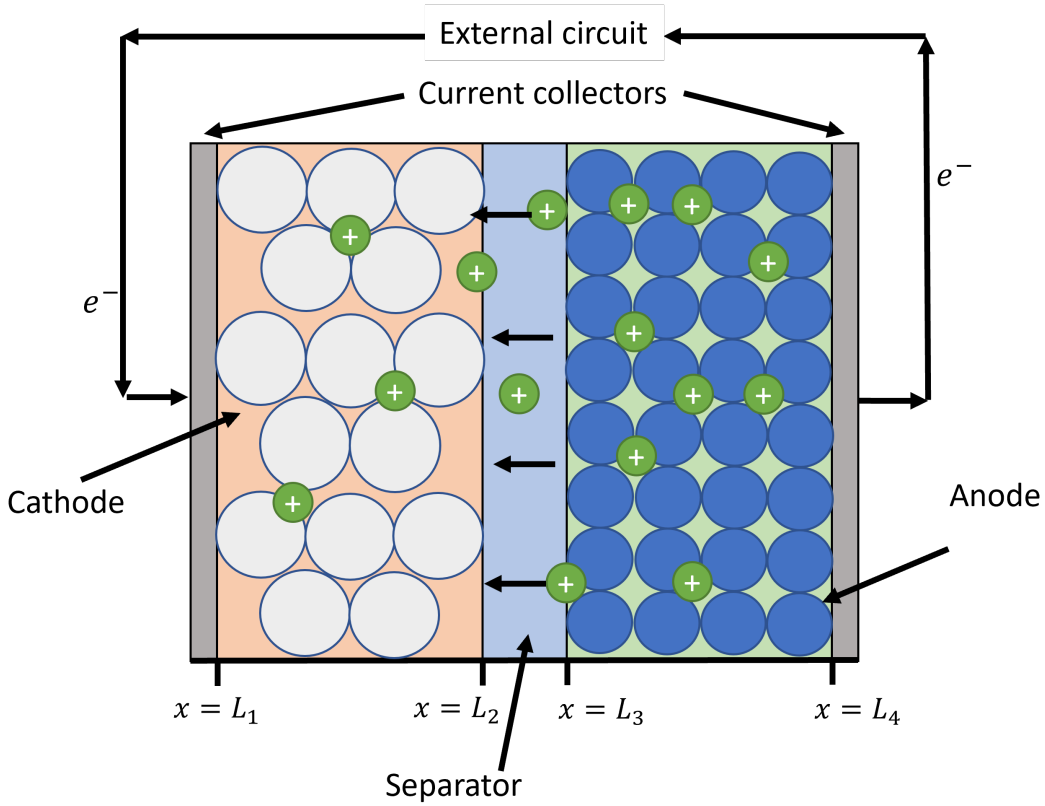

Figure 10: A diagram of the setup used for the DFN model for a full electrochemical cell. Here, we show the movements of the lithium ions and the electrons during the discharge of the cell.

Macroscopic Equations We begin by discussing the macroscopic equations for the electrolyte and the electrodes. Consider a binary 1:1 electrolyte composed of lithium ions Li^+ and a negative ion N^- in a solvent. In the following equations we will be using N_- to denote the flux of the negative ions in the electrolyte. These

equations could also have been stated in terms of the flux of the lithium ions; we have chosen to define the equations in terms of the negative ions as no additional terms will be required to account for the redox reactions, as would have been the case with the lithium ions (Richardson et al., 2020).

We also have an electrolyte concentration $c_e(x,t)$ and the potential in the electrolyte Φ_e, which is generally given with respect to that of a lithium electrode. j is the current density in the electrolyte, while j_n is the current density on the surface of the electrode particles, which is determined by the rate of the redox reactions occurring on this surface. As given in (Richardson et al., 2020) and (Korotkin et al., 2021), the equations for the electrolyte are given by:

In the region $L_1 < x < L_4$

$$\varepsilon_{el}\frac{\partial c_e}{\partial t} + \frac{\partial N_-}{\partial x} = 0, \qquad N_- = -B(x)D_e(c_e)\frac{\partial c_e}{\partial x} - (1-t^+)\frac{j}{F} \tag{4.1}$$

$$\frac{\partial j}{\partial x} = b_{et}(x)j_n(x,t), \qquad j = -B(x)\kappa(c_e)\left(\frac{\partial \Phi_e}{\partial x} - \frac{2R_gT(1-t^+)}{Fc_e}\frac{\partial c_e}{\partial x}\right) \tag{4.2}$$

Equation [4.1] describes the ionic transport through the electrolyte, while equation [4.2] maintains conservation of charge from the current transfer at the electrode surfaces through the electrolyte. Here, $\varepsilon_{el}(x)$ is known as the electrolyte phase volume fraction, which can be defined as (analogous to the definition of mole fraction) the volume of the specific substance divided by the volume of all substances. Its value varies throughout the electrodes and the separator (Xu et al., 2017). $B(x)$ is the permeability factor that depends on the electrode material. It can often be approximated from the Bruggeman relation where $B(x) = (\varepsilon_{el})^{\frac{3}{2}}$ (Richardson et al., 2020), however it has been argued that using this relation can lead to larger values for $B(x)$ than the true values (Zülke et al., 2021).

The diffusivity of the electrolyte is denoted $D_e(c_e)$, which describes the extent that the electrolyte allows the diffusive movements of the ions; higher values allow the ions to diffuse more rapidly. Similarly, κ refers to the conductivity of the electrolyte, which depends on the choice of electrolyte. Stronger electrolytes dissociate more fully into ions, meaning more ions are available to carry charge, therefore leading to higher conductivities.

The transference number is denoted t^+, which gives a measure of the amount of charge that is carried by the Li^+ ions. As we are considering the negative ions, we instead include the term $(1 - t^+)$. The Brunauer-Emmett-Teller (commonly shortened to BET) surface area gives a measure of the surface area of the electrode particles that are able to interact with the electrolyte relative to the electrode's volume. Here we have denoted it as $b_{et}(x)$ (Zulke et al., 2021). Finally, R_g, T and F are the universal gas constant, temperature and Faraday's constant, respectively.

Next, we look at the macroscopic equations for the electrodes, equation [4.3] gives the conservation equations for charge in the anode, with equation [4.4] being the relative one for the cathode. We have denoted the current densities, the electric potentials and the conductivities for the anode and cathode as $j_a, j_c, \Phi_a, \Phi_c, \sigma_a, \sigma_c$.

In the region $L_1 < x < L_2$

$$\frac{\partial j_a}{\partial x} = -b_{et}(x) j_n, \qquad j_a = -\sigma \frac{\partial \Phi_a}{\partial x} \tag{4.3}$$

In the region $L_3 < x < L_4$

$$\frac{\partial j_c}{\partial x} = -b_{et}(x) j_n, \qquad j_c = -\sigma \frac{\partial \Phi_c}{\partial x} \tag{4.4}$$

The current density on the surface of the electrode particles can be given by the Butler-Volmer equation, which describes the kinetics of the reaction rates of the redox reactions as functions of overpotentials. Here, we denote the concentrations of lithium ions in the electrode particles as c_a and c_c with c_a^{max} and c_c^{max} as the maximum concentration of lithium ions in the anode and cathode, respectively.

$$j_n = \begin{cases} 2Fk_a c_e^{1/2} (c_a|_{r=R_a(x)})^{1/2} (c_a^{max} - c_a|_{r=R_a(x)})^{1/2} \sinh\left(\frac{F\eta_a}{2R_gT}\right) & \text{in} \quad L_1 \leq x < L_2, \\ 0 & \text{in} \quad L_2 < x < L_3, \\ 2Fk_c c_e^{1/2} (c_c|_{r=R_c(x)})^{1/2} (c_c^{max} - c_c|_{r=R_c(x)})^{1/2} \sinh\left(\frac{F\eta_c}{2R_gT}\right) & \text{in} \quad L_3 \leq x < L_4. \end{cases} \tag{4.5}$$

The overpotentials η_a, η_c can be defined in terms of the difference in potential between the electrolyte Φ_e and the electrode particles Φ_a, Φ_c minus the equilibrium potential of the electrode $U_{eq,a}, U_{eq,c}$. These equilibrium potentials can also be referred to as open circuit potentials, and they depend on the electrochemical properties of the electrode materials.

$$\eta_a = \Phi_a - \Phi_e - U_{eq,a}(c_a|_{r=R_a(x)}) \qquad \eta_c = \Phi_c - \Phi_e - U_{eq,c}(c_c|_{r=R_c(x)}). \quad [4.6]$$

Next, we introduce the boundary conditions for these equations:

$$N_-|_{x=L_1} = 0 \qquad N_-|_{x=L_4} = 0. \quad [4.7]$$

$$j_a|_{x=L_1} = \frac{I(t)}{A} \qquad j_a|_{x=L_2} = 0, \quad [4.8]$$

$$j_c|_{x=L_3} = 0 \qquad j_c|_{x=L_4} = \frac{I(t)}{A}, \quad [4.9]$$

$$j|_{x=L_1} = 0 \qquad j|_{x=L_4} = 0, \quad [4.10]$$

and an initial condition for the lithium concentration in the electrolyte:

$$c_e|_{t=0} = c_0. \quad [4.11]$$

At each end of the cell, where the current collectors are located, there is no movement of negative ions into or out of the current collectors, therefore it follows that the negative ion flux N_- at each boundary is 0. Similarly, at the boundaries where the electrodes meet the separator, the current densities j_a, j_c must be 0, whereas the current densities on the boundaries of the electrodes must be equal to the current density supplied by (or to) the external circuit. This current density is given by the current $I(t)$ divided by the area of the electrode's cross-section, A.

Microscopic Equations We are now interested in transport equations for within the electrode particles, this is when $r < R_a(x), R_c(x)$, the distance from the centre of the particle relative to the radii of the electrode particles. To allow for the variance of particle sizes along the electrode, we have denoted these radii as functions of x.

$$\frac{\partial c_a}{\partial t} = \frac{1}{r^2}\frac{\partial}{\partial r}\left[r^2 D_a(c_a)\frac{\partial c_a}{\partial r}\right] \quad \text{in} \quad 0 < r < R_a(x) \quad \text{for} \quad L_1 < x < L_2 \quad [4.12]$$

$$\frac{\partial c_c}{\partial t} = \frac{1}{r^2}\frac{\partial}{\partial r}\left[r^2 D_c(c_c)\frac{\partial c_c}{\partial r}\right] \quad \text{in} \quad 0 < r < R_c(x) \quad \text{for} \quad L_3 < x < L_4 \quad [4.13]$$

where $D_a(c_a)$ and $D_c(c_c)$ are the diffusivities of the respective electrode's particles.

We require that the change in concentration of lithium at the centre of the particles must equal 0, while on the particle surfaces it must be proportional to the surface current density. Therefore, we define the boundary conditions as:

$$\left.\frac{\partial c_a}{\partial r}\right|_{r=0} = 0, \qquad \left.\frac{\partial c_a}{\partial r}\right|_{r=R_a(x)} = -\frac{j_n}{D_a(c_a)F} \quad \text{for} \quad L_1 > x > L_2 \qquad [4.14]$$

$$\left.\frac{\partial c_c}{\partial r}\right|_{r=0} = 0, \qquad \left.\frac{\partial c_c}{\partial r}\right|_{r=R_c(x)} = -\frac{j_n}{D_c(c_c)F} \quad \text{for} \quad L_3 > x > L_4. \qquad [4.15]$$

We also require initial conditions on the concentrations, this time for c_a and c_c, we define:

$$c_a|_{t=0} = c_{0,a} \qquad [4.16]$$

$$c_c|_{t=0} = c_{0,c}. \qquad [4.17]$$

While setting up this model, we have introduced new parameters, Table 7 summarises these parameters with their descriptions and values. In this model, these parameters are all taken to be constants.

Table 7: Values and descriptions of parameters introduced in the model.

Parameter	Description	Value	Reference
ε_{el}	Electrolyte volume fraction	0.3407	(Srinivasan, and Newman, 2004)
k_a	Butler-Volmer rate constant for the anodic reaction	2.28x10^{-11} $m^{2.5}$ s^{-1} $mol^{-0.5}$	(Malifarge et al., 2018)
k_c	Butler-Volmer rate constant for the cathodic reaction	3x10^{-12} $m^{2.5}$ s^{-1} $mol^{-0.5}$	(Srinivasan, and Newman, 2004)
$L_2 - L_1$	Typical thickness of the cathode	6.2x10^{-5} m	(Srinivasan, and Newman, 2004)
$L_3 - L_2$	Typical thickness of the separator	2.5x10^{-5} m	(Malifarge et al., 2018)
$L_4 - L_3$	Typical thickness of the anode	7.4x10^{-5} m	(Ecker et al., 2015)
T	Temperature	298 K	(Srinivasan, and Newman, 2004)
t^+	Transference number	0.38	(Valen and Reimers, 2005)

4.1.1 Non-Dimensionalisation

Here, we introduce some parameters that are representative of the typical scale of the variables in the model in order to non-dimensionalise the equations. These are the scalings used in (Richardson et al., 2020), here we will include a table describing the parameters used and give approximate values, these are shown in Table 8 along with any derived dimensionless parameters in Table 9.

$$t = \tau t^* \qquad x = Lx^* \qquad r = \hat{R}r^* \qquad R = \hat{R}R^* \tag{4.18}$$

$$D_e = \hat{D}_e D_e^* \quad D_s = \hat{D}_s D_s^* \quad \kappa = \hat{\kappa}\kappa^* \quad c_e = c_0 c_e^* \tag{4.19}$$

$$c_s = c_s^{max} c_s^* \quad \Phi_e = \frac{R_g T}{F}\Phi_e^* \quad \Phi_s = \hat{U}\Phi_s^* \quad j = \frac{\hat{I}}{A}j^* \tag{4.20}$$

$$j_s = \frac{\hat{I}}{A}j_s^* \quad j_n = \frac{\hat{I}}{AL\hat{b}}j_n^* \quad I = \hat{I}I^*\eta_s = \frac{R_g T}{F}\eta_s^* \tag{4.21}$$

$$U_{eq,s} = \hat{U}U_{eq,s}^* \quad N_- = \frac{\hat{B}\hat{D}_e c_0}{L}N_-^* \quad B = \hat{B}B^* \tag{4.22}$$

$$b_{et} = \hat{b}b_{et}^* \quad \sigma = \hat{\sigma}\sigma^* \quad L_i = LL_i^* \tag{4.23}$$

Size of Parameters Here, we are scaling most quantities with their typical values. We scale x by the typical value of the width of the electrochemical cell, denoted L and similarly, where the boundary conditions rely on the widths of specific parts of the cell we have also scaled $L_i, i = 1, 2, 3, 4$ by the total width L. The radial coordinate, r, is scaled by the average radius of the electrode particles. This radius can differ for the anode and cathode as it depends on the material chosen, we chose to study a Graphite (LiC_6) anode and a Lithium Iron Phosphate ($LiFePO_4$) cathode. A typical current that the cell is able to sustain when discharged is denoted at $\hat{I}$ and the time coordinate t is scaled by the typical timescale over which a cell will discharge with the given current $\hat{I}$, we have denoted this timescale as τ.

The diffusivities in the electrolyte and both electrodes will vary depending on the materials chosen, so each have been scaled separately by a typical value for the diffusion coefficient in the specific medium. We have chosen to consider a lithium hexafluorophosphate ($LiPF_6$) electrolyte and its diffusivity has been scaled by $\hat{D}_e$. Similarly, the diffusivities in the anode and cathode have been scaled by $\hat{D}_a$ and $\hat{D}_c$, and the conductivities in the electrolyte and the electrodes have been scaled by their typical values, κ and σ, respectively.

The concentrations in the electrolyte phase and each electrode have been scaled individually. In the electrolyte, the initial lithium salt concentration is assumed to be uniform, this leads from the assumption of the cell being at equilibrium and so there is no current flow. The electrolyte concentration has been scaled by this initial value, denoted c_0. For each electrode, there is a maximum concentration of lithium that can be intercalated into material, this depends on the material chosen and

its structure. We have scaled the lithium concentration in each electrode by these maximum values, namely c_a^{max} and c_c^{max} for the anode and cathode respectively.

Table 8: Descriptions and typical values of the parameters introduced in equations [4.18] - [4.23]. Here, our chosen anode is Graphite (LiC_6) and our chosen cathode is Lithium Iron Phosphate ($LiFePO_4$)

Parameter	Description	Value	Reference
A	Typical electrode cross-sectional area	1.54x10^{-4} m^2	(Malifarge et al., 2018)
$\hat{B}$	Typical permeability factor of electrolyte	0.1989	Calculated using Bruggeman relation (Richardson et al., 2020)
$\hat{b}$	Typical Brunauer-Emmett-Teller surface area for electrode	2.7x10^6 m^2 kg^{-1}	(Duan et al., 2023)
c_0	Typical lithium concentration in the electrolyte	1000 mol m^{-3}	(Richardson and King, 2007)
c_a^{max}	Maximum lithium concentration in the anode	31920 mol m^{-3}	(Ecker et al., 2015)
c_c^{max}	Maximum lithium concentration in the cathode	20950 mol m^{-3}	(Srinivasan and Newman, 2004)
D_a	Typical diffusivity in the anode	7x10^{-14} m^2 s^{-1}	(Ecker et al., 2015)
D_c	Typical diffusivity in the cathode	8x10^{-18} m^2 s^{-1}	(Srinivasan and Newman, 2004)
$\hat{D}_e$	Typical diffusivity of the electrolyte	5.34x10^{-10} m^2 s^{-1}	(Srinivasan and Newman, 2004)
$\hat{I}$	Typical current draw	0.0015 A	(Srinivasan and Newman, 2004)
$\hat{\kappa}$	Typical conductivity of the electrolyte	1 S m^{-1}	(Valen and Reimers, 2005)
L	Typical thickness of the electrochemical cell	1.6x10^{-4} m	(Ecker et al., 2015)
$\hat{R}_a$	Typical radius of the anode particles	1.37x10^{-5} m	(Ecker et al., 2015)
$\hat{R}_c$	Typical radius of the cathode particles	5.2x10^{-8} m	(Srinivasan and Newman, 2004)
$\hat{\sigma}$	Typical conductivity of the electrode	0.5 S m^{-1}	(Ecker et al., 2015)
τ	Typical time-scale for discharge process	1.7x10^5 s	(Srinivasan and Newman, 2004)
U	Typical change in overpotential during discharge	0.2 V	(Srinivasan and Newman, 2004)

The permeability of the electrolyte and the BET surface area for the electrodes are scaled by their typical values, denoted $\hat{B}$ and $\hat{b}$. The value for $\hat{B}$ shown in Table 8 was calculated using the Bruggeman relation $\hat{B} = (\varepsilon)^{\frac{3}{2}}$ (Richardson et al.,2020) using the value for the volume fraction from Table 7. Both the open-circuit potentials $U_{eq,s}$ and the electric potentials Φ_s of the electrodes related directly to the overpotentials η_s by equation [4.6], so we have chosen to scale these values by a typical change in this overpotential, denoted $\hat{U}$. For the electric potential in the electrolyte Φ_e, we have chosen to scale by $\frac{R_g T}{F}$ which denotes the thermal voltage. In the case of electrolytes, this can be defined as the voltage generated by the heat from the ion movements. This was used to scale the electrolyte potential as it is typically a good measure of the amount of variation of the potential across the electrolyte.

A typical value for the flux of the negative ions in the electrolyte is described by the diffusive flux (recall equation [2.4]) for the initial concentration with the diffusion coefficient being multiplied by $\hat{B}$. This accounts for the effect that the permeability of the solution has on the ion movements. This is then divided by the scale of the distance the ions must diffuse, namely the length scale of the electrochemical cell L.

The current densities of the electrode and electrolyte j_a, j_c and j are simply the typical current through the cell divided by the cross-sectional area of the electrode, while the transfer current density on the surface of the electrode depends on the surface reaction rates and so must additionally be divided by BET surface area $\hat{b}$ that determines the proportion of the electrode's surface area that able to interact with the electrolyte.

All of these values are summarised in Table 8 with their descriptions and approximate values from the literature. The non-dimensionalisation process then leads to the introduction of some derived dimensionless parameters, these are summarised in Table 9 with their values calculated using the values in Table 8.

Electrolyte Equations Applying the non-dimensionalisation using the scalings in equations [4.18] - [4.23] to the electrolyte equations [4.1] - [4.2] leads to:

$$\varepsilon_l\left[\frac{L^2}{\hat{B}\hat{D}_e\tau}\right]\frac{\partial c_e^*}{\partial t^*}+\frac{\partial N_-^*}{\partial x^*}=0, \qquad \left[\frac{\hat{B}\hat{D}_e c_0}{L}\right]N_-^*=-\left[\frac{\hat{B}\hat{D}_e c_0}{L}\right]B^*D_e^*\frac{\partial c_e^*}{\partial x^*}-(1-t^+)j^*\frac{\hat{I}}{AF}, \quad [4.24]$$

$$\frac{\hat{I}}{LA}\frac{\partial j^*}{\partial x^*}=\frac{\hat{I}}{LA}b_{et}j_n^*, \qquad j^*=-\left[\frac{AR_gT\hat{B}\hat{\kappa}}{FL\hat{I}}\right]B(x)\kappa(c)\left(\frac{\partial \Phi_e^*}{\partial x^*}-\frac{2(1-t^+)}{c_e^*}\frac{\partial c_e^*}{\partial x^*}\right), \quad [4.25]$$

which simplifies to (and dropping the stars for easier notation):

$$\varepsilon_{el}\mathcal{N}\frac{\partial c_e}{\partial t}+\frac{\partial N_-}{\partial x}=0, \qquad N_-=-BD_e\frac{\partial c_e}{\partial x}-\Gamma(1-t^+)j, \quad [4.26]$$

$$\frac{\partial j}{\partial x}=b_{et}j_n, \qquad j=-PB\kappa\left(\frac{\partial \Phi_e}{\partial x}-\frac{2(1-t^+)}{c_e}\frac{\partial c_e}{\partial x}\right), \quad [4.27]$$

where we have introduced:

$$\mathcal{N} = \frac{L^2}{\tau \hat{B} \hat{D}_e}, \qquad \Gamma = \frac{\hat{I} L}{A \hat{D}_e \hat{B} F c_0}, \qquad P = \frac{A R_g T \hat{B} \hat{\kappa}}{F L \hat{I}}. \tag{4.28}$$

The non-dimensional boundary conditions become:

$$j^*|_{x^*=L_1^*} = 0, \qquad j^*|_{x^*=L_4^*} = 0, \qquad N_-^*|_{x^*=L_1^*} = 0, \qquad N_-^*|_{x^*=L_4^*} = 0, \tag{4.29}$$

and initial condition:

$$c_e^*|_{t^*=0} = 1. \tag{4.30}$$

Here, we have introduced the derived dimensionless parameters $\mathcal{N}, \Gamma, P$ which are summarised with approximate values in Table 9. $\frac{L^2}{\hat{B}\hat{D}_e}$ gives a measure of the timescale for the diffusion through the electrolyte, therefore $\mathcal{N}$ gives the ratio of this diffusion timescale to the timescale for cell discharge. $\frac{\hat{B}\hat{D}c_0}{L}$ represents the typical diffusive flux and $\frac{\hat{I}}{AF}$ represents a typical drift flux in the electrolyte due to the electric field and so Γ gives the ratio of diffusive flux to drift flux in the electrolyte.

Table 9: Values of the derived dimensionless parameters introduced in equations [4.28], [4.39] and [4.45] using the values in Table 8.

Parameter	Value
$\Gamma = \frac{\hat{I}L}{A\hat{D}_e\hat{B}Fc_0}$	0.152
$\Theta = \frac{\hat{\sigma}R_gTA}{L\hat{I}F}$	8.24
$\lambda = \frac{\hat{U}F}{R_gT}$	7.79
$\mathcal{N} = \frac{L^2}{\tau\hat{B}\hat{D}_e}$	0.00142
$P = \frac{AR_gT\hat{B}\hat{\kappa}}{FL\hat{I}}$	3.28
$\mathcal{Q} = \frac{\hat{R}^2}{\tau\hat{D}_s}$	1.99x10^{-3}
$\Upsilon = \frac{Fk_sAL\hat{b}c_s^{max}{c_0}^{1/2}}{\hat{I}}$	8.51

$\frac{R_gT}{F}$ denotes the thermal voltage which is linked to the ionic movements. This leads to $\frac{R_gT\hat{B}}{FL}$ describing these ionic movements across a distance L with electrolyte permeability $\hat{B}$. Multiplying this by the conductivity of the electrolyte, $\hat{\kappa}$ therefore gives a measure of the ionic conductivity as these ions move through the electrolyte. P gives a measure of this ionic conductivity divided by the current density of the electrode (Richardson et al., 2020).

Electrode Equations Similarly, applying the scalings in equations [4.18] - [4.23] to equations for the electrodes [4.3] - [4.6] leads to:

$$\frac{\hat{I}}{AL}\frac{\partial j_a^*}{\partial x^*} = -\frac{\hat{I}\hat{b}}{AL\hat{b}} b_{et}^* j_n^*, \qquad \frac{\hat{I}}{A} j_a^* = -\hat{\sigma}\sigma^* \frac{\hat{U}}{L}\frac{\partial \Phi_a^*}{\partial x^*} \tag{4.31}$$

$$\frac{\hat{I}}{AL}\frac{\partial j_c^*}{\partial x^*} = -\frac{\hat{I}\hat{b}}{AL\hat{b}} b_{et}^* j_n^*, \qquad \frac{\hat{I}}{A} j_c^* = -\hat{\sigma}\sigma^* \frac{\hat{U}}{L}\frac{\partial \Phi_c^*}{\partial x^*} \tag{4.32}$$

$$\frac{\hat{I}}{AL\hat{b}} j_n^* = \begin{cases} 2Fkc_a^{max}(c_0 c_e^* c_a^*|_{r^*=R_a^*})^{1/2}(1 - c_a^*|_{r^*=R_a^*})^{1/2} \sinh\left(\frac{R_gT}{F}\frac{F\eta_a^*}{2R_gT}\right) & \text{in} \quad L_1^* < x^* < L_2^*, \\ 0 & \text{in} \quad L_2^* < x^* < L_3^*, \\ 2Fkc_c^{max}(c_0 c_e^* c_c^*|_{r^*=R_c^*})^{1/2}(1 - c_c^*|_{r^*=R_c^*})^{1/2} \sinh\left(\frac{R_gT}{F}\frac{F\eta_c^*}{2R_gT}\right) & \text{in} \quad L_3^* < x^* < L_4^*. \end{cases} \tag{4.33}$$

$$\frac{R_gT}{F}\eta_a^* = \hat{U}\Phi_a^* - \frac{R_gT}{F}\Phi_e^* - \hat{U}U_{eq,a}^* \qquad \frac{R_gT}{F}\eta_c^* = \hat{U}\Phi_c^* - \frac{R_gT}{F}\Phi_e^* - \hat{U}U_{eq,c}^*. \tag{4.34}$$

These simplify to (where we have also dropped the stars in notation):

$$\frac{\partial j_a}{\partial x} = -b_{et} j_n, \qquad j_a = -\Theta\lambda\sigma\frac{\partial \Phi_a}{\partial x}, \tag{4.35}$$

$$\frac{\partial j_c}{\partial x} = -b_{et} j_n, \qquad j_c = -\Theta\lambda\sigma\frac{\partial \Phi_c}{\partial x}, \tag{4.36}$$

$$j_n = \begin{cases} 2\Upsilon(c_e c_a|_{r=R_a})^{1/2}(1 - c_a|_{r=R_a})^{1/2} \sinh\left(\frac{\eta_a}{2}\right) & \text{in} \quad L_1 < x < L_2, \\ 0 & \text{in} \quad L_2 < x < L_3, \\ 2\Upsilon(c_e c_c|_{r=R_c})^{1/2}(1 - c_c|_{r=R_c})^{1/2} \sinh\left(\frac{\eta_c}{2}\right) & \text{in} \quad L_3 < x < L_4, \end{cases} \tag{4.37}$$

$$\eta_a = \lambda(\Phi_a - U_{eq,a}) - \Phi_e \qquad \eta_c = \lambda(\Phi_c - U_{eq,c}) - \Phi_e. \tag{4.38}$$

where:

$$\Theta = \frac{\hat{\sigma} R_g T A}{L\hat{I}F}, \qquad \lambda = \frac{\hat{U}F}{R_gT}, \qquad \Upsilon = \frac{Fk_s AL\hat{b}c_s^{max}{c_0}^{1/2}}{\hat{I}} \tag{4.39}$$

As before, we can apply the non-dimensionalisation to the boundary conditions:

$$j_a^*|_{x^*=L_1^*} = I(t) \qquad j_a^*|_{x^*=L_2^*} = 0, \tag{4.40}$$

$$j_c^*|_{x^*=L_3^*} = 0 \qquad j_c^*|_{x^*=L_4^*} = I(t), \tag{4.41}$$

Here, we have introduced the dimensionless parameters $\Theta, \lambda, \Upsilon$, approximate values are shown in Table 9. Θ is almost analogous to P in the electrolyte equations in that represents the ionic conductivity in the electrodes divided by the current density. λ is the ratio of the characteristic cell voltage to the thermal voltage from the ionic movements. Υ is the rate of lithium insertion into the electrode materials divided by the current density on the surface of the electrode.

Electrode Particles Equations Continuing, we now apply the non-dimensionalisation to the equations describing within the electrode particles. As before, we apply the scalings in equations [4.18] - [4.23] to equations [4.12] and [4.13], which leads to:

$$\frac{\hat{R}_s^{\,2}}{\tau \hat{D}_a}\frac{\partial c_a^*}{\partial t^*} = \frac{1}{r^{*2}}\frac{\partial}{\partial r^*}\left[r^{*2} D_a^* \frac{\partial c_a^*}{\partial r^*}\right], \qquad \frac{\hat{R}_s^{\,2}}{\tau \hat{D}_c}\frac{\partial c_c^*}{\partial t^*} = \frac{1}{r^{*2}}\frac{\partial}{\partial r^*}\left[r^{*2} D_c^* \frac{\partial c_c^*}{\partial r^*}\right], \tag{4.42}$$

which we simplify to (dropping the stars in notation):

$$\mathcal{Q}\frac{\partial c_a}{\partial t} = \frac{1}{r^2}\frac{\partial}{\partial r}\left[r^2 D_a \frac{\partial c_a}{\partial r}\right], \qquad \mathcal{Q}\frac{\partial c_c}{\partial t} = \frac{1}{r^2}\frac{\partial}{\partial r}\left[r^2 D_c \frac{\partial c_c}{\partial r}\right], \tag{4.43}$$

where we have introduced the characteristic timescale for the cell discharge as:

$$\tau = \frac{FAL\hat{b}c_s^{max}\hat{R}}{\hat{I}} \tag{4.44}$$

and so the terms on the left side of equations [4.42]a) and b) have been simplified by introducing:

$$\mathcal{Q} = \frac{\hat{R}^2}{\tau \hat{D}_s}. \tag{4.45}$$

Here, $\mathcal{Q}$ is analogous to $\mathcal{N}$ for the electrode particles, it gives the ratio of the timescale for the diffusive flux through the electrode particles relative to the timescale for the cell discharge.

Applying this to the boundary conditions [4.14]and [4.15] leads to:

$$\frac{\partial c_a^*}{\partial r^*}\Big|_{r^*=0} = 0, \qquad \frac{\partial c_c^*}{\partial r^*}\Big|_{r^*=0} = 0 \tag{4.46}$$

$$\frac{FAL\hat{b}\hat{D}_a c_a^{max}}{\hat{R}\hat{I}} \frac{\partial c_a^*}{\partial r^*}\Big|_{r^*=R_a^*} = -\frac{j_n^*}{D_a^*} \qquad \frac{FAL\hat{b}\hat{D}_c c_c^{max}}{\hat{R}\hat{I}} \frac{\partial c_c^*}{\partial r^*}\Big|_{r^*=R_c^*} = -\frac{j_n^*}{D_c^*} \tag{4.47}$$

which we simplify to:

$$\frac{\partial c_a^*}{\partial r^*}\Big|_{r^*=0} = 0, \qquad \frac{\partial c_c^*}{\partial r^*}\Big|_{r^*=0} = 0 \tag{4.48}$$

$$\frac{\partial c_a^*}{\partial r^*}\Big|_{r^*=R_a^*} = -\frac{\mathcal{Q} j_n^*}{D_a^*} \qquad \frac{\partial c_c^*}{\partial r^*}\Big|_{r^*=R_c^*} = -\frac{\mathcal{Q} j_n^*}{D_c^*} \tag{4.49}$$

Finally, for the initial conditions [4.16] and [4.51], we find:

$$c_a^*|_{t=0} = \frac{c_{0,a}}{c_a^{max}} \tag{4.50}$$

$$c_c^*|_{t=0} = \frac{c_{0,c}}{c_c^{max}}. \tag{4.51}$$

4.2 Summary of Full Cell Dimensionless Model

Macroscopic equations:

$$\varepsilon_l \mathcal{N}\frac{\partial c_e}{\partial t} + \frac{\partial N_-}{\partial x} = 0, \qquad N_- = -BD_e(c_e)\frac{\partial c_e}{\partial x} - \Gamma(1-t^+)j \tag{4.52}$$

$$\frac{\partial j}{\partial x} = b_{et} j_n, \qquad j = -PB\kappa\left(\frac{\partial \Phi_e}{\partial x} - \frac{2(1-t^+)}{c_e}\frac{\partial c_e}{\partial x}\right) \tag{4.53}$$

$$\frac{\partial j_a}{\partial x} = -b_{et} j_n, \qquad j_a = -\Theta\lambda\sigma\frac{\partial \Phi_a}{\partial x} \tag{4.54}$$

$$\frac{\partial j_c}{\partial x} = -b_{et} j_n, \qquad j_c = -\Theta\lambda\sigma\frac{\partial \Phi_c}{\partial x} \tag{4.55}$$

$$j_n = \begin{cases} 2\Upsilon(c_e c_a|_{r=R_a})^{1/2}(1-c_a|_{r=R_a})^{1/2}\sinh\left(\frac{\eta_a}{2}\right) & \text{in} \quad L_1 < x < L_2, \\ 0 & \text{in} \quad L_2 < x < L_3, \\ 2\Upsilon(c_e c_c|_{r=R_c})^{1/2}(1-c_c|_{r=R_c})^{1/2}\sinh\left(\frac{\eta_c}{2}\right) & \text{in} \quad L_3 < x < L_4. \end{cases} \tag{4.56}$$

$$\eta_a = \lambda(\Phi_a - U_{eq,a}(c_a|_{r=R_a})) - \Phi_e \qquad \eta_c = \lambda(\Phi_c - U_{eq,c}(c_c|_{r=R_c})) - \Phi_e. \tag{4.57}$$

with boundary conditions and initial condition:

$$j_a|_{x=L_1} = I(t) \qquad j_a|_{x=L_2} = 0, \tag{4.58}$$

$$j_c|_{x=L_3} = 0 \qquad j_c|_{x=L_4} = I(t), \tag{4.59}$$

$$c_e|_{t=0} = 1 \qquad c_a|_{t=0} = \frac{c_{0,a}}{c_a^{max}}. \qquad c_a|_{t=0} = \frac{c_{0,c}}{c_c^{max}}. \tag{4.60}$$

$$j|_{x=L_1} = 0 \qquad j|_{x=L_4} = 0 \tag{4.61}$$

$$N_-|_{x=L_1} = 0 \qquad N_-|_{x=L_4} = 0 \tag{4.62}$$

Microscopic equations: For $0 < r < R_s(x)$

$$\text{In} \quad L_1 < x < L_2 \qquad \mathcal{Q}\frac{\partial c_a}{\partial t} = \frac{1}{r^2}\frac{\partial}{\partial r}\left[r^2 D_a(c_a)\frac{\partial c_a}{\partial r}\right], \tag{4.63}$$

$$\frac{\partial c_a}{\partial r}\Big|_{r=0} = 0, \qquad \frac{\partial c_a}{\partial r}\Big|_{r=R_a(x)} = -\frac{\mathcal{Q} j_n}{D_a(c_a)}. \tag{4.64}$$

$$\text{In} \quad L_3 < x < L_4 \qquad \mathcal{Q}\frac{\partial c_c}{\partial t} = \frac{1}{r^2}\frac{\partial}{\partial r}\left[r^2 D_c(c_c)\frac{\partial c_c}{\partial r}\right], \tag{4.65}$$

$$\frac{\partial c_c}{\partial r}\Big|_{r=0} = 0, \qquad \frac{\partial c_c}{\partial r}\Big|_{r=R_c(x)} = -\frac{\mathcal{Q} j_n}{D_c(c_c)}, \tag{4.66}$$

where, for $s = a, c$:

$$\mathcal{Q} = \frac{\hat{R}^2}{\tau \hat{D}_s} \qquad \tau = \frac{FAL\hat{b}c_s^{max}\hat{R}}{\hat{I}} \qquad \mathcal{N} = \frac{L^2}{\tau \hat{B}\hat{D}}, \qquad \Gamma = \frac{\hat{I}L}{A\hat{D}\hat{B}Fc_0} \quad [4.67]$$

$$P = \frac{AR_gT\hat{B}\hat{\kappa}}{FL\hat{I}}, \qquad \Theta = \frac{\hat{\sigma}R_gTA}{L\hat{I}F}, \qquad \lambda = \frac{\hat{U}F}{R_gT}, \qquad \Upsilon = \frac{FkAL\hat{b}c_s^{max}{c_0}^{1/2}}{\hat{I}} \quad [4.68]$$

The full cell potential can then be calculated from the following relation:

$$V(t) = V_c(t) - V_a(t), \quad [4.69]$$

where:

$$V_a(t) = \Phi_a|_{x=L_1}, \qquad V_c(t) = \Phi_c|_{x=L_4}. \quad [4.70]$$

4.3 Asymptotic Expansions

Following the derivation in (Richardson et al., 2020), we will apply asymptotic analysis to derive the leading order terms and first-order correction terms for the single-particle model for a full cell.
Using the following expansions:

$$\Phi_s = \Phi_{s,0} + \frac{1}{\lambda}\Phi_{s,1} + ..., \qquad V = V_0 + \frac{1}{\lambda}V_1 + ..., \qquad c_s = c_{s,0} + \frac{1}{\lambda}c_{s,1} + ..., \quad [4.71]$$

$$j_s = j_{s,0} + \frac{1}{\lambda}j_{s,1} + ..., \qquad \eta = \eta_0 + \frac{1}{\lambda}\eta_1 + ..., \qquad j_n = j_{n,0} + \frac{1}{\lambda}j_{n,1} + ..., \quad [4.72]$$

$$\Phi_e = \Phi_{e,0} + \Phi_{e,1} + ..., \qquad c_e = c_{e,0} + c_{e,1} + ..., \qquad j = j_0 + j_1 + ..., \quad [4.73]$$

$$N_- = N_{-,0} + N_{-,1} + ... \quad [4.74]$$

we can substitute into the dimensionless model. We can start by finding the leading order problem, followed by the first order correction term for the cell voltage.

4.3.1 Leading order for the microscopic electrode particle equations

Starting with the equations for the electrode particles, we can consider the leading order problem by substituting the expansions [4.71] - [4.74] into equations and boundary conditions [4.63] - [4.66]. This leads to:

$$\mathcal{Q}\frac{\partial(c_{a,0}+\frac{1}{\lambda}c_{a,1}+...)}{\partial t}=\frac{1}{r^2}\frac{\partial}{\partial r}\left[r^2D_a(c_{a,0}+\frac{1}{\lambda}c_{a,1}+...)\frac{\partial(c_{a,0}+\frac{1}{\lambda}c_{a,1}+...)}{\partial r}\right], \quad [4.75]$$

$$\frac{\partial(c_{a,0}+\frac{1}{\lambda}c_{a,1}+...)}{\partial r}\Big|_{r=0}=0, \quad [4.76]$$

$$\frac{\partial(c_{a,0}+\frac{1}{\lambda}c_{a,1}+...)}{\partial r}\Big|_{r=R_a(x)}=-\frac{\mathcal{Q}(j_{n,0}+\frac{1}{\lambda}j_{n,1}+...)}{D_a(c_{a,0}+\frac{1}{\lambda}c_{a,1}+...)}. \quad [4.77]$$

$$\mathcal{Q}\frac{\partial(c_{c,0}+\frac{1}{\lambda}c_{c,1}+...)}{\partial t}=\frac{1}{r^2}\frac{\partial}{\partial r}\left[r^2D_c(c_{c,0}+\frac{1}{\lambda}c_{c,1}+...)\frac{\partial(c_{c,0}+\frac{1}{\lambda}c_{c,1}+...)}{\partial r}\right], \quad [4.78]$$

$$\frac{\partial(c_{c,0}+\frac{1}{\lambda}c_{c,1}+...)}{\partial r}\Big|_{r=0}=0, \quad [4.79]$$

$$\frac{\partial(c_{c,0}+\frac{1}{\lambda}c_{c,1}+...)}{\partial r}\Big|_{r=R_c(x)}=-\frac{\mathcal{Q}(j_{n,0}+\frac{1}{\lambda}j_{n,1}+...)}{D_c(c_{c,0}+\frac{1}{\lambda}c_{c,1}+...)}. \quad [4.80]$$

Taking the limit $\lambda \to \infty$, we find the leading order terms for equations [4.63] - [4.66]:

$$\mathcal{Q}\frac{\partial c_{a,0}}{\partial t}=\frac{1}{r^2}\frac{\partial}{\partial r}\left[r^2D_a(c_{a,0})\frac{\partial c_{a,0}}{\partial r}\right], \quad [4.81]$$

$$\frac{\partial c_{a,0}}{\partial r}\Big|_{r=0}=0, \quad [4.82]$$

$$\frac{\partial c_{a,0}}{\partial r}\Big|_{r=R_a(x)}=-\frac{\mathcal{Q}j_{n,0}}{D_a(c_{a,0})}. \quad [4.83]$$

$$\mathcal{Q}\frac{\partial c_{c,0}}{\partial t}=\frac{1}{r^2}\frac{\partial}{\partial r}\left[r^2D_c(c_{c,0})\frac{\partial c_{c,0}}{\partial r}\right], \quad [4.84]$$

$$\frac{\partial c_{c,0}}{\partial r}\Big|_{r=0}=0, \quad [4.85]$$

$$\frac{\partial c_{c,0}}{\partial r}\Big|_{r=R_c(x)}=-\frac{\mathcal{Q}j_{n,0}}{D_c(c_{c,0})}. \quad [4.86]$$

4.3.2 Leading order for the macroscopic electrode equations

Similarly, substituting the expansions [4.71] - [4.74] into equations [4.54] - [4.57]

$$\frac{\partial(j_{a,0}+\frac{1}{\lambda}j_{a,1}+...)}{\partial x}=-b_{et}(j_{n,0}+\frac{1}{\lambda}j_{n,1}+...), \quad [4.87]$$

$$\frac{\partial(j_{c,0}+\frac{1}{\lambda}j_{c,1}+...)}{\partial x}=-b_{et}(j_{n,0}+\frac{1}{\lambda}j_{n,1}+...), \quad [4.88]$$

$$j_{a,0}+\frac{1}{\lambda}j_{a,1}+...=-\Theta\lambda\sigma\frac{\partial(\Phi_{a,0}+\frac{1}{\lambda}\Phi_{a,1})}{\partial x}, \quad [4.89]$$

$$j_{c,0}+\frac{1}{\lambda}j_{c,1}+...=-\Theta\lambda\sigma\frac{\partial(\Phi_{c,0}+\frac{1}{\lambda}\Phi_{c,1})}{\partial x}. \quad [4.90]$$

Rearranging equations [4.89] and [4.90]:

$$-\frac{1}{\lambda}\frac{1}{\Theta\sigma}(j_{a,0}+j_{a,1}+...) = \frac{\partial\Phi_{a,0}}{\partial x}+\frac{1}{\lambda}\frac{\partial\Phi_{a,1}}{\partial x}, \quad [4.91]$$

$$-\frac{1}{\lambda}\frac{1}{\Theta\sigma}(j_{c,0}+j_{c,1}+...) = \frac{\partial\Phi_{c,0}}{\partial x}+\frac{1}{\lambda}\frac{\partial\Phi_{c,1}}{\partial x}. \quad [4.92]$$

and then taking the limit $\lambda\to\infty$ we are left with:

$$\frac{\partial j_{a,0}}{\partial x}=-b_{et}j_{n,0}, \qquad \frac{\partial\Phi_{a,0}}{\partial x}=0, \quad [4.93]$$

$$\frac{\partial j_{c,0}}{\partial x}=-b_{et}j_{n,0}, \qquad \frac{\partial\Phi_{c,0}}{\partial x}=0. \quad [4.94]$$

and boundary and initial conditions:

$$j_{a,0}|_{x=L_1} = I(t), \qquad j_{a,0}|_{x=L_2}=0, \quad [4.95]$$

$$j_{c,0}|_{x=L_3} = 0, \qquad j_{c,0}|_{x=L_4}=I(t), \quad [4.96]$$

$$c_{a,0}|_{t=0} = c_{a,0}, \qquad c_{c,0}|_{t=0}=c_{c,0} \quad [4.97]$$

For equations [4.57]:

$$\frac{1}{\lambda}(\eta_{a,0}+\frac{1}{\lambda}\eta_{a,1}+...)=\Phi_{a,0}+\frac{1}{\lambda}\Phi_{a,1}+...-U_{eq,a}(c_{a,0}|_{r=R_a}+\frac{1}{\lambda}c_{a,1}|_{r=R_a}+...)-\frac{1}{\lambda}\Phi_{0,} \quad [4.98]$$

$$\frac{1}{\lambda}(\eta_{c,0}+\frac{1}{\lambda}\eta_{c,1}+...)=\Phi_{c,0}+\frac{1}{\lambda}\Phi_{c,1}+...-U_{eq,c}(c_{c,0}|_{r=R_c}+\frac{1}{\lambda}c_{c,1}|_{r=R_c}+...)-\frac{1}{\lambda}\Phi_{0,} \quad [4.99]$$

again taking the limit $\lambda\to\infty$ we are left with:

$$\Phi_{a,0}=U_{eq,a}(c_{a,0}|_{r=R_a}), \qquad \Phi_{c,0}=U_{eq,c}(c_{c,0}|_{r=R_c}) \quad [4.100]$$

4.3.3 Leading order for the electrolyte problem

We can apply a similar method to find the leading order problem for the equations in the electrolyte. Substituting the expansions [4.71] - [4.74] into equations [4.52] and [4.53] and boundary and initial conditions [4.60]a), [4.61] and [4.62] leads to:

$$\varepsilon_{el}\mathcal{N}\frac{\partial c_{e,0}}{\partial t}+\frac{\partial N_{-,0}}{\partial x}=0, \qquad N_{-,0}=-BD_e(c_{e,0})\frac{\partial c_{e,0}}{\partial x}-\Gamma(1-t^+)j_0 \quad [4.101]$$

$$\frac{\partial j_0}{\partial x}=b_{et}j_{n,0}, \qquad j_0=-PB\kappa\left(\frac{\partial \Phi_0}{\partial x}-\frac{2(1-t^+)}{c_{e,0}}\frac{\partial c_{e,0}}{\partial x}\right) \quad [4.102]$$

with boundary conditions and initial condition:

$$j_0|_{x=L_1} = 0 \qquad j_0|_{x=L_4}=0 \quad [4.103]$$

$$N_{-,0}|_{x=L_1} = 0 \qquad N_{-,0}|_{x=L_4}=0 \quad [4.104]$$

$$c_{e,0}|_{t=0} = 1. \quad [4.105]$$

Bringing these equations together we can give the leading order problem as:

$$\varepsilon_{el}\mathcal{N}\frac{\partial c_{e,0}}{\partial t}+\frac{\partial N_{-,0}}{\partial x}=0, \qquad N_{-,0}=-BD_e(c_{e,0})\frac{\partial c_{e,0}}{\partial x}-\Gamma(1-t^+)j_0 \quad [4.106]$$

$$\frac{\partial j_0}{\partial x}=b_{et}j_{n,0}, \qquad j_0=-PB\kappa\left(\frac{\partial \Phi_0}{\partial x}-\frac{2(1-t^+)}{c_{e,0}}\frac{\partial c_{e,0}}{\partial x}\right), \quad [4.107]$$

$$\frac{\partial j_{a,0}}{\partial x}=-b_{et}j_{n,0}, \qquad \frac{\partial \Phi_{a,0}}{\partial x}=0, \qquad \frac{\partial j_{c,0}}{\partial x}=-b_{et}j_{n,0}, \qquad \frac{\partial \Phi_{c,0}}{\partial x}=0. \quad [4.108]$$

$$\Phi_{a,0}=U_{eq,a}(c_{a,0}|_{r=R_a}), \qquad \Phi_{c,0}=U_{eq,c}(c_{c,0}|_{r=R_c}), \quad [4.109]$$

$$\mathcal{Q}\frac{\partial c_{a,0}}{\partial t}=\frac{1}{r^2}\frac{\partial}{\partial r}\left[r^2D_a(c_{a,0})\frac{\partial c_{a,0}}{\partial r}\right], \qquad \mathcal{Q}\frac{\partial c_{c,0}}{\partial t}=\frac{1}{r^2}\frac{\partial}{\partial r}\left[r^2D_c(c_{c,0})\frac{\partial c_{c,0}}{\partial r}\right]. \quad [4.110]$$

$$\frac{\partial c_{a,0}}{\partial r}\Big|_{r=0} = 0, \qquad \frac{\partial c_{a,0}}{\partial r}\Big|_{r=R_a(x)}=-\frac{\mathcal{Q}j_{n,0}}{D_a(c_{a,0})}, \quad [4.111]$$

$$\frac{\partial c_{c,0}}{\partial r}\Big|_{r=0} = 0, \qquad \frac{\partial c_{c,0}}{\partial r}\Big|_{r=R_c(x)}=-\frac{\mathcal{Q}j_{n,0}}{D_c(c_{c,0})}. \quad [4.112]$$

$$j_{a,0}|_{x=L_1}=I(t), \qquad j_{a,0}|_{x=L_2}=0, \qquad j_{c,0}|_{x=L_3}=0, \qquad j_{c,0}|_{x=L_4}=I(t), \quad [4.113]$$

$$c_{a,0}|_{t=0}=c_{a,0}, \qquad c_{c,0}|_{t=0}=c_{c,0}, \qquad V_{a,0}=\Phi_{a,0}|_{x=L_1}, \qquad V_{c,0}=\Phi_{c,0}|_{x=L_4}, \quad [4.114]$$

$$j_0|_{x=L_1} = 0, \quad j_0|_{x=L_4} = 0, \quad N_{-,0}|_{x=L_1} = 0, \quad N_{-,0}|_{x=L_4} = 0, \quad c_{e,0}|_{t=0} = 1. \tag{4.115}$$

We can note that equations [4.108](b) and (d) implies that $\Phi_{a,0}$ and $\Phi_{c,0}$ are independent of x and so are only functions of t so we can rewrite equations [4.109] in terms of $c_{s,0}$:

$$U_{eq,a}^{-1}(\Phi_{a,0}) = c_{a,0}|_{r=R_a(x)} = C_{0,a}(t), \tag{4.116}$$
$$U_{eq,c}^{-1}(\Phi_{c,0}) = c_{c,0}|_{r=R_c(x)} = C_{0,c}(t), \tag{4.117}$$

and therefore define the leading order terms for the cell voltage as:

$$V_{a,0} = \Phi_{a,0}(t) = U_{eq,a}(C_{a,0}(t)), \qquad V_{c,0} = \Phi_{c,0}(t) = U_{eq,c}(C_{c,0}(t)). \tag{4.118}$$

Integrating equations [4.108](a) and (c) between L_1 and L_2 and L_3 and L_4, respectively, and applying boundary conditions [4.113], we find:

$$-\int_{L_1}^{L_2} b_{et} j_{n,0} dx = j_{a,0}|_{x=L_2} - j_{a,0}|_{x=L_1} = -I(t), \tag{4.119}$$
$$-\int_{L_3}^{L_4} b_{et} j_{n,0} dx = j_{c,0}|_{x=L_4} - j_{c,0}|_{x=L_3} = I(t). \tag{4.120}$$

So we can rewrite equations [4.111](b) and [4.112](b) as:

$$\int_{L_1}^{L_2} b_{et} \frac{D_a(c_{a,0})}{\mathcal{Q}} \frac{\partial c_{a,0}}{\partial r}\Big|_{r=R_a(x)} dx = I(t) \tag{4.121}$$
$$\int_{L_3}^{L_4} b_{et} \frac{D_c(c_{c,0})}{\mathcal{Q}} \frac{\partial c_{c,0}}{\partial r}\Big|_{r=R_c(x)} dx = -I(t). \tag{4.122}$$

When considering a single-particle model, we can define the particle sizes in the given electrodes to be of a specific size and no longer dependent on x, namely R_a, R_c. Bringing the above equations together and applying this we find:

$$\mathcal{Q}\frac{\partial c_{a,0}}{\partial t} = \frac{1}{r^2}\frac{\partial}{\partial r}\left[r^2 D_a(c_{a,0})\frac{\partial c_{a,0}}{\partial r}\right], \qquad \mathcal{Q}\frac{\partial c_{c,0}}{\partial t} = \frac{1}{r^2}\frac{\partial}{\partial r}\left[r^2 D_c(c_{c,0})\frac{\partial c_{c,0}}{\partial r}\right]. \tag{4.123}$$

$$\frac{\partial c_{a,0}}{\partial r}\Big|_{r=0} = 0, \qquad D_a(c_{a,0})\frac{\partial c_{a,0}}{\partial r}\Big|_{r=R_a} = \frac{\mathcal{Q}I(t)}{\int_{L_1}^{L_2} b_{et} dx}, \tag{4.124}$$
$$\frac{\partial c_{c,0}}{\partial r}\Big|_{r=0} = 0, \qquad D_c(c_{c,0})\frac{\partial c_{c,0}}{\partial r}\Big|_{r=R_c} = -\frac{\mathcal{Q}I(t)}{\int_{L_3}^{L_4} b_{et} dx}. \tag{4.125}$$

$$c_{a,0}|_{t=0} = c_{0,a}, \quad c_{c,0}|_{t=0} = c_{0,c}, \quad V_{a,0} = U_{eq,a}(C_{a,0}(t)), \quad V_{c,0} = U_{eq,c}(C_{c,0}(t)) \tag{4.126}$$

which give conditions on $C_{a,0}$ and $C_{a,0}$.

Similarly, we can find an expression for $\eta_{a,0}$ and $\eta_{c,0}$ by applying expansions to [4.56]:
-2.0cm

$$j_{n,0}+\frac{1}{\lambda}j_{n,1}+...=\begin{cases}2\Upsilon(c_{e,0}(c_{a,0}|_{r=R_a}+\frac{1}{\lambda}c_{a,1}|_{r=R_a}+...))^{1/2} & \\ (1-c_{a,0}|_{r=R_a}-\frac{1}{\lambda}c_{a,1}|_{r=R_a}-...)^{1/2}\sinh\left(\frac{\eta_{a,0}+\frac{1}{\lambda}\eta_{a,1}+...}{2}\right) & \text{in} \quad L_1<x<L_2,\\ \quad 0 & \text{in} \quad L_2<x<L_3,\\ 2\Upsilon(c_{e,0}(c_{c,0}|_{r=R_c}+\frac{1}{\lambda}c_{c,1}|_{r=R_c}+...))^{1/2} & \\ (1-c_{c,0}|_{r=R_c}-\frac{1}{\lambda}c_{c,1}|_{r=R_c}-...)^{1/2}\sinh\left(\frac{\eta_{c,0}+\frac{1}{\lambda}\eta_{c,1}+...}{2}\right) & \text{in} \quad L_3<x<L_4.\end{cases} \quad [4.127]$$

again taking the limit $\lambda\to\infty$ we are left with:

$$j_{n,0}=\begin{cases}2\Upsilon(c_{e,0}c_{a,0}|_{r=R_a})^{1/2}(1-c_{a,0}|_{r=R_a})^{1/2}\sinh\left(\frac{\eta_{a,0}}{2}\right) & \text{in} \quad L_1<x<L_2,\\ \quad 0 & \text{in} \quad L_2<x<L_3,\\ 2\Upsilon(c_{e,0}c_{c,0}|_{r=R_c})^{1/2}(1-c_{c,0}|_{r=R_c})^{1/2}\sinh\left(\frac{\eta_{c,0}}{2}\right) & \text{in} \quad L_3<x<L_4.\end{cases} \quad [4.128]$$

Rearranging therefore leads to:

$$\eta_{a,0}=2\text{arcsinh}\left(\frac{j_{n,0}}{2\Upsilon(c_{e,0}c_{a,0}|_{r=R_a})^{1/2}(1-c_{a,0}|_{r=R_a})^{1/2}}\right), \quad [4.129]$$

$$\eta_{c,0}=2\text{arcsinh}\left(\frac{j_{n,0}}{2\Upsilon(c_{e,0}c_{c,0}|_{r=R_c})^{1/2}(1-c_{c,0}|_{r=R_c})^{1/2}}\right). \quad [4.130]$$

4.3.4 First order correction terms

Next we want to consider a first order correction term. Starting with the macroscopic electrode equations, we begin by substituting the expansion terms [4.71] - [4.74] into equations [4.54] - [4.57]:

$$\frac{\partial j_{a,0}}{\partial x}+\frac{1}{\lambda}\frac{\partial j_{a,1}}{\partial x}+...=-b_{et}(j_{n,0}+\frac{1}{\lambda}j_{n,1}+...), \quad [4.131]$$

$$\frac{\partial j_{c,0}}{\partial x}+\frac{1}{\lambda}\frac{\partial j_{c,1}}{\partial x}+...=-b_{et}(j_{n,0}+\frac{1}{\lambda}j_{n,1}+...), \quad [4.132]$$

$$j_{a,0}+\frac{1}{\lambda}j_{a,1}+...=-\Theta\lambda\sigma\left(\frac{\partial\Phi_{a,0}}{\partial x}+\frac{1}{\lambda}\frac{\partial\Phi_{a,1}}{\partial x}+...\right), \quad [4.133]$$

$$j_{c,0}+\frac{1}{\lambda}j_{c,1}+...=-\Theta\lambda\sigma\left(\frac{\partial\Phi_{c,0}}{\partial x}+\frac{1}{\lambda}\frac{\partial\Phi_{c,1}}{\partial x}+...\right), \quad [4.134]$$

This time we need to rearrange for the first order terms. For equations [4.133] and [4.134] we rearrange for the first order terms in Φ_s:

$$\frac{1}{\lambda}\frac{\partial \Phi_{a,1}}{\partial x} = \left(\frac{1}{-\Theta\lambda\sigma}\right)(j_{a,0} + \frac{1}{\lambda}j_{a,1} + ...) - \frac{\partial \Phi_{a,0}}{\partial x} - ... \quad [4.135]$$

$$\frac{1}{\lambda}\frac{\partial \Phi_{c,1}}{\partial x} = \left(\frac{1}{-\Theta\lambda\sigma}\right)(j_{c,0} + \frac{1}{\lambda}j_{c,1} + ...) - \frac{\partial \Phi_{c,0}}{\partial x} - ... \quad [4.136]$$

First we note we can neglect the $\Phi_{s,0}$ terms, due to [4.108](b) and [4.108](d), and therefore we can cancel some λ terms to give:

$$\frac{\partial \Phi_{a,1}}{\partial x} = \left(\frac{1}{-\Theta\sigma}\right)(j_{a,0} + \frac{1}{\lambda}j_{a,1} + ...) \quad [4.137]$$

$$\frac{\partial \Phi_{c,1}}{\partial x} = \left(\frac{1}{-\Theta\sigma}\right)(j_{c,0} + \frac{1}{\lambda}j_{c,1} + ...) \quad [4.138]$$

We now apply the limit $\lambda \to \infty$, simplifying to:

$$\frac{\partial \Phi_{a,1}}{\partial x} = -\frac{j_{a,0}}{\Theta\sigma}, \qquad \frac{\partial \Phi_{c,1}}{\partial x} = -\frac{j_{c,0}}{\Theta\sigma}. \quad [4.139]$$

Integrating, we can rewrite this as:

$$\Phi_{a,1} = -\int_x^{L_1} \frac{j_{a,0}}{\Theta\sigma}dx + \Phi_{a,1}|_{x=L_1}, \qquad \Phi_{a,1} = -\int_{L_4}^{x} \frac{j_{c,0}}{\Theta\sigma}dx + \Phi_{c,1}|_{x=L_4}. \quad [4.140]$$

Recall equation [4.70], we can apply the expansions [4.71] - [4.74] to give:

$$V_{a,0}(t) + \frac{1}{\lambda}V_{a,1}(t) = \Phi_{a,0}|_{x=L_1} + \frac{1}{\lambda}\Phi_{a,1}|_{x=L_1}, \quad [4.141]$$

$$V_{c,0}(t) + \frac{1}{\lambda}V_{c,1}(t) = \Phi_{c,0}|_{x=L_4} + \frac{1}{\lambda}\Phi_{c,1}|_{x=L_4}. \quad [4.142]$$

Using the leading order equations [4.114]c) and d), we remove the leading order terms and can find for first order:

$$V_{a,1}(t) = \Phi_{a,1}|_{x=L_1}, \qquad V_{c,1}(t) = \Phi_{c,1}|_{x=L_4}. \quad [4.143]$$

and substitute this into equations [4.140]a) and b) to give:

$$\Phi_{a,1} = -\int_x^{L_1} \frac{j_{a,0}}{\Theta\sigma} dx + V_{a,1}, \qquad \Phi_{a,1} = -\int_{L_4}^{x} \frac{j_{c,0}}{\Theta\sigma} dx + V_{c,1}. \qquad [4.144]$$

Similarly, we apply a similar method for equations [4.131] and [4.132]; we can cancel the leading order terms using equations [4.108] a) and c):

$$\frac{1}{\lambda}\frac{\partial j_{a,1}}{\partial x} = -b_{et}(\frac{1}{\lambda} j_{n,1}), \qquad [4.145]$$

$$\frac{1}{\lambda}\frac{\partial j_{c,1}}{\partial x} = -b_{et}(\frac{1}{\lambda} j_{n,1}), \qquad [4.146]$$

and therefore cancelling the λ terms we can find in terms of $j_{s,1}$ as:

$$\frac{\partial j_{a,1}}{\partial x} = -b_{et} j_{n,1}, \qquad \frac{\partial j_{c,1}}{\partial x} = -b_{et} j_{n,1}, \qquad [4.147]$$

and therefore integrating leads to:

$$[j_{a,1}]_{L_1}^{L_2} = -\int_{L_1}^{L_2} b_{et} j_{n,1} dx, \qquad [j_{c,1}]_{L_3}^{L_4} = -\int_{L_3}^{L_4} b_{et} j_{n,0} dx. \qquad [4.148]$$

Applying the expansions [4.71] - [4.74] to the boundary conditions [4.58] and [4.59]:

$$j_{a,0}|_{x=L_1} + \frac{1}{\lambda} j_{a,1}|_{x=L_1} = I(t), \qquad j_{a,0}|_{x=L_2} + \frac{1}{\lambda} j_{a,1}|_{x=L_2} = 0, \qquad [4.149]$$

$$j_{c,0}|_{x=L_3} + \frac{1}{\lambda} j_{c,1}|_{x=L_3} = 0, \qquad j_{c,0}|_{x=L_4} + \frac{1}{\lambda} j_{c,1}|_{x=L_4} = I(t), \qquad [4.150]$$

and using the leading order boundary conditions [4.113] to simplify, we find the first order terms for the boundary conditions as:

$$j_{a,1}|_{x=L_1} = 0, \qquad j_{a,1}|_{x=L_2} = 0, \qquad [4.151]$$

$$j_{c,1}|_{x=L_3} = 0, \qquad j_{c,1}|_{x=L_4} = 0, \qquad [4.152]$$

Applying these boundary conditions to [4.148] leads to:

$$\int_{L_1}^{L_2} b_{et} j_{n,1} dx = 0, \qquad \int_{L_3}^{L_4} b_{et} j_{n,1} dx = 0, \qquad [4.153]$$

giving conditions on $j_{n,1}$.

These conditions on $j_{n,1}$, together with the first order correction terms for $V_{a,1}$ and $V_{c,1}$ and the leading order models discussed in Sections 4.3.1 and 4.3.2 for the microscopic and macroscopic electrode equations, respectively, and in Section 4.3.3 for the electrolyte combine to give the single-particle model.

4.4 Summary

In this chapter, we have introduced the concept of single-particle models and how they can be used to simplify a full-cell, multi-scale model such as the Doyle-Fuller-Newman (DFN) model. We described the setup of an electrochemical cell and laid out the DFN model to describe the charge transport occurring in each phase of the cell. We non-dimensionalised the model, making notes on the significance of some parameters.

We then went on to follow the derivation in (Richardson et al., 2020) to apply asymptotic analysis on the model to derive the leading order model and the first order correction terms. It was shown in (Richardson et al., 2020) that this single-particle model shows good agreement with the DFN model for various electrode chemistries.

This model could be applied to various current areas of lithium-ion battery research. The study of the electrode surface reactions could help with insight into electrode degradation and electrolyte decomposition; this single-particle model could help simplify the reaction equations resulting from the Butler-Volmer kinetics. Modelling the heat generation and energy losses occurring in different parts of the electrochemical cell was presented in (Richardson and Korotkin, 2021); the derivation of an equivalent single-particle model could prove valuable. Similarly, this model could set a pathway to the study of much more complex electrode structures by helping to reduce the complexity of the model, such as for a lithium iron phosphate cathode where the lithium transport in the electrode particles occurs in two phases (Richardson et al., 2021).

5 The Double Layer

In Chapter 2, we looked at a model for a dilute electrolyte where we made the assumption of charge neutrality, where the concentrations of the negative and positive ions are equal throughout the electrolyte. However, we find that at the interface between an electrode and the electrolyte, the behaviour of the ions is different from that in the bulk electrolyte. Each species of ion has a tendency to be attracted to the electrode of the opposite charge, therefore at each interface one species of ion will be much more abundant than the other and so we have a net separation of charge (Chapman, 1913). This layer is referred to as the electrical double layer, and for most typical electrolyte concentrations it has a width of a few nanometres (Newman and Thomas-Alyea, 2004).

5.1 The Structure of the Double Layer

The double layer consists of two layers; the layer closest to the electrode is called the Stern layer, and consists of a thin, dense layer of ions with the opposite charge of the electrode, these ions are said to be specifically adsorbed (Bard and Faulkner, 2001). This layer is bounded by two planes, termed the inner and outer Helmholtz planes. The inner Helmholtz plane is defined by the position of the centres of the specifically adsorbed ions, while the outer Helmholtz plane is by the centres of the closest location (to the electrode) of the solvated ions; these ions are surrounded by solvent molecules which restricts how close they can get (Newman and Thomas-Alyea, 2004). Moving away from the electrode, the ions are now able to move more freely; this layer is often termed the diffuse layer (Stillinger and Kirkwood, 1960) and extends out to the bulk solution. The potential in the Stern layer is thought to decrease linearly, while it then decreases exponentially throughout the diffuse layer as it tends to 0 in the bulk electrolyte (Mortimer, 2008). This is shown in Figure 11, where the structure of the double layer adjacent to a negative electrode is shown in a), while b) shows a plot of the potential through the double layer, with the dashed lines representing the boundaries of the Stern layer and diffuse layer.

The thickness of the double layer is dependent on the concentration of the electrolyte (Newman and Thomas-Alyea, 2004), with higher concentrations leading to narrower double layers, often due to the compression of the Stern layer with higher concentrations (Brown, Goel and Abbas, 2016). It has also been shown that the ion

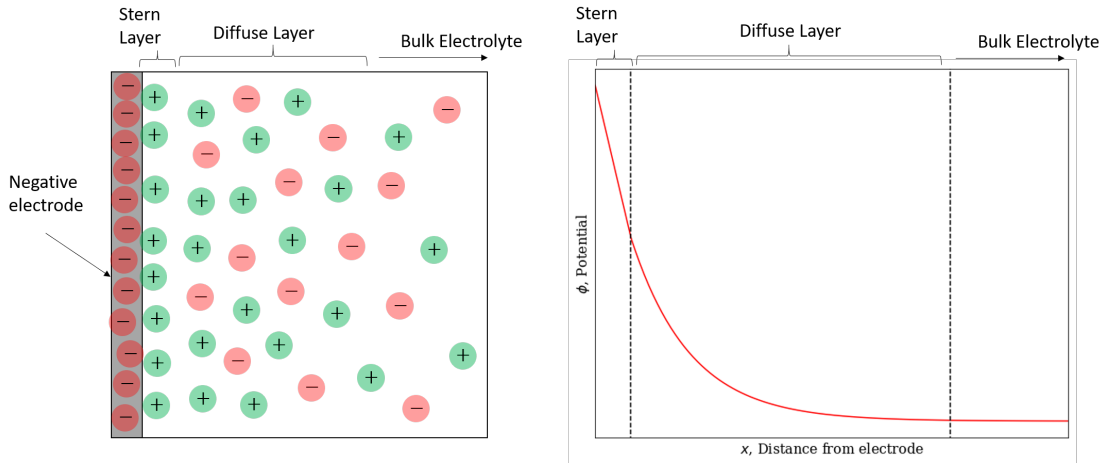

Figure 11: a) A representation of the structure of the electrical double layer adjacent to a negative electrode. b) A plot showing the potential across the electrical double layer, with the dashed lines showing the boundaries between each layer. The potential in the Stern layer decreases linearly, while it decreases exponentially in the diffuse layer.

size can have an effect on its thickness; larger ion sizes can lead to thicker double layers (Bohinc, Kralj-Iglič and Iglič, 2001). The thickness of the double layer will then affect the rate of processes occurring at the electrode (Bard and Faulkner, 2001).

5.1.1 Chapter Outline

Here, we will briefly set out the aims of this chapter and how we will go about studying them. We wish to investigate the double layer, the region adjacent to an electrode. To do this we are going to focus on the redox reactions that occur on the electrode surface, where the lithium ions (de)-intercalate into the electrode structure.

The aim of this chapter is to investigate the occurrence of electron tunnelling within the double layer and its effect on the rates of the redox reactions and therefore on cell performance. At the beginning of this work, we theorised that electron tunnelling out of the electrode could make the electrons more readily available for the reactions, leading to an increase in reaction rate and therefore faster lithium intercalation. During the charge cycle, this would lead to faster charge times which is a favourable feature for a rechargeable battery. On the other hand, during discharge, faster lithium intercalation into the cathode would lead to the battery not lasting as long, an unfavourable property. We proposed that if the electron tunnelling could

be studied and more controlled, it could be utilised to gain more favourable charge times while mitigating its effects during discharge. Ultimately, we found our prediction was incorrect and instead found results that suggested the electron tunnelling leads to a reduction of cell performance without any significant benefits. Here, we discuss how we went about investigating this behaviour and the conclusions we came to.

To look at these reactions we split our focus into two parts, an electron tunnelling model and the Butler-Volmer equation. In Section 5.2, we will introduce the Schrödinger equation and derive a general matrix equation to solve it for any given potential barrier. This gives us values for the transmission coefficient, which is a measure of the probability of an electron successfully tunnelling through the barrier. We apply this to the potential barriers found in the double layer for specific cathode materials (lithium iron phosphate and lithium cobalt oxide) at multiple times throughout the discharge process resulting in plots of transmission coefficient against state of discharge (SoD). We then repeat this for different discharge voltages.

In Section 5.3 we now focus on the redox reaction rates by introducing the Butler-Volmer equation and applying this equation to the same materials as in Section 5.2 throughout the discharge process and again we repeat for various discharge voltages. This gives us curves for current density against state of discharge.

In Section 5.4 we bring our results for the transmission coefficients and current densities together and plot them together as functions of state of discharge. This allows us to compare the results and investigate any possible relations between them. In this Section, we then discuss the results individually and together and then explore possible consequences and further research ideas.

5.2 Quantum Tunnelling

We will now shift focus to specifically consider the movement of electrons as lithium ions (de)-intercalate with the electrodes. During the (dis)-charge of an electrochemical cell, a lithium ion travels from one electrode to the other through the electrolyte while an electron travels in the same direction but through the external circuit. The lithium ion will now absorb the electron, but to do this the electron will need to travel against the potential difference that is across the cell. In this chapter, we

review the process of electrons tunnelling through a potential barrier to discuss whether this is a possible mechanism that occurs in an electrochemical cell.

In this section, we will briefly set out the background to quantum tunnelling and introduce how the Schrödinger equation can be used to describe the process of tunnelling compared to a classical mechanics situation. We will begin with the example of a single potential barrier to demonstrate the process, before extending the problem to multiple barriers and then formulating a general model that can be used to solve the problem of tunnelling through any potential curve. This model will then be used later in the chapter to study electron tunnelling through a potential barrier at the electrode-electrolyte interface in an electrochemical cell.

5.2.1 Background

Consider an object with energy E approaching a potential barrier with potential V; in classical mechanics we could interpret this as a ball of mass m travelling at velocity $\mathbf{v}$ towards a ramp of height h, as shown in blue in Figure 12.

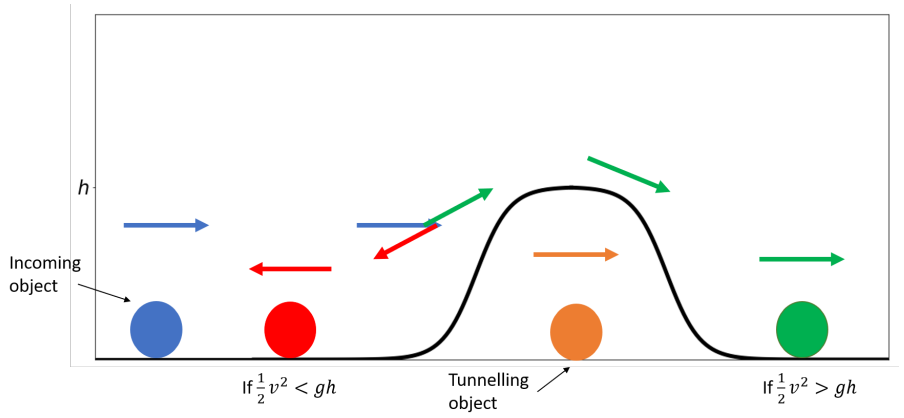

Figure 12: An image demonstrating the difference between classical mechanics (where the incoming ball (blue) will either have enough energy to overcome the ramp (green) or will roll back down if not (red)) and quantum mechanics (where the ball has a possibility of tunnelling through the ramp (orange)).

In this example, the ball would have kinetic energy $E_K = \frac{1}{2}mv^2$ and would require gravitational potential energy of $E_G = mgh$ to make it over the ramp. Therefore, if $\frac{1}{2}v^2 \geq gh$ holds, we would expect the ball to follow the path shown in green in Figure 12 and make it to the other side. If $\frac{1}{2}v^2 < gh$, the ball will not have enough energy to reach the top of the ramp and therefore we would expect it to be impossible for it

to be found beyond the barrier, instead following the path shown in red in Figure 12.

Quantum mechanics treats the situation from a different perspective. When considering objects at the subatomic level, such as electrons, the concept of tunnelling is introduced. The idea behind tunnelling suggests that even if $\frac{1}{2}v^2 < gh$, there is still a small probability that the object will be found on the other side of the potential barrier as it has tunnelled through via the path shown in orange in Figure 12.

Quantum tunnelling has been applied to many research areas, one of the earliest being the Gamow model which describes the process of alpha decay where the alpha particle is confined to a potential well. George Gamow linked the probability of the alpha particle tunnelling through the potential well to the half-life of the decay process (Griffiths, 2006). The most well-known example is the Scanning Tunnelling Microscope. Developed by Gerd Binnig and Heinrich Rohrer, the instrument uses electron tunnelling to produce 3D images of material surfaces with resolutions such that individual atoms can be precisely imaged (Binnig and Rohrer, 1986).

5.2.2 The Schrödinger Equation

In quantum mechanics, the concept of wave-particle duality describes how matter can exhibit properties of both particles and waves. The idea was proposed in 1924 by Louis de Broglie and was later demonstrated experimentally when diffraction patterns of a beam of electrons were observed. Diffraction is the spreading out of a wave (Thomson and Reid, 1927), for example a water wave, as it passes through a narrow gap.

This leads to the concept of a wave function, which describes the wave in space as it evolves. This evolution can be described by the Schrödinger Equation, one of the fundamental equations of quantum mechanics (Schrödinger, 1926); it has been described as being analogous to Newton's 2nd Law. The time-independent Schrödinger equation can be stated as follows:

$$-\frac{\bar{h}^2}{2m}\frac{d^2\Psi}{dx^2} + V_{bar}(x)\Psi(x) = E_q\Psi(x), \qquad [5.1]$$

where $\bar{h}$ is the reduced Planck's constant given by $h/2\pi$, m is the mass of the particle, x represents the direction of motion, E_q is the energy of the quantum

particle, in this case electrons measured in electron volts, eV, and $V_{bar}(x)$ is the function of the potential barrier.

Solving the Schrödinger Equation: Following (Giffiths, 2004) we solve the Schrödinger equation. We can rewrite [5.1] as:

$$-\frac{\bar{h}^2}{2m}\frac{d^2\Psi}{dx^2} + \big[V_{bar}(x) - E_q\big]\Psi(x) = 0, \qquad [5.2]$$

We will be considering multiple small regions where $V_{bar}(x)$ is constant, and applying Schrödinger's equation to each region, so we can write the characteristic equation as:

$$-\frac{\bar{h}^2}{2m}k^2 + (V_{bar} - E_q) = 0, \qquad [5.3]$$

and we can now consider the cases where $E_q > V_{bar}$ and $E_q < V_{bar}$.

1. **When** $E_q > V_{bar}$:

   The characteristic equation [5.3] has complex roots, so a general solution can be written as:

   $$\Psi(x) = A_1 e^{ikx} + B_1 e^{-ikx} \quad \textbf{where} \quad k = \frac{\sqrt{2m(E_q - V_{bar})}}{\bar{h}}. \qquad [5.4]$$

2. **When** $E_q < V_{bar}$:

   The characteristic equation [5.3] has real roots, so a general solution can be written as:

   $$\Psi(x) = A_2 e^{kx} + B_2 e^{-kx} \quad \textbf{where} \quad k = \frac{\sqrt{2m(V_{bar} - E_q)}}{\bar{h}}. \qquad [5.5]$$

Here $\Psi(x)$ can be defined as the wave function and k the wave number. The wave function describes the system at each point in space; the e^{ikx} term represents the portion of the wave travelling in the positive direction, while the e^{-ikx} term represents the portion of the wave travelling in the negative direction. The coefficients A_i and $B_i, i = 1, 2$ are complex-valued constants defining the magnitude of each of these parts of the wave.

Boundary Conditions: In the following examples, it will be necessary to solve the Schrödinger equation within multiple regions where the potential relative to the electron's energy will vary. This will give us a solution in each region that we can combine to create one 'smooth' solution. This will require imposing conditions on the boundaries, $x = b_i, i = 1, 2, ...$, of each region so that the solutions and their derivatives are continuous:

$$\begin{aligned}
\Psi_1|_{x=b_1} &= \Psi_2|_{x=b_1} \qquad \left.\frac{d\Psi_1}{dx}\right|_{x=b_1} = \left.\frac{d\Psi_2}{dx}\right|_{x=b_1}, \\
\Psi_2|_{x=b_2} &= \Psi_3|_{x=b_2} \qquad \left.\frac{d\Psi_2}{dx}\right|_{x=b_2} = \left.\frac{d\Psi_3}{dx}\right|_{x=b_2}, \\
&\vdots \qquad\qquad\qquad\qquad \vdots \\
\Psi_i|_{x=b_i} &= \Psi_{i+1}|_{x=b_i} \qquad \left.\frac{d\Psi_i}{dx}\right|_{x=b_i} = \left.\frac{d\Psi_{i+1}}{dx}\right|_{x=b_i}.
\end{aligned} \tag{5.6}$$

5.2.3 A Single Barrier

Consider a single potential barrier of width $2a$ centred around the origin of potential $V_{bar,0}$, where $V_{bar,0} > E_q$, as shown in Figure 13. This potential can be split into 3 regions and be defined as:

$$V_{bar}(x) = \begin{cases} 0 & \text{for } x < -a, \\ V_{bar,0} & \text{for } -a > x > a, \\ 0 & \text{for } x > a. \end{cases} \tag{5.7}$$

Using the general solutions to the Schrödinger equation above, we can define the wave functions, Ψ_i, and wave numbers, k_i, for each region. In the regions on either side of the potential barrier we have $E_q > V_{bar,0}$, so we can use the form of [5.4], whereas in the region containing the barrier we have $E_q < V_{bar,0}$ so we use the form of [5.5]. This leads to:

$$\Psi_1(x) = A_1 e^{ik_1 x} + B_1 e^{-ik_1 x}, \tag{5.8}$$

$$\Psi_2(x) = A_2 e^{k_2 x} + B_2 e^{-k_2 x}, \tag{5.9}$$

$$\Psi_3(x) = A_3 e^{ik_1 x} + B_3 e^{-ik_1 x}, \tag{5.10}$$

where:

$$k_1 = \frac{\sqrt{2mE_q}}{\bar{h}}, \qquad k_2 = \frac{\sqrt{2m(V_{bar,0} - E_q)}}{\bar{h}}. \tag{5.11}$$

We can start by considering the B_3 term; this term represents the reflected portion in the region beyond the barrier, however as the potential remains 0 in this region, this term is physically impossible to be non-zero. Therefore, we can set $B_3 = 0$.

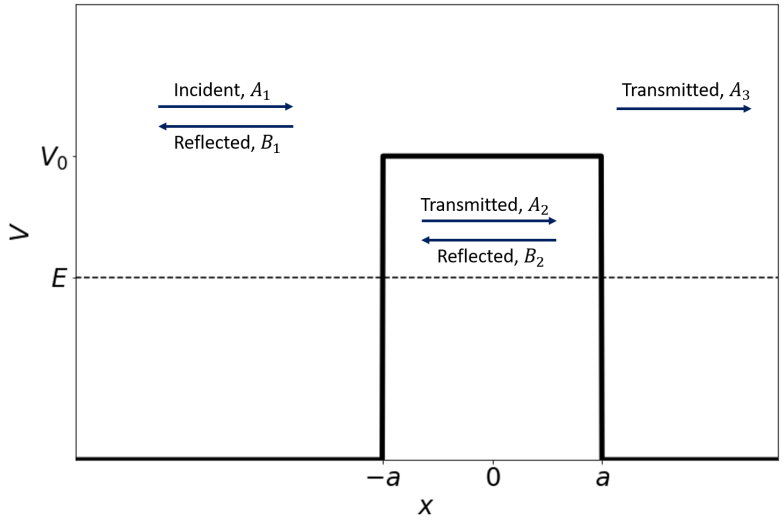

Figure 13: A representation of the potential barrier used for a single barrier example. The arrows demonstrate the direction and magnitude of the incident, reflected and transmitted portions of the wave in each region. The dotted line shows the energy of the incoming wave relative to the potential barrier ($E_q < V_{bar,0}$)

We then proceed by formulating the relevant boundary conditions at $x = -a$ and $x = a$, using the form of [5.6]:

$$\Psi_1|_{x=-a} = \Psi_2|_{x=-a} \qquad \left.\frac{d\Psi_1}{dx}\right|_{x=-a} = \left.\frac{d\Psi_2}{dx}\right|_{x=-a} \tag{5.12}$$

$$\Psi_2|_{x=a} = \Psi_3|_{x=a} \qquad \left.\frac{d\Psi_2}{dx}\right|_{x=a} = \left.\frac{d\Psi_3}{dx}\right|_{x=a} \tag{5.13}$$

Applying these conditions results in the following equations:

$$-B_1 e^{ik_1 a} + A_2 e^{-k_2 a} + B_2 e^{k_2 a} = A_1 e^{-ik_1 a} \tag{5.14}$$

$$ik_1 B_1 e^{ik_1 a} + k_2(A_2 e^{-k_2 a} - B_2 e^{k_2 a}) = ik_1 A_1 e^{-ik_1 a} \tag{5.15}$$

$$A_2 e^{k_2 a} + B_2 e^{-k_2 a} - A_3 e^{ik_1 a} = 0 \tag{5.16}$$

$$k_2 A_2 e^{k_2 a} - k_2 B_2 e^{-k_2 a} - ik_1 A_3 e^{ik_1 a} = 0 \tag{5.17}$$

The Transmission Coefficient: We are interested in solving for A_3 as this represents the transmitted portion of the wave that made it beyond the barrier. This will allow us to find an expression for the transmission coefficient, T^{coeff}, which gives a measure of the probability that the particle, in this case an electron, will successfully tunnel through the barrier and be found on the other side. The transmission coefficient is the ratio of magnitude of the transmitted wave relative to the initial incoming wave, given by:

$$T^{coeff} = \frac{|A_3|^2}{|A_1|^2} \tag{5.18}$$

We begin by combining equations [5.14] and [5.15] to find:

$$2A_1 e^{-ik_1 a} = A_2 e^{-k_2 a}\left(1 - \frac{ik_2}{k_1}\right) + B_2 e^{k_2 a}\left(1 + \frac{ik_2}{k_1}\right) \tag{5.19}$$

while combining equations [5.16] and [5.17] results in:

$$A_2 e^{k_2 a} = \frac{1}{2} A_3 e^{ik_1 a}\left(1 + \frac{ik_1}{k_2}\right) \tag{5.20}$$

$$B_2 e^{-k_2 a} = \frac{1}{2} A_3 e^{ik_1 a}\left(1 - \frac{ik_1}{k_2}\right) \tag{5.21}$$

Substituting equations [5.20] and [5.21] into [5.19] we find:

$$A_1 e^{-ik_1 a} = \frac{1}{4} A_3 e^{ik_1 a}\left[\left(1 + \frac{ik_1}{k_2}\right)\left(1 - \frac{ik_2}{k_1}\right)e^{-2k_2 a} + \left(1 - \frac{ik_1}{k_2}\right)\left(1 + \frac{ik_2}{k_1}\right)e^{2k_2 a}\right], \tag{5.22}$$

then rearranging we can finally write:

$$A_1 e^{-ik_1 a} = A_3 e^{ik_1 a}\left[\cosh(2k_2 a) + \frac{i({k_2}^2 - {k_1}^2)}{2k_1 k_2}\sinh(2k_2 a)\right], \tag{5.23}$$

where we have made use of:

$$\sinh(x) = \frac{e^x - e^{-x}}{2} \qquad \cosh(x) = \frac{e^x + e^{-x}}{2}. \tag{5.24}$$

Using [5.18] we can therefore state the transmission coefficient as:

$$T^{coeff} = \frac{1}{\cosh(2k_2 a) + \frac{i({k_2}^2 - {k_1}^2)}{2k_1 k_2}\sinh(2k_2 a)}, \tag{5.25}$$

As expected we can see that as a, half the width of the barrier, increases, T^{coeff} will decrease drastically, and therefore the probability of tunnelling is much lower.

The Wave Function: To find a numerical solution for the wave function, the most efficient method is to form a matrix equation; this method can then be generalised for any number of barriers, which will be discussed later. To proceed, we can also consider the A_1 term, which is the coefficient of the initial incoming wave. We are interested in the other coefficients relative to the incoming wave, so we can simplify by setting $A_1 = 1$.

From equations [5.14] - [5.17], we can form the following matrix equation:

$$\begin{bmatrix} -e^{ik_1a} & e^{-k_2a} & e^{k_2a} & 0 \\ ik_1e^{ik_1a} & k_2e^{-k_2a} & -k_2e^{k_2a} & 0 \\ 0 & e^{k_2a} & e^{-k_2a} & -e^{ik_1a} \\ 0 & k_2e^{k_2a} & -k_2e^{-k_2a} & -ik_1e^{ik_1a} \end{bmatrix} \begin{bmatrix} B_1 \\ A_2 \\ B_2 \\ A_3 \end{bmatrix} = \begin{bmatrix} e^{-ik_1a} \\ ik_1e^{-ik_1a} \\ 0 \\ 0 \end{bmatrix}$$

which can be solved numerically for the coefficients B_1, A_2, B_2 and A_3. With these solutions, we can substitute back into equations [5.8] - [5.10] and then plot Ψ against x; the resulting solution is shown in Figure 14.

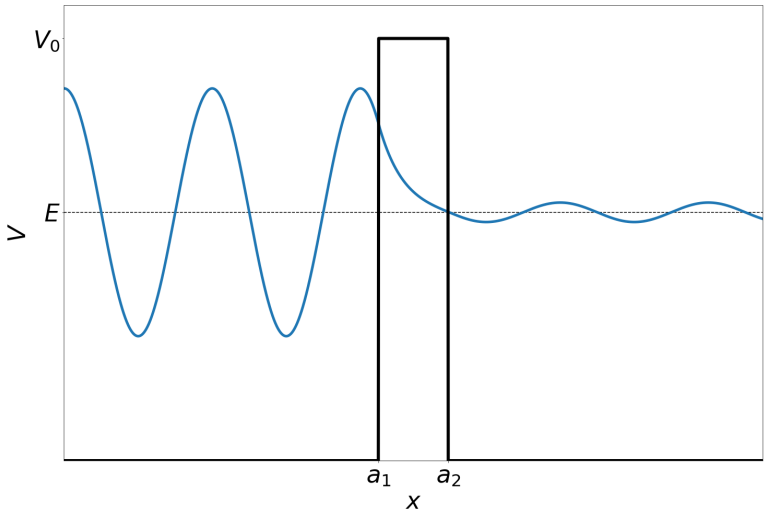

Figure 14: A plot showing the solutions to the Schrödinger equation for the wave function, Ψ in each region. The solution acts as an oscillating wave before the barrier, as it enters the potential barrier the solution decays exponentially before showing oscillating behaviour again beyond the barrier, this time with a smaller amplitude.

5.2.4 Extending to a Double Barrier

We can extend this idea to a barrier, where the potential varies slightly across the barrier, which we can treat as two separate barriers adjacent to each other. Consider a potential barrier, as shown in Figure 15, positioned between $x = a_1$ and $x = a_3$, with a change in potential at $x = a_2$, such that $V_{bar}(x)$ can be defined as:

$$V_{bar}(x) = \begin{cases} 0 & \text{for } x < a_1 \\ V_{bar,0} & \text{for } a_1 > x > a_2 \\ V_{bar,1} & \text{for } a_2 > x > a_3 \\ 0 & \text{for } x > a_3 \end{cases}$$

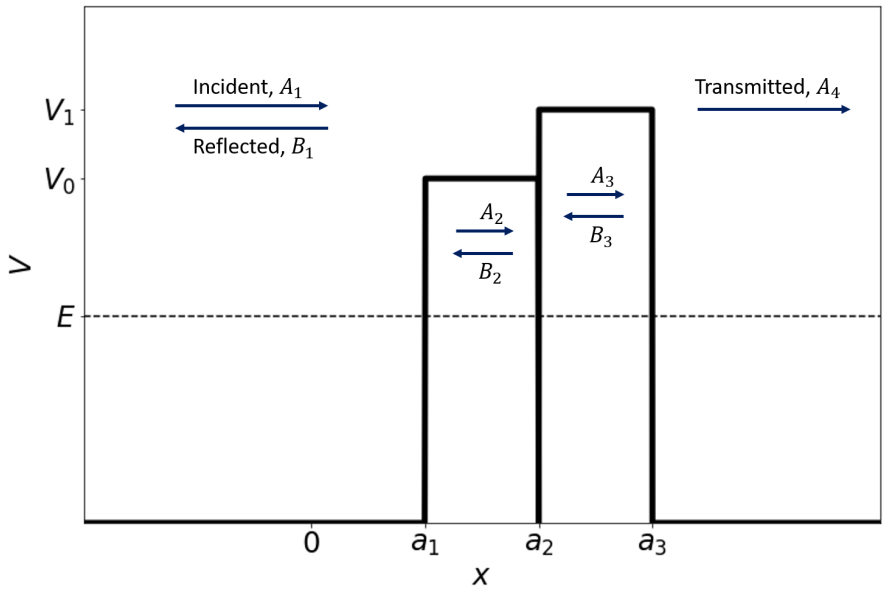

Figure 15: A representation of the potential barrier used for a double barrier example. The arrows demonstrate the direction and magnitude of the incident, reflected and transmitted portions of the wave in each region. The dotted line shows the energy of the incoming wave relative to the potential barrier ($E_{eq} < V_{bar,0}$, $E_{eq} < V_{bar,1}$)

As before we can define the wave functions and wave numbers, where we have set reflection coefficient of Ψ_4 to 0 and normalised the coefficient of the incoming wave to 1:

$$\Psi_1(x) = e^{ik_1x} + B_1e^{-ik_1x} \quad [5.26]$$

$$\Psi_2(x) = A_2e^{k_2x} + B_2e^{-k_2x} \quad [5.27]$$

$$\Psi_3(x) = A_3e^{k_3x} + B_3e^{-k_3x} \quad [5.28]$$

$$\Psi_4(x) = A_4e^{ik_1x} \quad [5.29]$$

where:

$$k_1 = \frac{\sqrt{2mE_q}}{\bar{h}} \qquad k_2 = \frac{\sqrt{2m(V_{bar,0} - E_q)}}{\bar{h}} \qquad k_3 = \frac{\sqrt{2m(V_{bar,1} - E_q)}}{\bar{h}} \quad [5.30]$$

Similarly, we can apply boundary conditions [5.6] to each boundaries at $x = a_1$, $x = a_2$ and $x = a_3$:

$$\Psi_1|_{x=a_1} = \Psi_2|_{x=a_1} \qquad \left.\frac{d\Psi_1}{dx}\right|_{x=a_1} = \left.\frac{d\Psi_2}{dx}\right|_{x=a_1} \quad [5.31]$$

$$\Psi_2|_{x=a_2} = \Psi_3|_{x=a_2} \qquad \left.\frac{d\Psi_2}{dx}\right|_{x=a_2} = \left.\frac{d\Psi_3}{dx}\right|_{x=a_2} \quad [5.32]$$

$$\Psi_3|_{x=a_3} = \Psi_4|_{x=a_3} \qquad \left.\frac{d\Psi_3}{dx}\right|_{x=a_3} = \left.\frac{d\Psi_4}{dx}\right|_{x=a_3} \quad [5.33]$$

This can lead to the matrix equation :

$$\begin{bmatrix} -e^{-ik_1a_1} & e^{k_2a_1} & e^{-k_2a_1} & 0 & 0 & 0 \\ ik_1e^{-ik_1a_1} & k_2e^{k_2a_1} & -k_2e^{-k_2a_1} & 0 & 0 & 0 \\ 0 & e^{k_2a_2} & e^{-k_2a_2} & -e^{k_3a_2} & -e^{-k_3a_2} & 0 \\ 0 & k_2e^{k_2a_2} & -k_2e^{-k_2a_2} & -k_3e^{k_3a_2} & k_3e^{-k_3a_2} & 0 \\ 0 & 0 & 0 & e^{k_3a_3} & e^{-k_3a_3} & -e^{ik_1a_3} \\ 0 & 0 & 0 & k_3e^{k_3a_3} & -k_3e^{-k_3a_3} & -ik_1e^{ik_1a_3} \end{bmatrix} \begin{bmatrix} B_1 \\ A_2 \\ B_2 \\ A_3 \\ B_3 \\ A_4 \end{bmatrix} = \begin{bmatrix} e^{ik_1a_1} \\ ik_1e^{ik_1a_1} \\ 0 \\ 0 \\ 0 \\ 0 \end{bmatrix}$$

The solution to the matrix equation for the wave function is shown in Figure 16.

In both Figure 14 and Figure 16, we can note the change in the behaviour of the oscillating wave as it enters the potential barrier. The solution decays exponentially within before showing oscillating behaviour again on the other side, only now with a much smaller amplitude. This amplitude relative to the incoming wave is directly related to the transmission coefficient. The solutions shown here are simply a background as we build up to more complex potential curves in the next section.

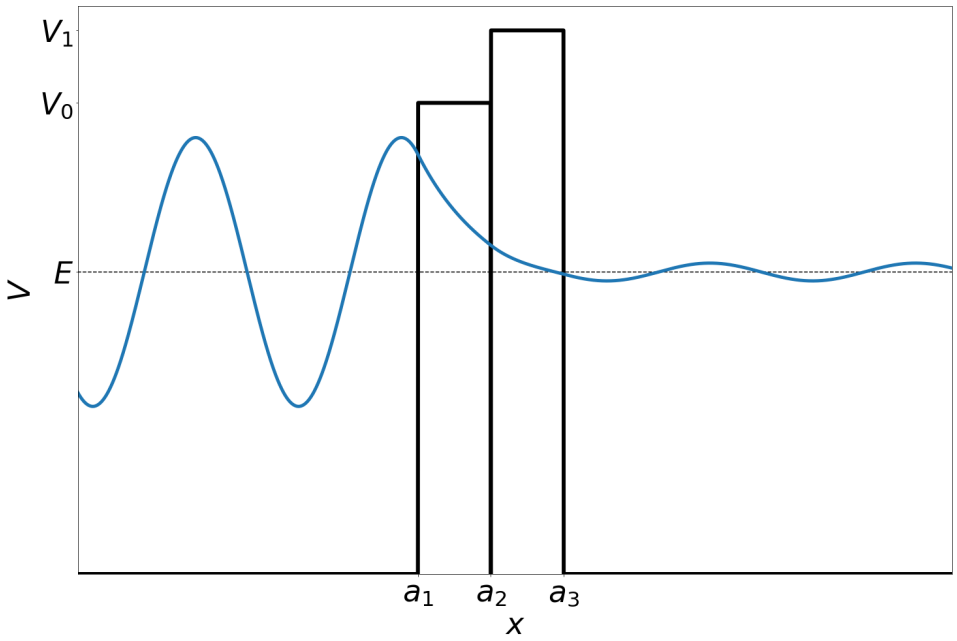

Figure 16: A plot showing the solutions to the Schrödinger equation for the wave function, Ψ in each region for a double potential barrier. The solution acts as an oscillating wave before the barrier; as it enters the potential barrier the solution decays before showing oscillating behaviour again beyond the barrier.

5.2.5 A General Matrix Equation

This problem can be extended to account for tunnelling through a potential curve. For any given curve, we can simplify the potential to multiple barriers each with constant potential.

Consider a potential curve, which we divide into N potential barriers, where we denote each with potential $V_{bar}(x) = V_{bar,i},\ i = 0, \ldots N+1$. Here $V_{bar,0}$ and $V_{bar,N+1}$ denote the potential on either of side of the barrier, so we will take $V_{bar,0} = V_{bar,N+1} = 0$. This leads to splitting the wave function, Ψ, into $N+2$ equations:

$$\Psi_0 = A_0 e^{ik_0 x} + B_0 e^{-ik_0 x} \quad [5.34]$$

$$\Psi_1 = A_1 e^{k_1 x} + B_1 e^{-k_1 x} \quad [5.35]$$

$$\vdots \qquad \vdots \quad [5.36]$$

$$\Psi_N = A_N e^{k_N x} + B_N e^{-k_N x} \quad [5.37]$$

$$\Psi_{N+1} = A_{N+1} e^{ik_0 x} + B_{N+1} e^{-ik_0 x} \quad [5.38]$$

where:

$$k_0 = \frac{\sqrt{2mE_q}}{\bar{h}} \quad [5.39]$$

$$k_1 = \frac{\sqrt{2m(V_{bar,1} - E_q)}}{\bar{h}} \quad [5.40]$$

$$\vdots \qquad \vdots \quad [5.41]$$

$$k_N = \frac{\sqrt{2m(V_{bar,N} - E_q)}}{\bar{h}} \quad [5.42]$$

This leads to a $(2N+1) \times (2N+1)$ matrix of the form:

$$
\begin{bmatrix}
-e^{-ik_0a_0} & e^{k_1a_0} & e^{-k_1a_0} & 0 & 0 & 0 & \cdots & \cdots & 0 \\
ik_0e^{-ik_0a_0} & k_1e^{k_1a_0} & -k_1e^{-k_1a_0} & 0 & 0 & 0 & \cdots & \cdots & 0 \\
0 & e^{k_1a_1} & e^{-k_1a_1} & -e^{k_2a_1} & -e^{-k_2a_1} & 0 & \cdots & \cdots & 0 \\
0 & k_1e^{k_1a_1} & -k_1e^{-k_1a_1} & -k_2e^{k_2a_1} & k_2e^{-k_2a_1} & 0 & \cdots & \cdots & 0 \\
\vdots & \ddots & & & \ddots & & & & \vdots \\
\vdots & & \ddots & & & \ddots & & & \vdots \\
\vdots & & & \ddots & & & \ddots & & \vdots \\
\vdots & & & & \ddots & & & \ddots & \vdots \\
0 & \cdots & \cdots & 0 & e^{k_{N-1}a_{N-1}} & e^{-k_{N-1}a_{N-1}} & -e^{k_Na_{N-1}} & -e^{-k_Na_{N-1}} & 0 \\
0 & \cdots & \cdots & 0 & k_{N-1}e^{k_{N-1}a_{N-1}} & -k_{N-1}e^{-k_{N-1}a_{N-1}} & -k_Ne^{k_Na_{N-1}} & k_Ne^{-k_Na_{N-1}} & 0 \\
0 & \cdots & \cdots & 0 & \cdots & 0 & e^{k_Na_N} & e^{-k_Na_N} & -e^{ik_1a_N} \\
0 & \cdots & \cdots & 0 & \cdots & 0 & k_Ne^{k_Na_N} & -k_Ne^{-k_Na_N} & -ik_1e^{ik_1a_N}
\end{bmatrix}
\begin{bmatrix}
B_0 \\ A_1 \\ B_1 \\ A_2 \\ \vdots \\ B_{N-1} \\ A_N \\ B_N \\ A_{N+1}
\end{bmatrix}
=
\begin{bmatrix}
e^{ik_0a_0} \\ ik_0e^{ik_0a_0} \\ 0 \\ 0 \\ \vdots \\ 0 \\ 0 \\ 0 \\ 0
\end{bmatrix}
$$

We have represented these solutions by using various different equations for the potential curve; these are shown in Figure 17. The next step is to link this model for electron tunnelling to lithium-ion batteries; we will apply it to potential curves adjacent to electrodes for specific electrode materials, to study this in relation to reaction rates on the surface of the electrodes.

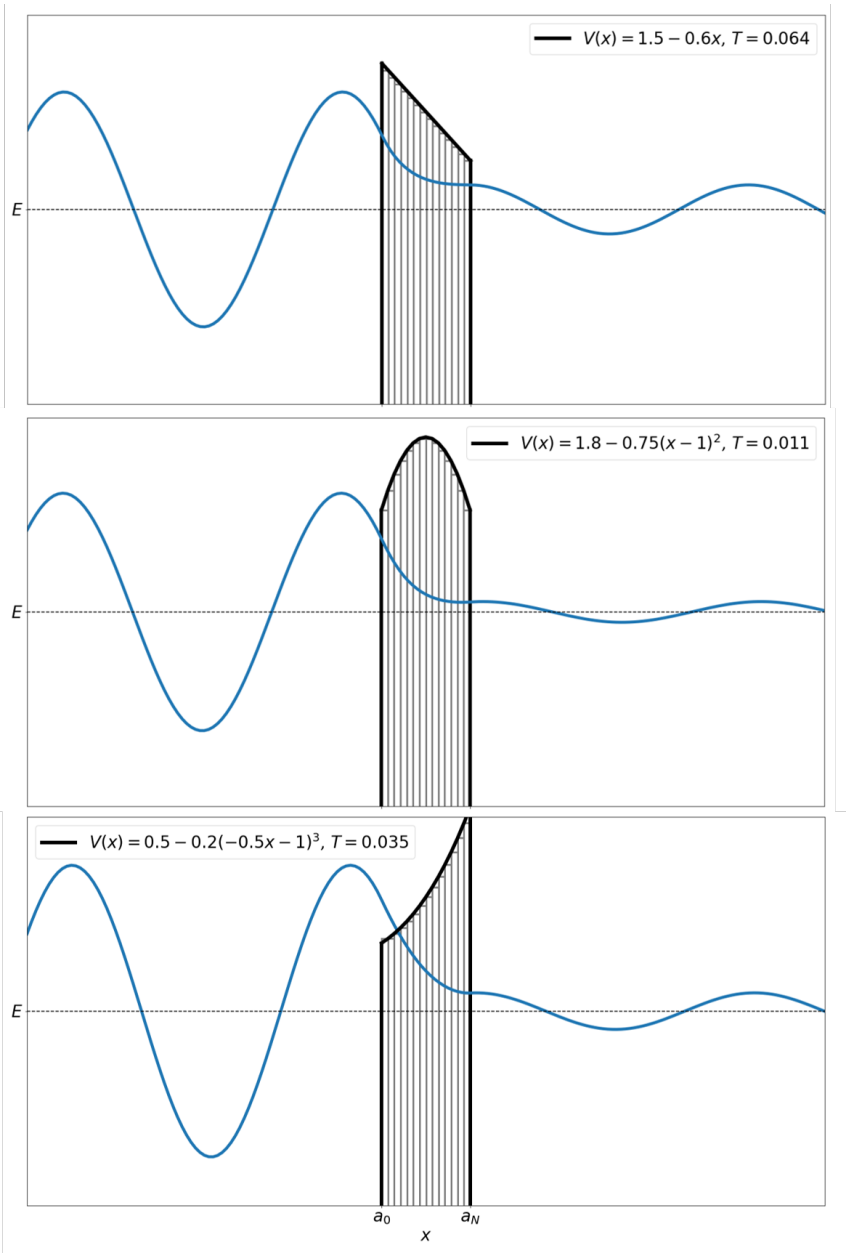

Figure 17: A selection of plots demonstrating the solutions for the wave function, Ψ, for the tunnelling problem with different potential curve barriers.

5.3 The Butler-Volmer Equation

In order to study the reactions occurring at the electrode-electrolyte interface, we first consider the Butler-Volmer equation, which describes the kinetics of these oxidation and reduction reactions. The equation was named after John Alfred Butler and Max Volmer; Butler published his work in 1924, which was then expanded upon by Volmer in 1930 (Dickinson and Wain, 2020).

The Butler-Volmer equation is a fundamental equation that can be derived from the laws of thermodynamics; it gives the relationship between the electrode current density, j, and the electrode potential E and can be stated as:

$$j = j_a - j_c = j_0 \left[\exp\left(\frac{\alpha_a z F (E - E_{eq})}{R_g T} \right) - \exp\left(- \frac{\alpha_c z F (E - E_{eq})}{R_g T} \right) \right], \quad [5.43]$$

where j_0 is the exchange-current density: a measure of the current-density when the electrode is at equilibrium and therefore $E - E_{eq} = 0$. As in previous sections, F, R_g and T are Faraday's constant, the universal gas constant and temperature respectively and z is the number of electrons transferred in the reaction.

Here we introduce the overpotential, a measure of the deviation between the applied electrode potential and the equilibrium potential:

$$\eta = E - E_{eq}. \quad [5.44]$$

This deviation is scaled by the dimensionless values $\alpha_s, s = a, c$ which are the anodic and cathodic charge transfer coefficients which describe the deviation for the anodic and cathodic reactions respectively.

We are interested in the reactions occurring at the electrode-electrolyte interface, so we can rewrite equation [5.44] as:

$$\eta = (E_{solid} - E_{electrolyte}) - E_{eq}, \quad [5.45]$$

where we have rewritten the potential difference across the electrode-electrolyte interface as the difference between the potential in the electrode and the potential in the electrolyte.

5.3.1 Equilibrium Potentials

During the discharge process, the lithium ions are inserted into the cathode material, during this process the equilibrium potential (also be referred to as the open-circuit potential) varies as more lithium is inserted. These equilibrium potential curves can also vary depending on the chemistry of the chosen material.

Here, we will specifically consider iron-phosphate (Li_xFePO_4, commonly referred to as LFP) and cobalt dioxide (Li_xCoO_2), Figure 18 shows the equilibrium potential for these materials against the state of discharge (SoD) where $x = \frac{c_s}{c_{s,max}}$ is the concentration of lithium that has been inserted into the material relative to the maximum concentration that the material can hold, therefore the SoDs for the graphs in Figure 18 vary between $0 - 1$.

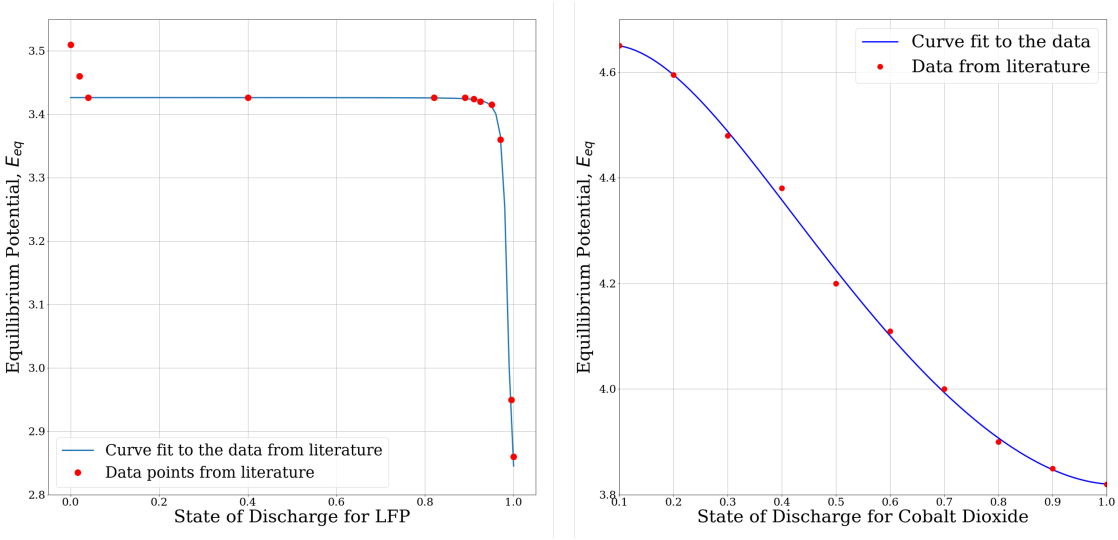

Figure 18: The equilibrium potentials as functions of state of discharge for LFP and cobalt dioxide cathodes. a) For LFP, the data points and curve fit equation come from (Srinivasan and Newman, 2004), given by equation [5.46] b) For cobalt dioxide, the data points come from (Fuller et al., 1994b) and we found a curve fit, given in equation [5.47].

The equilibrium potential of LFP has a wide region where the potential doesn't fluctuate with changing state of discharge, with narrow regions of steep decrease either side, as shown in Figure 18a). This shape indicates two phases occurring during the discharge process (Srinivasan and Newman, 2004).

The data points in the literature were found by solving a discharge model to specific states of discharge and then a curve was found to fit this data. The equation for

this curve was found to be:

$$E_{eq} = 3.11456 + 4.43879\tan^{-1}\Big[-71.7352x + 70.8534\Big] \\ -4.2403\tan^{-1}\Big[-68.5605x + 67.7301\Big]. \qquad [5.46]$$

The cobalt dioxide material shows a much more variable equilibrium potential with state of discharge, the data points were plotted from simulation results in the literature (Fuller et al., 1994b) and then we applied a curve to fit the data. The equation for this curve is given by:

$$E_{eq} = 1.92303x^5 - 6.84711x^4 + 10.4457x^3 \\ -7.32774x^2 + 1.01491x + 4.61167. \qquad [5.47]$$

For both of these equations $x = \frac{c_s}{c_{s,max}}$ is the state of discharge.

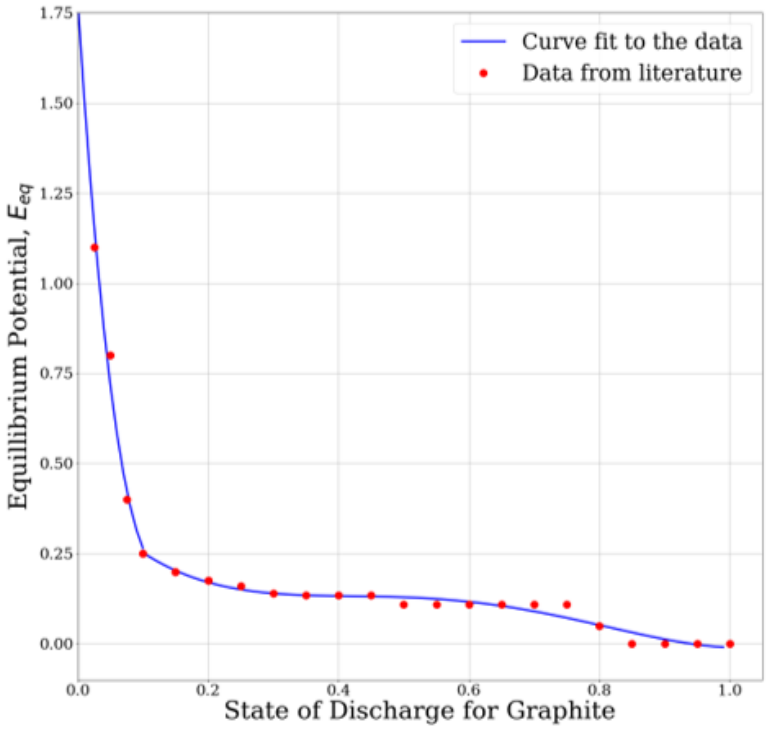

Figure 19: The equilibrium potential as a function of state of discharge for a graphite anode. The data points come from (Allart, Montaru and Gualous, 2018), we found a curve fit, given by equation [5.48].

Similarly, we can consider an anode material, here we will look at graphite LiC_6. During the discharge of the cell, the lithium ions are de-intercalated from the

graphite structure. We can again look at the equilibrium potential against the state of discharge, which is shown in Figure 19.

The equilibrium potential curve for graphite shows a steep change when the amount of intercalated lithium is low ($x < 0.1$) and then shows less variance across higher amounts of lithium, with only small step decreases.

The data points were taken from the literature, where a half-cell was charged and discharged using pulse of current to take measurements of the equilibrium potential at specific states of discharge (Allart, Montaru and Gualous, 2018).

In order to fit a curve to these we opted to split the data into the regions of $x < 0.1$ and $x \geq 0.1$ and find separate curves for each region with the intention that the curves will provide a better fit to the data. The equation for these curves was found to be:

$$E_{eq} = \begin{cases} -558.067x^4 - 144.702x^3 + 154.006x^2 - 28.5837x + 1.78385 & \text{for } x < 0.1, \\ 3.16145x^4 - 7.78813x^3 + 6.45701x^2 - 2.26234x + 0.422129 & \text{for } x \geq 0.1. \end{cases} \quad [5.48]$$

Now consider a full cell composing of graphite anode and a cobalt dioxide cathode. During the discharge process the lithium is oxidised into Li^+ ions which de-intercalate from the graphite material C_6 and are then inserted into the cathode material CoO_2. During this reaction the cobalt ions are reduced from the Co^{4+} form to the Co^{3+} form.

Using the equations for the respective electrode equilibrium potential we can therefore plot the total cell equilibrium potential against the cell discharge, as shown in Figure 20. Note that both Figure 18 and Figure 19 show the equilibrium potential as a function of discharge for the given electrode, with $SoD = 0$ meaning the electrode has been depleted of lithium ions and $SoD = 1$ meaning the electrode has maximum concentration of lithium ions. We are considering the discharge of a full cell, therefore we are interested in change in equilibrium potential of the cathode material as lithium ions are intercalated (so SoD changes from 0 to 1). Conversely, for the anode material, we are interested in change in equilibrium potential of the

as lithium ions are de-intercalated (so SoD changes from 1 to 0).

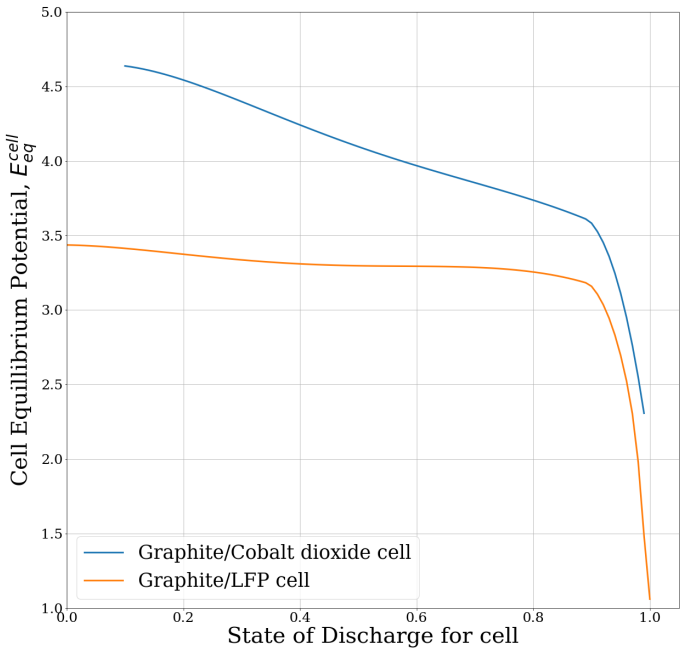

Figure 20: The full cell equilibrium potentials as functions of state of discharge for graphite/LFP and graphite/cobalt dioxide cells. We used the data from (Srinivasan and Newman, 2004) for LFP, the data from (Fuller et al., 1994b) for cobalt dioxide and (Allart, Montaru and Gualous, 2018) for graphite.

The equilibrium potentials of both the graphite/cobalt dioxide and graphite/LFP cells show similar-shaped curves due to the steep change in equilibrium potential of graphite when it is almost fully depleted. The significant difference in these curves comes from cobalt dioxide displaying more consistent variance over the discharge process, while LFP has a very steep curve when almost fully intercalated. This combination leads to the graphite/cobalt dioxide cell displaying much more variance for $SoD < 0.9$ compared to the graphite/LFP cell and overall the equilibrium potential of the graphite/cobalt dioxide remains higher across the entire discharge process.

A cobalt dioxide cathode can have problems with fully de-intercalating lithium ions compared to LFP. This is known as the depth of discharge of the electrode and is one factor that effects their cycle life. This can be seen in Figure 20 where the

graphite/cobalt dioxide cell never reaches $SoD < 0.1$.

5.3.2 Derivation of the Butler-Volmer Equation

To start we will first consider transition-state theory, which studies reactions rates by considering the energy states the reactants go through to become the products.

Consider a reaction where reactants R_1, R_2 combine to form a product P:

$$R_1 + R_2 \rightarrow P. \tag{5.49}$$

In order for this reaction to occur both R_1 and R_2 must go through some physical changes, such as the breaking of bonds. In order to break these bonds energy is required, therefore this energy is absorbed from the surroundings.

This means there is some intermediate state for these reactants before they go on to form the products of the reaction. This intermediate state is know as the transition state; it is a high-energy state that all reactants must reach in order to then go on to complete the reaction and form the product. The formation of such bonds releases energy into the surroundings, therefore if a given mole of reactants is able to absorb enough energy to reach the transition state the reaction will always complete and the products will always be formed.

This high-energy can therefore be linked to an activation energy, called the Gibbs energy of activation ΔG_A, for this reaction to occur as shown in Figure 21, where we can see the potential energy changes occurring throughout the reaction for both an endothermic (left) and an exothermic (right) reaction. An endothermic reaction is one that overall requires more energy for the breaking of the bonds than is released by the formation of the new bonds, whereas exothermic reaction is the opposite and overall gives a release of energy due to the products having a lower energy state than the reactants.

We are particularly interested in the Gibbs energy of activation for a given reaction as we can link this to the rate of the reaction. Following (Newman and Thomas-Alyea, 2004), the Gibbs energy of activation can be defined as:

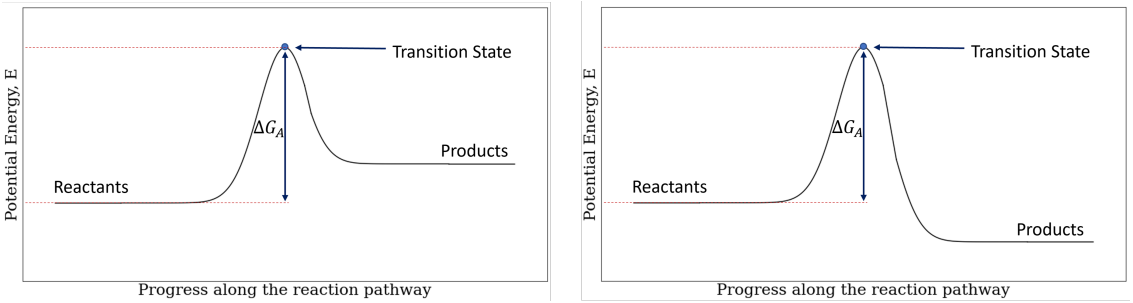

Figure 21: The potential energy changes over the reaction pathway for a) an endothermic reaction and b) an exothermic reaction.

$$\Delta G_{A,a} = \Delta G^0_{A,a} + C_a \quad [5.50]$$

$$\Delta G_{A,c} = \Delta G^0_{A,c} + C_c, \quad [5.51]$$

where we have denoted the Gibbs energy of activation as $\Delta G_{A,a}, \Delta G_{A,c}$ to indicate the these activation energies may be different for the oxidation and reduction reactions.

In these equations, $\Delta G^0_{A,s}$ are the Gibbs energy of activation for the reaction when there is no applied potential difference and C_s is some change in energy due to an applied potential difference, which we will consider below.

Consider an electrochemical reaction occurring at an electrode boundary, where z electrons are transferred and O_x and R_{ed} are the oxidised and reduced species respectively:

$$O_x + ze^- \rightleftharpoons R_{ed}. \quad [5.52]$$

This equation can be written as two half-equations, describing the anodic and cathodic reactions:

Anodic (Oxidation):

$$R_{ed} \rightarrow O_x + ze^-. \quad [5.53]$$

Cathodic (Reduction):

$$O_x + ze^- \rightarrow R_{ed}. \quad [5.54]$$

If the transition state for this reaction is similar to the reduced species R_{ed}, it is reactant-like for the anodic reaction and product-like for the cathodic reaction. This leads to the applied potential difference, $\Delta\phi$ having a large impact on the cathodic reaction by increasing the amount of energy required by $zF\Delta\phi$. This will also little impact on the anodic reaction, meaning the Gibbs energy of activation is independent of this potential difference.

Conversely, if the transition state is similar to the oxidised species, it is reactant-like for the cathodic reaction and therefore will have little impact on activation energy. The transition state is product like for the anodic reaction and so the potential difference will have a large impact but this time will contribute work done and therefore reduce the Gibbs energy of activation by $zF\Delta\phi$.

This phenomenon can be accounted for by introducing charge transfer coefficients α_s, where $s = a, c$ for the anodic and cathodic reactions. These charge transfer coefficients give a measure of how reactant-like or product-like the transition state is, and therefore the extent of which $\Delta\phi$ affects the Gibbs energy of activation.

In an actual reaction, the charge transfer coefficients will not be strictly 0 or 1 and therefore the Gibbs energy of activation equations can instead be summarised as;

$$\Delta G_{A,a} = \Delta G^0_{A,a} - \alpha_a zF\Delta\phi, \quad [5.55]$$

$$\Delta G_{A,c} = \Delta G^0_{A,c} + \alpha_c zF\Delta\phi. \quad [5.56]$$

In single-step reactions, the values for the charge transfer coefficients can typically be defined as $\alpha_a + \alpha_c = 1$ and so can often be written in the equations as simply α and $1 - \alpha$ (Dickinson and Wain, 2020).

We are interested in studying the rate of reactions [5.53] and [5.54] where these Gibbs energies of activation can be applied. The rates of these equations occurring, denoted r_a, r_c, is proportional to the concentrations of species R_{ed} and O_x respectively and so can be written as:

$$r_a = k_a[R_{ed}], \quad [5.57]$$

$$r_c = k_c[Ox_x]. \quad [5.58]$$

where we have introduced k_a and k_c as the rate constants of each reaction.

These can then be written in terms of the anodic and cathodic current densities j_a and j_c which are these rates multiplied by the amount of charge transferred, which can be given by the number of electrons transferred multiplied by Faraday's constant, zF:

$$j_a = zFk_a[R_{ed}], \tag{5.59}$$

$$j_c = zFk_c[Ox_x]. \tag{5.60}$$

Next, we introduce the Eyring equation, which relates rate constants to the Gibbs energy of activation, G_A, of the reaction:

$$k = \frac{\kappa k_B T}{h} \exp\left(\frac{-\Delta G_A}{R_g T}\right), \tag{5.61}$$

where κ is the transmission coefficient, k_B is Boltzmann's constant and h is Planck's constant. For simplicity we can combine these constants and denote them as B_a and B_c, phenomenological constants that depend on the chemical reaction being studied. We can define our rate constants as:

$$k_a = B_a \exp\left(\frac{-\Delta G_{A,a}}{R_g T}\right), \tag{5.62}$$

$$k_c = B_c \exp\left(\frac{-\Delta G_{A,c}}{R_g T}\right), \tag{5.63}$$

where we have denoted the Gibbs energy of activation as $\Delta G_{A,a}, \Delta G_{A,c}$ to indicate the these activation energies may be different for the oxidation and reduction reactions.

Substituting the rate constants into [5.59] and [5.60] to give:

$$j_a = zFB_a[R_{ed}] \exp\left(\frac{-\Delta G_{A,a}}{R_g T}\right), \tag{5.64}$$

$$j_c = zFB_c[Ox_x] \exp\left(\frac{-\Delta G_{A,c}}{R_g T}\right), \tag{5.65}$$

and then substituting in the Gibbs energies of activation from equations [5.55] and [5.56]:

$$j_a = zFB_a[R_{ed}] \quad \exp\left(\frac{-\Delta G^0_{A,a}}{R_g T}\right) \exp\left(\frac{\alpha_a z F \Delta\phi}{R_g T}\right), \tag{5.66}$$

$$j_c = zFB_c[O_x] \quad \exp\left(\frac{-\Delta G^0_{A,c}}{R_g T}\right) \exp\left(\frac{-\alpha_c z F \Delta\phi}{R_g T}\right). \tag{5.67}$$

If we consider the reaction is at equilibrium, there is no net flow of current and there is a balance between the reaction rates of the oxidation and reduction reactions $r_a = r_c$. Recalling equations [5.57], [5.58], we can therefore write:

$$B_a[R_{ed}] \exp\left(\frac{-\Delta G^0_{A,a}}{R_g T}\right) \exp = B_c[O_x]\left(\frac{-\Delta G^0_{A,c}}{R_g T}\right), \tag{5.68}$$

which leads us to denote:

$$j_0 = zFB_a[R_{ed}] \exp\left(\frac{-\Delta G^0_{A,a}}{R_g T}\right) = zFB_c[O_x] \exp\left(\frac{-\Delta G^0_{A,c}}{R_g T}\right), \tag{5.69}$$

and therefore the current densities can be simplified to:

$$j_a = j_0 \exp\left(\frac{\alpha_a z F \Delta\phi}{R_g T}\right), \tag{5.70}$$

$$j_c = j_0 \exp\left(\frac{-\alpha_c z F \Delta\phi}{R_g T}\right). \tag{5.71}$$

Now we can consider the potential difference $\Delta\phi$. If we denote the electrode potential of the cell while a current is being produced as E and the electrode potential of the cell at equilibrium as E_{eq}, we can therefore replace the $\Delta\phi$ term by $E - E_{eq}$:

$$j_a = j_0 \exp\left(\frac{\alpha_a z F (E - E_{eq})}{R_g T}\right), \tag{5.72}$$

$$j_c = j_0 \exp\left(\frac{-\alpha_c z F (E - E_{eq})}{R_g T}\right). \tag{5.73}$$

Finally, recall the net current density at the electrode is simply $j_a - j_c$, which leads to the Butler-Volmer equation:

$$j = j_0 \left[\exp\left(\frac{\alpha_a z F (E - E_{eq})}{R_g T}\right) - \exp\left(\frac{-\alpha_c z F (E - E_{eq})}{R_g T}\right)\right]. \tag{5.74}$$

For a single-step reactions we can replace $\alpha_c = \alpha$ and $\alpha_a = 1 - \alpha$, and using equation [5.44] we can replace $E - E_{eq} = \eta$ to give:

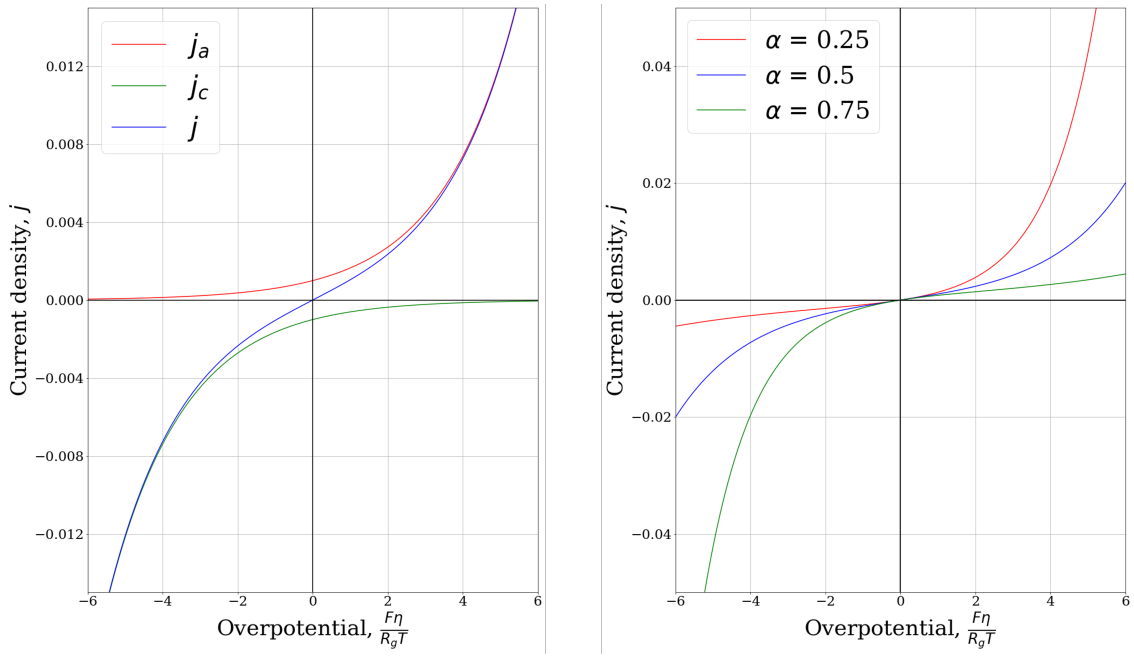

Figure 22: a) Current density, split into anodic and cathodic current densities, as a function of overpotential (which has been scaled by $\frac{F}{R_gT}$). b) Current density as a function of overpotential (scaled by $\frac{F}{R_gT}$) for values of $\alpha = 0.25, 0.5, 0.75$.

$$j = j_0 \left[\exp\left(\frac{(1-\alpha)zF\eta}{R_gT}\right) - \exp\left(\frac{-\alpha zF\eta}{R_gT}\right)\right]. \qquad [5.75]$$

To show how the individual current densities in equations [5.72] and [5.73] depend on overpotential and therefore contribute to the total current density, Figure 22 a) shows a plot of these current densities against overpotential with both anodic and cathodic transfer coefficients $\alpha = 0.5$ while Figure 22 b) shows a plot of how current density j varies for a few different values of α.

5.3.3 Tafel Approximation

The Butler-Volmer equation can be simplified when considering high-magnitude overpotentials; this leads us to an equation known as the Tafel equation.
For large positive overpotentials (typically $\eta > 0.12V$) the 2nd term in equation [5.75] becomes significantly smaller than the 1st term and so can be neglected. This leaves us with:

$$j = j_0 \exp\left(\frac{(1-\alpha)zF\eta}{R_gT}\right). \qquad [5.76]$$

Similarly, for negative overpotentials ($\eta < -0.12V$) the 1st term in equation [5.75] can be neglected when compared to the 2nd term, leaving us with:

$$j = -j_0 \exp\left(\frac{-\alpha z F \eta}{R_g T}\right). \qquad [5.77]$$

5.4 Results and Discussion

We are now ready to compare the current densities calculated using the Butler-Volmer equation [5.75] to the transmission coefficients found by applying the electron tunnelling model discussed in Section 5.2. We will be considering cathodes made up of lithium iron phosphate (LFP, $LiFePO_6$) and lithium cobalt dioxide ($LiCoO_2$). In both cases we assume the charge transfer coefficient $\alpha = 0.5$.

For the cobalt dioxide cathode, we begin by solving the Butler-Volmer equation for the cathodic current density using equation [5.73] for different states of discharge; we use [5.47] for the values of the equilibrium potential, E_{eq}.

We then applied the electron tunnelling model discussed in Section 5.2.5 to set up a matrix for the wave function. We split the potential barrier adjacent to the electrode into 10 sections, each with constant potential, and solved for the transmission and refection coefficients for each section of the potential barrier. We calculated the value of the final transmission coefficient relative to the incoming wave, which represents the proportion of the wave that was able to transmit through the entire potential barrier and therefore gives a measure of the probability of the electron tunnelling through the barrier. This process was repeated over the discharge process, using the values of the equilibrium potential from equation [5.47]. Note, as we are considering a cathode material, the system discharging means the insertion of lithium ions into the electrode material.

The plots in Figure 23 show the resulting transmission coefficients (in red) and the current densities (in blue) as a function of state of discharge. We repeated this for different values of E, the potential difference between the electrode and electrolyte across the surface, the plots show values between $E = 3.6 - 4.2V$: a) $E = 4.2V$, b) $E = 4V$, c) $E = 3.8V$ and d) $E = 3.6V$. These values were chosen as they fall within the usual discharges voltages for cobalt dioxide (Wang, 2014).

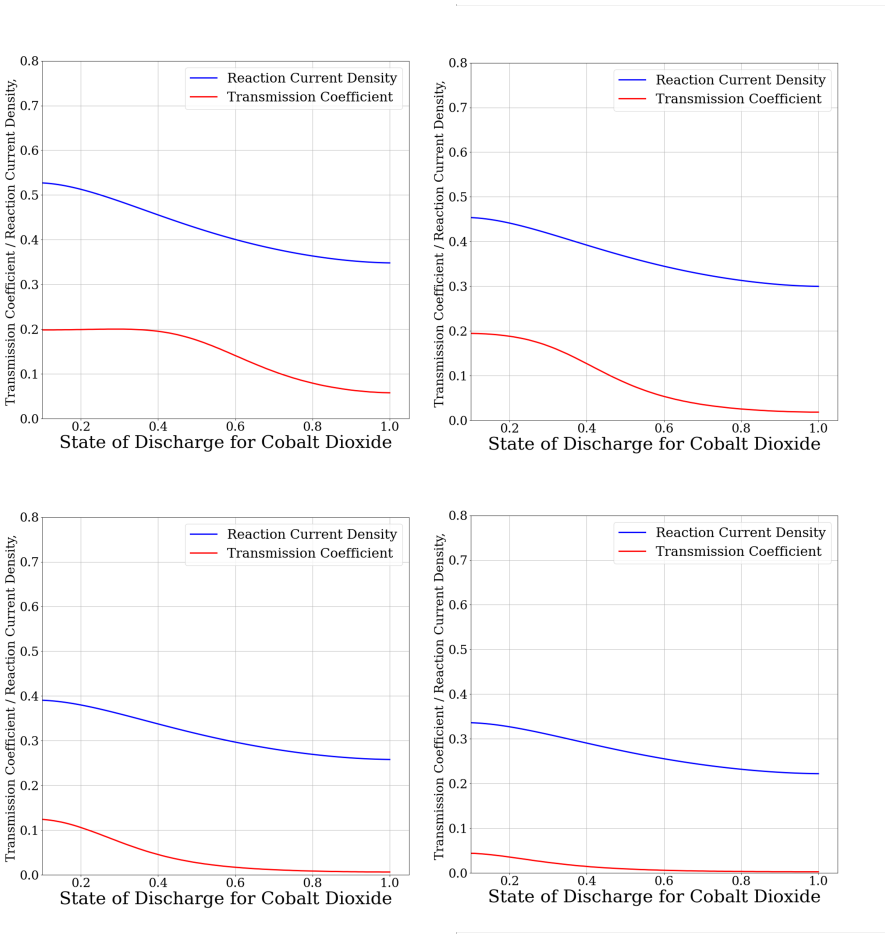

Figure 23: Transmission coefficients and current density as functions of state of discharge for a cobalt dioxide cathode discharged at various voltages, a) $E = 4.2V$, b) $E = 4V$, c) $E = 3.8V$ and d) $E = 3.6V$.

The plots in Figure 23 show the trend of both transmission coefficient and current density decreasing as the system is discharged. Similarly, the plots show that the higher the voltage that the cell is discharged at, the higher the transmission coefficient. This suggests that when discharged at higher voltages, there is a increased chance of electrons tunnelling against the potential curve and into the electrolyte. This is likely to cause unwanted side reactions, such as the electron reacting with the lithium ions on the surface of the cathode to form a solid layer rather than allowing the lithium ion to intercalate. This could lead to an irreversible decrease in capacity if this lithium isn't able to be removed and de-intercalate back into the anode on charging, or could simply cause damage to the cathode, therefore reducing its capacity for future charge/discharge cycles. These electrons also could react with the electrolyte causing its decomposition.

These type of reactions occurring on the cathode can cause the formation of a layer known as the cathode-electrolyte interphase (often shortened to CEI). It has been found that higher discharge voltages can increase the risks of CEI layers forming (Guo et al., 2022).

We repeated this process for the LFP cathode using equation [5.46] for the values of the equilibrium potential over the discharge process, E_{eq}. The plot in Figure 24 shows the results for the transmission coefficients (in red) and the current densities (in blue) as a function of state of discharge. We varied the values of E between $E = 3.3 - 3.9V$; the plots show: a) $E = 3.9V$, b) $E = 3.7V$, c) $E = 3.5V$ and d) $E = 3.3V$. These values were chosen as they are close to the usual discharges voltages for LFP (Lain and Kendrick, 2021).

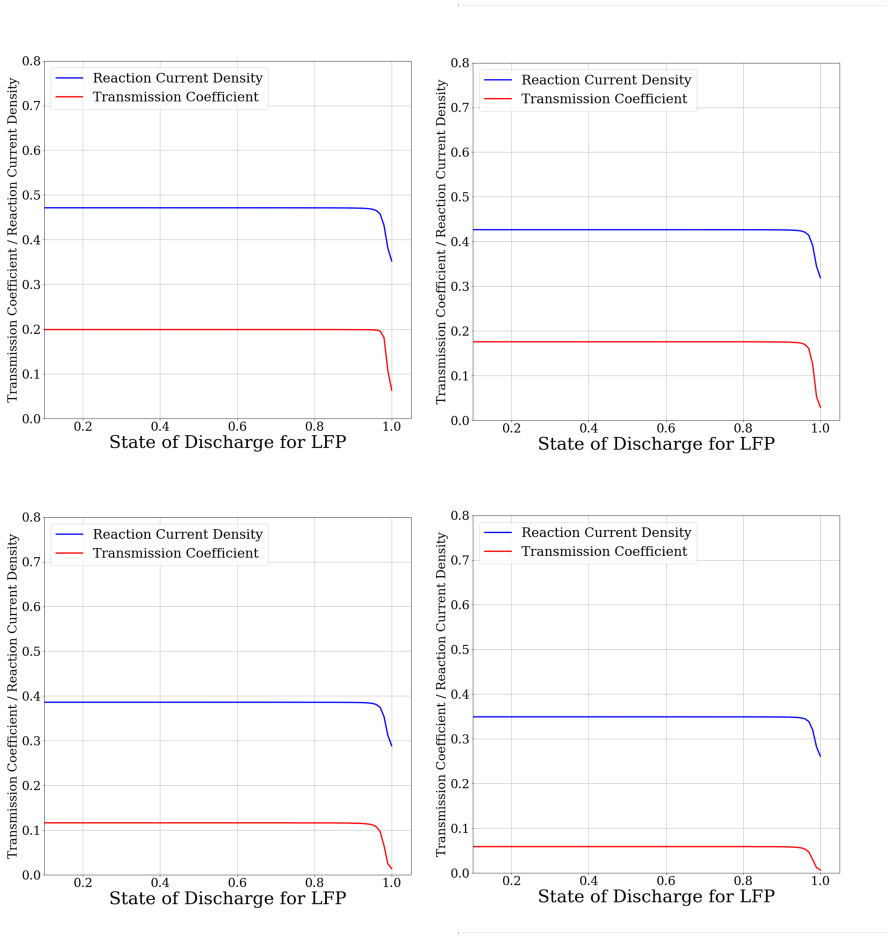

Figure 24: Transmission coefficients and current density as functions of state of discharge for an LFP cathode discharged at various voltages, a) $E = 3.9V$, b) $E = 3.7V$, c) $E = 3.5V$ and d) $E = 3.3V$.

The results for the LFP cathode show a similar trend to the cobalt dioxide cathode, with the transmission coefficients decreasing with lower discharge voltages. This is to be expected as it has been found that LFP can also suffer from the formation of CEI layers, especially at higher voltages (Kim et al., 2023). The reactions involved in forming this layer are often exothermic, leading to the release of heat which can cause safety issues. The degradation of the cathode material has also been found to increase at higher temperatures, and often led to a significant decrease in capacity (Wang et al., 2022).

5.5 Summary and Further Work

In this chapter, we have studied the electrical double layer; this layer occurs at the interface between an electrode and the electrolyte. In contrast to the bulk electrolyte, the concentrations of the ionic species in this region can no longer be assumed to be equal.

We began with an overview of the structure of the double layer and how the electric potential varies in this region. We introduced the concept of quantum tunnelling through a potential barrier compared to the classical mechanics approach. We discussed how the Schrödinger equation could be applied to give probabilities of electrons tunneling through the potential barrier. We demonstrated the solutions to the Schrödinger equation for a simple single barrier and a double barrier. Then, we derived a model to solve for any given potential barrier and calculate the transmission coefficients. We calculated these coefficients for different states of discharge.

We then introduced the Butler-Volmer equation, which is used to describe the reaction kinetics occurring at the electrode-electrolyte interface. We studied the equilibrium potentials for specific electrode materials using data given in the literature. This allowed us to substitute the equations for the equilibrium potentials into the Butler-Volmer equation to give the current density as a function of state of discharge.

We compared the transmission coefficients and the current densities for lithium iron phosphate and cobalt dioxide cathodes, discharged at various voltages, to give insight into how these vary over the discharge process. We found higher voltages

typically led to increased transmission coefficient for both types of cathode material. We suggest this could give insight into electron tunnelling contributing to increased cathode degradation and the formation of CEI layers.

5.5.1 Further Work - Intercalation Models

To further study the double layer and the reactions occurring on the electrode-electrolyte interface we could study the intercalation mechanisms in more detail. In 1996, lithium iron phosphate ($LiFePO_4$, known as LFP) was found to be a good candidate for use as a cathode material (Padhi, Nanjundaswamy and Goodenough, 1996), however this material leads to a relatively flat discharge curve, implying that a separation into lithium-rich and lithium-poor phases occurs during this process (Bazant, 2012). This leads to a need for a more detailed look into the diffusion occurring within these particles, as a linear diffusion can no longer be assumed. In this section, we will briefly set out the relevant background to the shrinking-core model and the Cahn-Hilliard equation.

The Shrinking Core Model: Up until 1996, most models of the intercalation of lithium used linear Fickian diffusion, where the reaction occurs on the surface of the particle and then lithium diffuses into the particle. This diffusion is assumed to only occur in the radial direction. During discharge, the lithium is inserted into $FePO_4$ by the reaction shown by equation [5.78]:

$$FePO_4 + x\,Li^+ + xe^- \rightarrow Li_xFePO_4, \qquad [5.78]$$

where x is the number of moles of lithium that is being transferred.

After the discovery of LFP's properties during discharge, a new model was first proposed to explain these observations. Their research found that the capacity of the cell decreased more severely than expected over longer cycles. They concluded that this was a reversible capacity loss that was due to the two-phase reaction that occurs, and could be avoided by reducing the current (Padhi, Nanjundaswamy and Goodenough, 1997).

They proposed the following alternative reaction:

$$FePO_4 + x\,Li^+ + xe^- \rightarrow xLiFePO_4 + (1-x)FePO_4. \qquad [5.79]$$

As this lithium is inserted, it is first inserted on the surface of the particle, forming a shell of $LiFePO_4$ and an interface between the two regions. This is then followed by more lithium insertion at this new interface, forming another shell within the previous one. This leads to a series of shells being formed, along with a new interface each time, with each shell having a smaller surface area than the previous. This process was termed the 'shell-core' mechanism and can be seen in Figure 25.

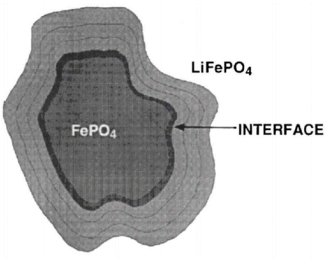

Figure 25: A representation of the shell-core mechanism, a figure taken from (Padhi, Nanjundaswamy and Goodenough, 1997). The figure shows a series of shells forming around the lithium-poor core, with the interface moving inwards as more shells form.

As the diffusion proceeds at an assumed constant rate, the surface area of the interface also shrinks, meaning that at some point the amount of lithium transported to the interface will no longer be supported. The surface area when this occurs is termed the critical surface area; beyond this point less lithium is able to be transported and the performance of the cell is diffusion-limited. However, this cell performance can be restored on the following cycles and does not represent an irreversible capacity fade (Padhi, Nanjundaswamy and Goodenough, 1997).

In 2004, the porous electrode theory was then developed to include a similar mechanism, now termed the shrinking core model, that shows similarities to the previous mechanisms; a representation is shown in Figure 26.
The mechanism begins with lithium being inserted at the surface of the particle:

$$FePO_4 + y\,Li^+ + ye^- \rightarrow Li_yFePO_4 \qquad [5.80]$$

Some of this lithium is then transported to the interior of the particle, via diffusion. We denote this amount by x, where $x < y$.

$$FePO_4\,(\text{interior}) + Li_yFePO_4\,(\text{outer}) \rightarrow Li_xFePO_4\,(\text{int}) + Li_{y-x}FePO_4\,(\text{outer}) \qquad [5.81]$$

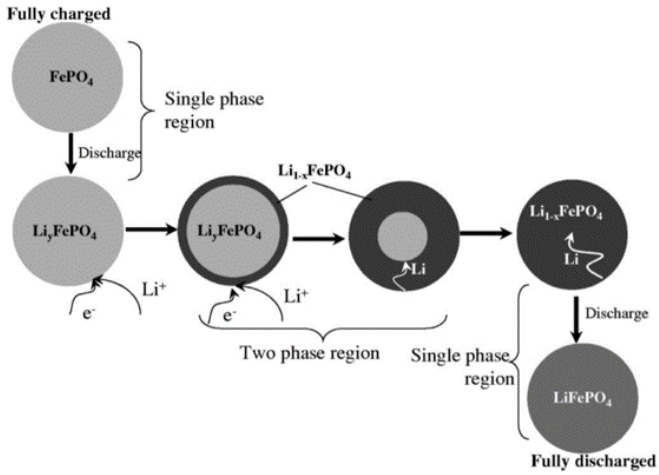

Figure 26: A representation of the shrinking core mechanism, a figure taken from (Srinivasan and Newman, 2004). The figure shows the insertion of lithium on the surface while simultaneously lithium diffuses into the lithium-poor core, causing this core to shrink.

However while this is occurring, more lithium is being inserted into the outer shell:

$$\mathrm{Li}_{y-x}\mathrm{FePO}_4\,(\text{outer}) + x\,\mathrm{Li}^+ + x\mathrm{e}^- \rightarrow \mathrm{Li}_y\mathrm{FePO}_4\,(\text{outer}) \qquad [5.82]$$

This process leads to a lithium-rich outer shell with a lithium-poor inner core; as the mechanism proceeds more of the core becomes lithium-rich, essentially causing the lithium-poor core to 'shrink' as the interface between the two phases moves inwards (Srinivasan and Newman, 2004).

The Cahn-Hilliard Equation: Another approach to modelling phase separation is using a non-linear partial differential equation known as the Cahn-Hilliard equation [5.88], developed in 1957.

As in previous chapters, we can start by denoting the mass flux as:

$$\frac{\partial c}{\partial t} = -M\nabla^2\mu, \qquad [5.83]$$

where c is the concentration, M is the mobility and μ is the chemical potential; we can also define the chemical potential as:

$$\mu = \frac{\partial G}{\partial c} \qquad [5.84]$$

where G is the Gibbs free energy.

We can define the Gibbs free energy density as:

$$F = \int_V (f(c) + \varepsilon^2 |\nabla c|^2) dV, \qquad [5.85]$$

where $f(c)$ is a scaled free energy density due to the contributions of both phases, a function that has the form of a double potential. The $\varepsilon^2|\nabla c|^2$ term gives a measure of the free energy density due to the concentration gradient at the interface. Here, ε is a phenomenological parameter which scales with interface width (Cahn and Hilliard, 1958).

We can therefore define the Gibbs free energy as:

$$G(c) = f(c) + \varepsilon^2 |\nabla c|^2), \qquad [5.86]$$

and therefore using [5.84], we can find:

$$\mu = f'(c) + \varepsilon^2 \nabla^2 c. \qquad [5.87]$$

Finally, substituting [5.87] into [5.83] we find:

$$\frac{\partial c}{\partial t} = -M\nabla^2 (f'(c) + \varepsilon^2 \nabla^2 c) \qquad [5.88]$$

which is know as the time-dependent Cahn-Hilliard equation.

6 Conclusions and Future Work

In this thesis, we have studied charge transport in lithium-ion batteries by considering the movements of charged ions in different parts of an electrochemical cell. Here, we will summarise the work completed in each chapter with specific details on the novel results produced in Chapters 3 and 5 and how this work could be taken further.

We began Chapter 1 by giving an overview of lithium-ion batteries and their use as energy storage devices. We discussed the structure of an electrochemical cell and the electrochemical reactions that occur during the charge and discharge processes. We gave background to the current popular research areas with a particular focus on electrode and electrolyte materials and experimental and computational methods to improve their performance and reliability.

In Chapter 2, we began to explore models that can be used to describe charge transport in the electrolyte. We began by considering a dilute electrolyte to derive the equations for the Poisson-Nernst-Planck theory and then went on to consider how this can be applied to the electrolyte near an electrode's surface, where a double layer forms. Throughout the model for dilute electrolytes, we assumed charge neutrality, which we justified by non-dimensionalising the model and using the fact that the Debye length for a dilute electrolyte is very small compared to the overall scale of the cell (Richardson and King, 2007). This allowed for the concentrations of each species in the electrolyte, c_n and c_p, to be replaced by electrolyte concentration, c, which reduces the number of equations and boundary conditions required to solve the model.

We have also assumed the electrolyte behaves as an ideal solution which neglects interactions between the differently charged ions. In a dilute electrolyte, this assumption is reasonable, however electrolytes used in lithium-ion batteries are often of higher concentration ($\sim 1\,\mathrm{M}$) than the dilute model allows (Newman and Thomas-Alyea, 2004). At these higher concentrations, ions passing close to one another will become much more frequent, making these interactions important to consider. Due to the charges of the ions, oppositely charged ones will tend to attract each other, and this leads to lower mobility.

This motivated a look into the Maxwell-Stefan equations to model for moderately concentrated electrolytes (Newman et al., 2003), where the mole fraction term in the electrochemical potentials is replaced with the activity $a_i(c_i)$. In Chapter 3, we introduced the idea of electrochemical potential and studied how they could be incorporated into charge transport models for the electrolyte phase. We opted to formulate these into our own model and to include partial molar volume terms for each species in the electrolyte to place restrictions on the high concentrations found adjacent to the electrodes. Most models in the literature tend to predict higher values for these concentrations than could realistically fit into the space. We gave analytical and numerical solutions to our model. Our analytical solution appeared to place too many restrictions on the total concentration allowed in a given volume, so we relaxed these restrictions and solved the model numerically using a finite difference scheme.

We then discussed the difference between ideal and non-ideal solutions. In order to account for the interactions between the ionic species, we looked at the Maxwell-Stefan equations and Margules functions. We set up a model that uses a Monte Carlo algorithm to simulate the ionic movements in the electrolyte; we applied Margules functions to calculate values for the activity coefficient for various electrolyte concentrations and solvent choices. Comparing the simulation results to experimental results from the literature, we found agreement at low concentrations, but the results deviated to much higher activity coefficients at higher concentrations.

This motivated us to study the solvent more closely; we opted to account for the formation of solvation shells in the simulation. These shells form in electrolytes with polar solvents, such as those typically studied in the literature. This involved making changes to the algorithm to represent the solvent molecules (adjacent to a charged ion) as having partial charges on opposite sides of the molecule. We repeated the simulation with these changes and found better agreement with the experimental results. We observed that the mixed solvent used in the literature showed promising results when assuming the lithium ions have coordination numbers ~ 4, with the higher concentrations no longer showing significant deviation.

This model and the simulation results are a novel contribution towards moderately concentrated electrolyte research. Often in the literature, ion-ion and ion-solvent

interactions are neglected but they become important to consider at higher concentrations. Here, we show their inclusion gives good agreement with experimental results and by studying the solvent in more detail we were able to continue to refine our results. We feel this model could be used to further understand electrolytes using different solvents, by altering the solvent interactions further to account for the polarity of the chosen solvent.

In Chapter 4, we introduce the Doyle-Fuller-Newman (DFN) model, a popular charge transport model for electrochemical cells. The DFN model is often computationally intensive to solve; a single-particle model can bring simplifications while still maintaining high accuracy. Following the model derived by (Richardson, et al., 2020), we began by non-dimensionalising the DFN model and then applied asymptotic analysis to find the leading-order model and the first-order correction terms.

In Chapter 5, we outlined a model where we attempted to account for the double layer at the electrode's surface. We have summarised the background of quantum tunnelling and how this differs from classical mechanics. The Schrödinger equation can be solved to give a measure of the probability of a quantum particle (in this case, an electron) tunnelling through a potential barrier. Starting from the simple potential step barrier, we discussed the form of a general matrix equation that can be applied to any potential curve. We applied this model to cathodes made of lithium iron phosphate and lithium cobalt dioxide to find the transmission coefficients when discharged at different voltages. These coefficients give a measure of the probability of the electron tunnelling through the potential barrier. We used data from the literature to find equations for the equilibrium potentials for these materials. An interesting further look could consider not only the transmission coefficient for the electron tunnelling through the complete barrier but also how this transmission coefficient changes throughout the barrier.

We introduced the Butler-Volmer equation to study the reaction kinetics of the redox reactions occurring on the electrode surfaces. Using the equilibrium potentials, we found the current densities for the same cathode materials and compared them to the results from the electron tunnelling.

Applying the theory behind electron tunnelling to electrochemical cells is not of-

ten considered in the literature, and is typically only looked at with relation to anode materials, such as graphite. Here, we instead focus on cathode materials. The motivation behind studying electron tunnelling was to determine if it could be occurring at the electrode surface and contributing to the Butler-Volmer reaction rates, with the idea that a higher occurrence of electron tunnelling could lead to faster reactions and therefore faster lithium (de)-insertion.

Instead, the work in Chapter 5 indicated potential drawbacks to electrons tunnelling out of the electrodes. We observed that the transmission coefficients increased at higher discharge voltages; we suggested this could explain some of the degradation these cathodes can experience. If electrons are tunnelling through the potential barrier, they could go on to react with the electrolyte or irreversibly react with lithium ions on the surfaces of the electrode. We suggest it could be a significant mechanism through which a cathode-electrolyte interphase is able to form as well as electrolyte decomposition. This is due to less available lithium ions in the electrolyte for charge transport, leading to a reduction in capacity on repeated charge-discharge cycles, especially at higher discharge voltages where our electron tunnelling model suggests higher rates of electron tunnelling could be occurring.

6.1 Further Work

Here, we detail some possible research ideas to expand on the work done in each chapter.

Further work on the Monte Carlo algorithm in Chapter 3 could include comparisons to a continuous model derived from the Debye-Hückel theory. This could provide ideas for how to account for the ionic interactions for future iterations of the algorithm. Similarly, introducing the Maxwell-Stefan equations, and therefore including the effects of the drag forces between ions, could prove valuable for refining the simulation for higher concentrations.

The simulation could be expanded to 3D and with a larger lattice, this wouldn't add too much more complexity to code the simulation but would require much more computing power. The results could once again be compared to the literature and other parameters could be calculated, such as electrolyte transference number t^+ or electrolyte conductivity κ. More consideration of the ionic movements at the

boundaries of the system would then become more important.

In solution, the positive and negative ions will have different radii from when they are in solid form. Ionic radii depend on atomic structure and so there will be a variance in how close the ions and solvent molecules can get to each other depending on the ions involved in the interaction. Our lattice treated the possible ion sites as a grid of sites of set size and equal distance from each other. To more accurately represent reality this could be reconsidered, but would add significant additional complexity to the algorithm.

Chapter 4 introduces the single-particle model; this model shows good agreement with the DFN model while being computationally quicker to solve and therefore a similar process of asymptotic analysis could be applied to other models, such as those used in battery management systems and models predicting electrode degradation or thermal modelling. These models are often very computationally complex to solve, and so a single-particle model could be a reasonable alternative.

In Chapter 5, we used electron tunnelling to explore the double layer. Our results provided a reasonable basis for further research into the formation of CEI layers, and the equivalent solid electrolyte interphase (SEI) layers that form on anodes. Studying the effects of these layers on cell capacity over multiple cycles or possible ways to reduce electron tunnelling, and therefore reduce the formation of these layers, could be valuable in research into increasing cycle life and overall cell performance. Such as a look at more electrode materials and their specific chemistries and how this affects the electric potential between the electrodes.

A model for lithium diffusion within the electrode particles could be included. Models in the literature often assume linear diffusion in the radial direction, but experimental results have shown this doesn't fully describe the lithium transport. Nonlinear diffusion has been researched with more complex models considering specific electrode materials. For example, lithium iron phosphate undergoes phase separation during intercalation, we briefly set out the Cahn-Hilliard equation which has been a focus of research recently to account for this behaviour. Combining this with the models in Chapters 3 and 5 could form a full-cell model; our detailed look at the ionic interactions and the solvent molecules in the electrolyte could lead to

more interesting results and insights for other parts of a cell.

References

Allart,D., Montaru, M. and Gualous, H. (2018). Model of Lithium Intercalation into Graphite by Potentiometric Analysis with Equilibrium and Entropy Change Curves of Graphite Electrode. *Journal of The Electrochemical Society*, 165(2), pp.A380-A387.

Al Hallaj, S., Maleki, H., Hong, J. and Selman, J. (1999). Thermal modeling and design considerations of lithium-ion batteries. *Journal of Power Sources*, 83(1-2), pp.1-8.

Arora, P., White, R., Doyle, M. (1998). Capacity Fade Mechanisms and Side Reactions in Lithium-Ion Batteries. *Journal of The Electrochemical Society*, 145(10), p.3647.

Arora, P., Doyle, M., White, R. (1999). Mathematical Modeling of the Lithium Deposition Overcharge Reaction in Lithium-Ion Batteries Using Carbon-Based Negative Electrodes. *Journal of The Electrochemical Society*, 146(10), p.3543.

Atkins, P., Clugston, M., Frazer, M. and Jones, R. (1988). *Chemistry: Principles and Applications*. London: Longman, pp.162-176.

Atkins, P. and De Paula, J. (2014). *Atkins' Physical Chemistry*. 10th ed. Oxford: Oxford University Press.

Aurbach, D. (2000). Review of selected electrode-solution interactions which determine the performance of Li and Li ion batteries. *Journal of Power Sources*, 89(2), pp.206-218.

Aurbach, D. (2003). Electrode-solution interactions in Li-ion batteries: a short summary and new insights. *Journal of Power Sources*, 119-121, pp.497-503.

Bard, A. and Faulkner, L. (2001). *Electrochemical Methods: Fundamentals and Applications*. 2nd ed. New York: John Wiley & Sons, p.60.

Bazant, M., Thornton, K. and Ajdari, A. (2004). Diffuse-charge dynamics in elec-

trochemical systems. *Physical Review E*, 70(2).

Bazant, M. (2012). Phase-Field Theory of Ion Intercalation Kinetics. *Materials Science*, Corpus ID: 59332531.

Binnig, G.; Rohrer, H. (1986). Scanning tunneling microscopy, *IBM Journal of Research and Development*. 30(4) p.355-369.

Biton, M., Yufit, V., Tariq, F., Kishimoto, M. and Brandon, N. (2016). Enhanced Imaging of Lithium Ion Battery Electrode Materials. *Journal of The Electrochemical Society*, 164(1), A6032.

Blomgren, G. (2017). The Development and Future of Lithium Ion Batteries. *Journal of The Electrochemical Society*, 164(1), pp.A5019-A5025.

Bohinc, K., Kralj-Iglič, V. and Iglič, A. (2001). Thickness of electrical double layer. Effect of ion size. *Electrochimica Acta*, 46(19), pp.3033-3040.

Bothe D. (2011) On the Maxwell-Stefan Approach to Multicomponent Diffusion. In: Escher J. et al. (eds) *Parabolic Problems. Progress in Nonlinear Differential Equations and Their Applications*, 80. Basel: Springer

Botte, G., Subramanian, V. and White, R. (2000). Mathematical modeling of secondary lithium batteries. *Electrochimica Acta*, 45(15-16), pp.2595-2609.

Brown, M., Goel, A. and Abbas, Z. (2016). Effect of Electrolyte Concentration on the Stern Layer Thickness at a Charged Interface. *Angewandte Chemie*, 55(11), pp.3790-3794.

Cahn, J.W., Hilliard, J.E. (1958). Free Energy of a Nonuniform System. I. Interfacial Free Energy. *The Journal of Chemical Physics*, AIP Publishing, 28 (2), pp.258-267.

Chapman, D. L. (1913). LI. A contribution to the theory of electrocapillarity. *The London, Edinburgh, and Dublin Philosophical Magazine and Journal of Science*, Se-

ries 6, 25(148), pp475-481.

Chen. L., Fan, X., Hu, E., Ji, X., Chen, J., Hou, S., Deng, T., Li, J., Su, D., Yang, X. and Wang, C. (2019). Achieving High Energy Density through Increasing the Output Voltage: A Highly Reversible 5.3 V Battery. *Promise and reality of post-lithium-ion batteries with high energy densities*, 5 (4), pp.896-912.

Choi. J.W., and Aurbach, D. (2016). Promise and reality of post-lithium-ion batteries with high energy densities. *Chem*, 5, 16013.

Cabana, J., Monconduit, L., Larcher, D. and Palacín, M.R. (2010). Beyond Intercalation-Based Li-Ion Batteries: The State of the Art and Challenges of Electrode Materials Reacting Through Conversion Reactions. *Advanced Materials*, 22(35), E170-E192.

Danilov, D. and Notten, P. (2008). Mathematical modelling of ionic transport in the electrolyte of Li-ion batteries. *Electrochimica Acta*, 53(17), pp.5569-5578.

Dickinson, E.J.F. and Wain, A.J.. (2020). The Butler-Volmer equation in electrochemical theory: Origins, value, and practical application. *Journal of Electroanalytical Chemistry*, 872, Article 114145.

Doyle, M., Fuller, T.F. and Newman, J. (1993). Modeling of Galvanostatic Charge and Discharge of the Lithium Polymer Insertion Cell. *Journal of The Electrochemical Society*, 140(6), pp.1526-1533.

Doyle, M. and Newman, J. (1995). The use of mathematical modeling in the design of lithium/polymer battery systems. *Electrochimica Acta*, 40(13-14), pp.2191-2196.

Doyle, M., Newman, J., Gozdz, A., Schmutz, C. and Tarascon, J. (1996). Comparison of Modeling Predictions with Experimental Data from Plastic Lithium Ion Cells. *Journal of The Electrochemical Society*, 143(6), p.1890.

Duan, W., Husain, M., Li, Y., Lashari, N.R., Yang, Y., Ma, C., Zhao, Y. and Li, X. (2023), Enhanced charge transport properties of an LFP/C/graphite composite as a cathode material for aqueous rechargeable lithium batteries. *Royal Society of*

Chemistry, 13, pp.25327-25333.

Ecker, M., Käbitz, S., Laresgoiti, I. and Uwe Sauer, D. (2015). Parameterization of a Physico-Chemical Model of a Lithium-Ion Battery. *Journal of The Electrochemical Society*, 162(9), pp.A1849-1857.

Eftekhari, A. (2017). Low voltage anode materials for lithium-ion batteries. *Energy Storage Materials*, 7, pp.157-180.

Ellis, B., Makahnouk, W., Makimura, Y., Toghill, K. and Nazar, L. (2007). A multifunctional 3.5V iron-based phosphate cathode for rechargeable batteries. *Nature Materials*, 6(10), pp.749-753.

Etacheri, V., Marom, R., Elazari, R., Salitra, G. and Aurbach, D. (2011). Challenges in the development of advanced Li-ion batteries: a review. *Energy & Environmental Science*, 4(9), p.3243.

Fergus, J. (2010a). Ceramic and polymeric solid electrolytes for lithium-ion batteries. *Journal of Power Sources*, 195(15), pp.4554-4569.

Fergus, J. (2010b). Recent developments in cathode materials for lithium ion batteries. *Journal of Power Sources*, 195(4), pp.939-954.

Franco, A. (2013). Multiscale modelling and numerical simulation of rechargeable lithium ion batteries: concepts, methods and challenges. *RSC Advances*, 3(32), p.13027.

Fuller, T., Doyle, M. and Newman, J. (1994a). Simulation and Optimization of the Dual Lithium Ion Insertion Cell. *Journal of The Electrochemical Society*, 141(1), p.1-10.

Fuller, T., Doyle, M. and Newman, J. (1994b). Relaxation Phenomena in Lithium-Ion-Insertion Cells. *Journal of The Electrochemical Society*, 141(4), p.982-990.

Furihata, D. (2001) A stable and conservative finite difference scheme for the Cahn-

Hilliard equation. *Numerische Mathematik*, 87, pp.675-699

Garcia, R., Chiang, Y., Craig Carter, W., Limthongkul, P. and Bishop, C. (2005). Microstructural Modeling and Design of Rechargeable Lithium-Ion Batteries. *Journal of The Electrochemical Society*, 152(1), pp.A255 - A263.

Gauthier, M., Carney, T., Grimaud, A., Giordano, L., Pour, N., Chang, H., Fenning, D., Lux, S., Paschos, O., Bauer, C., Maglia, F., Lupart, S., Lamp, P. and Shao-Horn, Y. (2015). Electrode-Electrolyte Interface in Li-Ion Batteries: Current Understanding and New Insights. *The Journal of Physical Chemistry Letters*, 6(22), pp.4653-4672.

Ghosal, S. and Chen, Z. (2010). A nonlinear equation for ionic diffusion in a strong binary electrolyte. *Proceedings of the Royal Society A: Mathematical, Physical and Engineering Sciences*, 466(2119), pp.2145-2154.

Gillespie, D., Nonner, W. and Eisenberg, R. (2002). Coupling Poisson Nernst Planck and density functional theory to calculate ion flux. *Journal of Physics: Condensed Matter*, 14(46), pp.12129-12145.

Gomadam, P., Weidner, J., Dougal, R. and White, R. (2002). Mathematical modeling of lithium-ion and nickel battery systems. *Journal of Power Sources*, 110(2), pp.267-284.

Goodenough, J. and Kim, Y. (2010). Challenges for Rechargeable Li Batteries. *Chemistry of Materials*, 22(3), pp.587-603.

Goodenough, J. and Park, K. (2013). The Li-Ion Rechargeable Battery: A Perspective. *Journal of the American Chemical Society*, 135(4), pp.1167-1176.

Grazioli, D., Magri, M. and Salvadori, A. (2016). Computational modeling of Li-ion batteries. *Computational Mechanics*, 58(6), pp.889-909.

Griffiths, David J. (2006). *Introduction to Quantum Mechanics.* 2nd ed. Pearson.

Guo, K., Qi, S., Wang, H., Huang, J., Wu, M., Yang, Y., Li, X., Ren, Y. and Ma, J. (2022). High-Voltage Electrolyte Chemistry for Lithium Batteries. *Small*, 2(5), 2100107.

Guo, M., Sikha, G. and White, R.E. (2010). Single-Particle Model for a Lithium-Ion Cell: Thermal Behavior. *Journal of The Electrochemical Society*, 158(2), pp.A122-A132.

He, J., Tao, T., Yang, F. and Sun, Z. (2022). Unravelling Li+ Intercalation Mechanism and Cathode Electrolyte Interphase of Na3V2(PO4)3 and Na3(VOPO4)2F Cathode as Robust Framework Towards High-Performance Lithium-Ion Batteries. *ChemSusChem*, 15(15), e202200817.

Hu, M., Pang, X. and Zhou, Z. (2013). Recent progress in high-voltage lithium ion batteries. *Journal of Power Sources*, 237(1), pp.229-242.

Hunter, J. (1981). Preparation of a new crystal form of manganese dioxide: λ-MnO2. *Journal of Solid State Chemistry*, 39(2), pp.142-147.

Imamura W., Eda N., Tanaka K., Horie H., Akimoto H. (2011). Capacity fade model of Lithium-ion batteries for Practical use. In: Frey D., Fukuda S., Rock G. (eds) *Improving Complex Systems Today. Advanced Concurrent Engineering. Springer, London* p. 441-448

Jämbeck, J.P.M., Mocci, F., Lyubartsev, A.P. and Laaksonen, A. (2012). Partial atomic charges and their impact on the free energy of solvation. *Journal of Computational Chemistry*, 34(3), pp.187-197.

Ji, L., Lin, Z., Alcoutlabi, M. and Zhang, X. (2011). Recent developments in nanostructured anode materials for rechargeable lithium-ion batteries. *Energy & Environmental Science*, 4(8), p.2682.

Jokar, A., Rajabloo, B., Désilets, M. and Lacroix, M. (2016). Review of simplified Pseudo-two-Dimensional models of lithium-ion batteries. *Journal of Power Sources*, 327, pp.44-55.

Kameda Y., Saito S., Umebayashi Y., Fujii K., Amo Y. and Usuki, T. (2016). Local structure of Li+ in concentrated LiPF6-dimethyl carbonate solutions. *Journal of Molecular Liquids*, 217, pp.17-22.

Kang, B. and Ceder, G. (2009). Battery materials for ultrafast charging and discharging. *Nature*, 458(7235), pp.190-193.

Khalik, Z., Donkers, M.C.F. and Bergveld, H.J. (2021). Model simplifications and their impact on computational complexity for an electrochemistry-based battery modeling toolbox. *Journal of Power Sources*, 488, 229427.

Kim, T., Ono, L.K. and Qi, Y. (2023). Understanding the active formation of a cathode-electrolyte interphase (CEI) layer with energy level band bending for lithium-ion batteries. *Journal of Materials Chemistry A*, 11(1), pp.221-231.

Kirkpatrick, S., Gelatt, C.D. and Vecchi, M.P. (1983). Optimization by Simulated Annealing. *Science*, 220(4598), pp.671-680.

Kobayashi, S. and Uchimoto, Y. (2005). Lithium Ion Phase-Transfer Reaction at the Interface between the Lithium Manganese Oxide Electrode and the Nonaqueous Electrolyte. *The Journal of Physical Chemistry B*, 109(27), pp.13322-13326.

Korotkin, I., Sahu, S., O'Kane, S.E.J, Richardson, G. and Foster, J.M. (2021). DandeLiion v1: An Extremely Fast Solver for the Newman Model of Lithium-Ion Battery (Dis)charge. *Journal of The Electrochemical Society*, 168(6), 060544.

Lagnoni, M., Nicolella, C. and Bertei, A. (2022). Comparison of Electrolyte Transport Modelling in Lithium-ion Batteries: Concentrated Solution Theory Vs Generalized Nernst-Planck Model. *Journal of The Electrochemical Society*, 169(2), 020570.

Lain, M.J. and Kendrick, E. (2021), Understanding the limitations of lithium ion batteries at high rates. *Journal of Power Sources*, 493, 229690.

Latz, A., Zausch, J. and Iliev, O. (2011). Modeling of Species and Charge Transport

in Li-Ion Batteries Based on Non-equilibrium Thermodynamics. In: *International Conference on Numerical Methods and Applications*. Berlin, Heidelberg: Springer, pp.329-337.

Lau, J., DeBlock, R.H., Butts, D.M., Ashby, D.S., Choi, C.S. and Dunn, B.S. (2018). Sulfide Solid Electrolytes for Lithium Battery Applications. *Advanced Energy Materials*, 8(27), 1800933.

Lazzari, M. and Scrosati, B. (1980). A Cyclable Lithium Organic Electrolyte Cell Based on Two Intercalation Electrodes. *Journal of The Electrochemical Society*, 127(3), pp.773-774.

Lee, D. and Yoon, D. (2011). Computational Modeling of Charge-Discharge Characteristics of Lithium-Ion Batteries. *Journal of Energy Engineering*, 20(4), pp.278-285.

Leontyev, I. and Stuchebrukhov, A. (2011). Accounting for electronic polarization in non-polarizable force fields. *Physical Chemistry Chemical Physics*, 13, pp.2613-2626.

Leung, K. (2012). Electronic Structure Modeling of Electrochemical Reactions at Electrode/Electrolyte Interfaces in Lithium Ion Batteries. *The Journal of Physical Chemistry C*, 117(4), pp.1539-1547.

Li, H., Wang, Z., Chen, L. and Huang, X. (2009). Research on Advanced Materials for Li-ion Batteries. *Advanced Materials*, 21(45), pp.4593-4607.

Li, J., Adewuji, K., Lotfi, N., Landers, R.G. and Park, J. (2018), A single particle model with chemical-mechanical degradation physics for lithium ion battery State of Health (SOH) estimation *Applied Energy*, 212(15), pp.1178-1190.

Li, J., Du, Z., Ruther, R.E., Jin, S.AN, David, L.A., Hays, K., Wood, M., Phillip, N.D., Sheng, Y., Mao, C., Kalnaus, S., Daniel, C. and Wood III, D.L. (2017). Toward Low-Cost, High-Energy Density, and High-Power Density Lithium-Ion Batteries. *The Journal of The Minerals, Metals and Materials Society*, 69, pp.1484-1496.

Li, Q., Yang, Y., Yu X. and Li, H. (2023). A 700 Whkg-1 Rechargeable Pouch Type Lithium Battery. *Chinese Physics Letters*, 40(4), 048201

Li, W., Song, B., and Manthiram, A. (2017). High-voltage positive electrode materials for lithium-ion batteries *Chemical Society Reviews*, (10)

Liu, Q., Su., X, Lei, D., Qin, Y., Wen, J., Guo, F., Wu, Y.A., Rong, Y., Kou, R., Xiao, X., Aguesse, F., Bareno, J., Ren, Y. and Lu, W. (2018) Approaching the capacity limit of lithium cobalt oxide in lithium ion batteries via lanthanum and aluminium doping. *Nature Energy*, 3, pp.936-943.

Liu, W. (2009). One-dimensional steady-state Poisson"Nernst"Planck systems for ion channels with multiple ion species. *Journal of Differential Equations*, 246(1), pp.428451.

Lüders, C., Zinth, V., Erhard, S.V., Osswald, P.J., Hofmann, M., Gilles, R. and Jossen, A. (2017). Lithium plating in lithium-ion batteries investigated by voltage relaxation and in situ neutron diffraction. *Journal of Power Sources*, 342, pp17-23.

Luyben, William L., and Yu, C.X. *Ternary Decomposition Reaction.* John Wiley and Sons, Inc. EBooks, 2008

Malifarge, S., Delobel, B. and Delacourt, C. (2018). Experimental and Modeling Analysis of Graphite Electrodes with Various Thicknesses and Porosities for High-Energy-Density Li-Ion Batteries. *Journal of The Electrochemical Society*, 165(7), pp.A1275-1287.

Malliakas, C.D., Leung, K., Pupek, K.Z., Shkrob, I.A. and Abraham, D.P. (2016). Spontaneous aggregation of lithium ion coordination polymers in fluorinated electrolytes for high-voltage batteries. *Physical Chemistry Chemical Physics*, 18(16), pp.10846-10849.

Manthiram, A. (2017). An Outlook on Lithium Ion Battery Technology. *ACS Central Science*, 3(10), pp.1063-1069.

Marcus, Y. (1988). Ionic radii in aqueous solutions. *Chemical Reviews*, 88(8), pp.1475-1498.

Meng, J., Yao, X., Hong, X., Zhu, L., Xiao, Z., Jia, Y., Liu, F., Song, H., Zhao, Y. and Pang, Q. (2023). A solution-to-solid conversion chemistry enables ultrafast-charging and long-lived molten salt aluminium batteries. *Nature Communications volume*, 14, 3909.

Metropolis, N., Rosenbluth, A.W., Rosenbluth, M.N., Teller, A.H. and Teller, E. (1953).. Equation of State Calculations by Fast Computing Machines *Journal of Chemical Physics*, 21(6), pp.1087-1092.

Moran, M.J. and Shapiro, H.N. (2006). *Fundamentals of Engineering Thermodynamics*. John Wiley & Sons.

Mortimer, R. (2008). *Physical Chemistry*. 3rd ed. Academic Press, pp.595-605.

Newman, J. and Tiedemann, W. (1975). Porous-electrode theory with battery applications. *AIChE Journal*, 21(1), pp.25-41.

Newman, J., Thomas, K., Hafezi, H. and Wheeler, D. (2003). Modeling of lithium-ion batteries. *Journal of Power Sources*, 119-121, pp.838-843.

Newman, J. and Thomas-Alyea, K. (2004). *Electrochemical Systems*. 3rd ed. John Wiley & Sons.

Ning, G. and Popov, B. (2004). Cycle Life Modeling of Lithium-Ion Batteries. *Journal of The Electrochemical Society*, 151(10), p.A1584.

Nonner, W. and Eisenberg, B. (1998). Ion Permeation and Glutamate Residues Linked by Poisson-Nernst-Planck Theory in L-Type Calcium Channels. *Biophysical Journal*, 75(3), pp.1287-1305.

Padhi, A., Nanjundaswamy, K. and Goodenough, J. (1996). LiFePO 4: A Novel

Cathode Material for Rechargeable Batteries. *The Electrochemical Society Meeting Abstracts*, 96(1), p.73.

Padhi, A., Nanjundaswamy, K. and Goodenough, J. (1997). Phospho-olivines as Positive-Electrode Materials for Rechargeable Lithium Batteries. *Journal of The Electrochemical Society*, 144(4), pp.1188-1194.

Planella, F.B. and Widanage, W.D. (2023). A Single Particle model with electrolyte and side reactions for degradation of lithium-ion batteries. *Applied Mathematical Modelling*, 121, pp.586-610.

Planella, F.B., Sheikh, M. and Widanage, W.D. (2021). Systematic derivation and validation of a reduced thermal-electrochemical model for lithium-ion batteries using asymptotic methods. *Electrochimica Acta*, 388, 138524.

Ramadass, P., Haran, B., White, R. and Popov, B. (2003). Mathematical modeling of the capacity fade of Li-ion cells. *Journal of Power Sources*, 123(2), pp.230-240.

Ranom, R. (2014). Mathematical modelling of lithium ion batteries. *Ph.D Thesis*. The University of Southampton.

Rao, M. (2013). LiMn2O4 cathodes for solid state lithium-ion batteries - energy storage and conversion. *Journal of Optoelectronic and Biomedical Materials*, 5(1), pp.9-16.

Rao, M. (2014). Novel Cathode Materials for Rechargeable Batteries. In: *UGC Sponsored Conference on Advanced Technology Oriented Materials*. Andhra Pradesh, India, pp.11-13.

Reddy, M.V., Mauger, A., Julien, C.M., Paolella, A. and Zaghib1, K. (2020). Brief History of Early Lithium-Battery Development. *Materials*, 13(8) pp.1884-1893

Richardson, G., Denuault, G. and Please, C. (2012). Multiscale modelling and analysis of lithium-ion battery charge and discharge. *Journal of Engineering Mathematics*, 72(1), pp.41-72.

Richardson, G., Foster, J.M., Ranom, R., Please, C.P. and Ramos, A.M. (2021), Charge transport modelling of Lithium-ion batteries. *European Journal of Applied Mathematics*, 33(6), pp.983-1031.

Richardson, G. and King, J. (2007). Time-dependent modelling and asymptotic analysis of electrochemical cells. *Journal of Engineering Mathematics*, 59(3), pp.239-275.

Richardson, G., Korotkin, I., Ranom, R., Castle, M. and Foster, J.M. (2020). Generalised single particle models for high-rate operation of graded lithium-ion electrodes: Systematic derivation and validation. *Electrochimica Acta*, 339, 135862.

Richardson, G. and Korotkin, I. (2021). Heat generation and a conservation law for chemical energy in Li-ion batteries. *Electrochimica Acta*, 392, 138909.

Ritchie, A. and Howard, W. (2006). Recent developments and likely advances in lithium-ion batteries. *Journal of Power Sources*, 162(2), pp.809-812.

Rogers, D. (1962). Deriving the Gibbs-Duhem equation. *Journal of Chemical Education*, 39(10), p.527.

Samson, E., Lemaire, G., Marchand, J. and Beaudoin, J.J. (1999). Modeling chemical activity effects in strong ionic solutions. *Computational Materials Science*, 15(3), pp.285-294.

Santhanagopalan, S., Guo, Q., Ramadass, P. and White, R.E. (2006). Review of models for predicting the cycling performance of lithium ion batteries. *Journal of Power Sources*, 156(2), pp.620-628.

Sathiya, M., Leriche, J.B., Salager, E., Gourier, D., Tarascon, J.M. and Vezin, H. (2015). Electron paramagnetic resonance imaging for real-time monitoring of Li-ion batteries. *Nature Communications*, 6, 6276.

Schaefer, J.L., Lu, Y., Moganty, S.S., Agarwal, P., N. Jayaprakash and Archer, L.A.

(2011). Electrolytes for high-energy lithium batteries. *Applied Nanoscience*, 2(2), pp.91-109

Schmuck, M. and Bazant, M.Z. (2015). Homogenization of the Poisson-Nernst-Planck Equations for Ion Transport in Charged Porous Media. *SIAM Journal of Applied Mathematics*, 75(3), pp.1369-1401.

Schrödinger, E. (1926). An Undulatory Theory of the Mechanics of Atoms and Molecules. *Physical Review*, 28(6), pp.1049-1070.

Scrosati, B., Hassoun, J. and Sun, Y. (2011). Lithium-ion batteries. A look into the future. *Energy & Environmental Science*, 4(9), pp.3287-3295.

Simoes, M.C., Hughes, K.J., Ingham, D.B., Ma, L. and Pourkashanian, M. (2017). Estimation of the Thermochemical Radii and Ionic Volumes of Complex Ions (Supplemental Material). *Inorganic Chemistry*, 56(13), pp.7566-7573.

Srinivasan, V. and Newman, J. (2004). Discharge Model for the Lithium Iron-Phosphate Electrode. *Journal of The Electrochemical Society*, 151(10), pp.A1517-A1529.

Stewart S., and Newman, J (2008). Measuring the Salt Activity Coefficient in Lithium-Battery Electrolytes. *Journal of The Electrochemical Society*, 155(6), pp.A458-A463.

Stillinger, F.H. and Kirkwood, J.G. (1960). Theory of the Diffuse Double Layer. *Journal of Chemical Physics*, 33, 1282-1290.

Subramaniam, A. (2019). Analysis and Simulation of One-Dimensional Transport Models for Lithium Symmetric Cells. *Journal of The Electrochemical Society*, 166(15), pp.A3806-A3819.

Summerfield, J. (2013). Modeling the Lithium Ion Battery. *Journal of Chemical Education*, 90(4), pp.453-455.

Thackeray, M., David, W., Bruce, P. and Goodenough, J. (1983). Lithium insertion into manganese spinels. *Materials Research Bulletin*, 18(4), pp.461-472.

Thomson, G. P., Reid, A. (1927). Diffraction of Cathode Rays by a Thin Film. *Nature*, 119 (890).

Tjaden, B., Cooper, S.J., Brett, D.J.L., Kramer, D. and Shearing, P.R. (2016). On the origin and application of the Bruggeman correlation for analysing transport phenomena in electrochemical systems. *Current Opinion in Chemical Engineering*, 12, pp.44-51.

Valøen, L.O. and Reimers, J.N. (2005), Transport Properties of LiPF6-Based Li-Ion Battery Electrolytes. *Journal of The Electrochemical Society*, 152(5), pp.A882-A891.

Verma, P., Maire, P. and Novák, P. (2010). A review of the features and analyses of the solid electrolyte interphase in Li-ion batteries. *Electrochimica Acta*, 55(22), pp.6332-6341.

Verros, G.D and Giovannopoulos, F. (2009). On the Maxwell-Stefan Equations for Multicomponent Diffusion. In: *AIP Conference Proceedings* 1148(1), pp.262-266

Vigil, D.L., Stevens, M.J. and Frischknecht, A.L. (2023). Accurate Calculation of Solvation Properties of Lithium Ions in Nonaqueous Solutions. *Journal of Physical Chemistry B*, 127(37), pp.8002-8008.

Vyroubal, P., Maxa, J., Kazda, T. and Vondrak, J. (2014). Computational Modeling of Lithium Ion Battery. *ECS Transactions*, 63(1), pp.99-110.

Wang, H., Li, X., Li, F., Liu, X., Yang, S. and Ma. J. (2021). Formation and modification of cathode electrolyte interphase: A mini review. *Electrochemistry Communications*, 122, 106870.

Wang, L., Qiu, J., Wang, X., Chen, L., Cao, G., Wang, J., Zhang, H. and He, X. (2022), Insights for understanding multiscale degradation of LiFePO4 cathodes.

eScience, 2(2), pp.125-137.

Wang, Z., Wang, Z., Peng, W., Guo, H., Li, X., Wang, J. and Qi, A. (2014). Structure and electrochemical performance of LiCoO2 cathode material in different voltage ranges. *Ionics*, 20, pp.1525-1534.

Wright, M.R. (2007). *An Introduction to Aqueous Electrolyte Solutions*. John Wiley & Sons.

Wu, Y., Rahm, E. and Holze, R. (2003). Carbon anode materials for lithium ion batteries. *Journal of Power Sources*, 114(2), pp.228-236.

Xia, L., Najafi, E., Bergveld, H.J. and Donkers, M.C.F. (2017), A Computationally Efficient Implementation of an Electrochemistry-Based Model for Lithium-Ion Batteries. *IFAC-PapersOnLine*, 50(1), pp2169-2174.

Xu, J., Wu, Y. and Yin, S. (2017). Investigation of effects of design parameters on the internal short-circuit in cylindrical lithium-ion batteries. *Royal Society of Chemistry Advances*, 7(24), pp.14360-14371.

Xu, K. (2004). Nonaqueous Liquid Electrolytes for Lithium-Based Rechargeable Batteries. *Chemical Reviews*, 104(10), pp.4303-4418.

Yan, W., Yang, S., Huang, Y., Yang, Y. and Yuan, G. (2020). A review on doping-coating of nickel-rich cathode materials for lithium-ion batteries. *Journal of Alloys and Compounds*, 819, 153048.

Yiding, L., Wenwei, W., Cheng, L., Xiaoguang, Y. and Fenghao, Z. (2020). Multi-physics safety model based on structure damage for lithium-ion battery under mechanical abuse. *Journal of Cleaner Production*, 277, 124094.

Yuan, K., Bian, H., Shen, Y., Jiang, B., Li, J., Zhang, Y., Chen, H., and Zheng, J. (2014). Coordination Number of Li+ in Nonaqueous Electrolyte Solutions Determined by Molecular Rotational Measurements. *The Journal of Physical Chemistry B*, 118(13), pp.3689-3695.

Yu, S.H., Feng, X., Zhang, N., Seok, J. and Abruna, H.D. (2018). Understanding Conversion-Type Electrodes for Lithium Rechargeable Batteries. *Accounts of Chemical Research*, 51(2), pp.273-281.

Yu, S.H., Lee, S.H., Lee, D.J., Sung, Y.E. and Hyeon, T. (2015). Conversion Reaction-Based Oxide Nanomaterials for Lithium Ion Battery Anodes. *Small*, 12(16), pp.2146-2172.

Zhang, D., Haran, B., Durairajan, A., White, R., Podrazhansky, Y. and Popov, B. (2000). Studies on capacity fade of lithium-ion batteries. *Journal of Power Sources*, 91(2), pp.122-129.

Zhang, L., Liu, L., Gao, X., Pan, X., Liu, X. and Feng, X. (2022). Modeling of Lithium plating in lithium ion batteries based on Monte Carlo method. *Journal of Power Sources*, 541, 231568.

Zülke, A., Korotkin, I., Foster, J.M., Nagarathinam, M., Hoster, H. and Richardson, G. (2021). Parametrisation and use of a predictive DFN model for a high-energy NCA-Gr-SiOx battery. *Journal of The Electrochemical Society*, 168(12), 120522.

Zwicker, D. (2020). py-pde: A Python package for solving partial differential equations. *Journal of Open Source Software*, 5(48) pp.2158-2161.